UNIVERSITÀ
DI TORINO

Università degli Studi di Torino
Facoltà di Scienze MM. FF. NN.
Dipartimento di Fisica

Dottorato di Ricerca in Fisica
Ciclo XXXV

A Panchromatic View of Radio-Loud AGN and Their Environment

Candidata:
Valentina Missaglia

Supervisore:
Prof. Francesco Massaro

Università degli Studi di Torino
Dipartimento di Fisica

Dottorato di Ricerca in Fisica
Ciclo XXXV

A Panchromatic View of Radio-Loud AGN and Their Environment

Presentata da: **Valentina Missaglia**

Tutor:
Prof. Francesco Massaro

Coordinatore del dottorato:
Prof. Paolo Olivero

Anni Accademici: 2019-2022

Settore Scientifico-Disciplinare di Afferenza:
FIS/05 – Astronomia e Astrofisica

Courage is not having the strength to go on,
it is going on when you don't have the strength.
Theodore Roosevelt

Table of Contents

Abstract

Radio-loud active galactic nuclei (AGN) are among the most captivating sources in the Universe, with their high luminosity (up to 10^{48} erg s^{-1}) and spectacular extended radio emission (up to Mpc distances from the radio galaxy core). This is the result of the accretion of matter onto a supermassive black hole, at the center of the host galaxy. Radio-loud AGN are usually found in the brightest cluster galaxy (BCG) of galaxy clusters, formed through hierarchical accretions of smaller systems (i.e. groups). Through processes as synchrotron, inverse Compton and thermal bremsstrahlung, radio and X-ray astronomical facilities can detect the emission from both the lobes of the radio galaxies and the intracluster medium (ICM), the hot plasma that permeates the gravitational potential well of a galaxy group/cluster, with a density $n \sim 10^{-2} - 10^{-4}$ cm^{-3} and a temperature of T $\sim 10^{8}$ K. It has been established that a connection between the central supermassive black hole and its host galaxy exists, but it is still debated how the large-scale environment in which AGN reside affects their evolution. The study of the so-called AGN feedback gave some answers on how the AGN interact with the surrounding medium, but some questions still need to be addressed, starting from what is the dominant mechanism for powering the AGN and how this depends on the environment. Radio and X-ray observations are a key tool to investigate the feedback process in AGN because they reveal different components (synchrotron radio lobe non-thermal and bremsstrahlung ICM thermal) and allow to study the interplay between these components. In this thesis I present the results obtained from radio and X-ray observations of the most powerful radio sources in the northern hemisphere, i.e. sources from the Third Cambridge Catalog (3C). I focused on a sample restricted to the sources

lacking a detection of the optical host, and therefore named unidentified. Complementing archival infrared/optical/radio/X-ray observations represents a big step toward resolving the nature of these sources: to this end, I reduced unpublished Very Large Array radio observations, used to confirm the radio core position observed in the X-rays and obtained from old, low resolution radio maps. With these new radio observations, I morphologically classified the sources, and measured their fluxes. Panoramic Survey Telescope & Rapid Response System (Pan-STARRS) and Wide-field Infrared Survey Explorer (WISE) data helped me to identify the optical and infrared counterparts of the nuclei detected in the X-rays with *Chandra*. Among the results of this analysis, the most intriguing one is represented by the detection in the X-rays of extended emission around a source that I classified as a Fanaroff-Riley type 2 (FR IIs) radio galaxy, that also shows a tentative detection of X-ray cavities originated by the radio lobes expanding through the ICM, as described by the radio-mode feedback. This is interesting because FR IIs from the 3C are believed to inhabit poor environments, while X-ray extended emission is usually the hallmark of galaxy clusters hosting the radio galaxy. From the observations I obtained with the Sardinia Radio Telescope, I performed a high radio frequency follow-up of the giant radio galaxy 3CR 403.1. I characterized the properties of the source (flux, spectral features, rotation measure), but what caught my attention is the detection of two regions of negative radio flux density around the source, that indicates a possible presence of the Sunyaev-Zel'dovich effect in galaxy clusters. This result challenges the common picture of giant radio galaxies born and evolving in poor environments. From X-ray and optical data obtained from accepted observing proposals, I performed follow-up study of the high-redshift (z=1.408) radio-loud quasar 3C 297, which showed indications of diffuse emission in a shallow snapshot *Chandra* observation. From GEMINI optical observations I did not detect any optical companion galaxy and this, coupled with the presence of diffuse X-ray emission, is interpreted as this source being a fossil group. If confirmed, this would represent the first detection of a fossil group at such high redshift, and therefore a chance to study how the AGN feedback acts close to the epoch of galaxy clusters formation. The interplay between environment and

radio galaxy can be also investigated through optical observations, as I did in the case of the sample of wide-angle tail (WAT) radio galaxies in the local Universe listed in the WATCAT. WATs morphology (jet-warmspot-plume transition) is clearly related to the dynamical state of the cluster in which they reside, and I have shown that, at $z \lesssim 0.15$, these sources inhabit the central region of environments that are more galaxy-rich than those of Fanaroff-Riley type 1 and 2, in agreement with the hypothesis that disturbed clusters produce such a peculiar morphology. I also found that WATs tend to inhabit the central region of the group/cluster in which they reside. Therefore, complementing radio, optical and X-ray data is crucial to obtain an insight on the environment inhabited by radio-loud AGN and offers a chance to study how these sources interact with it through feedback processes.

Thesis Outline

This thesis, focused on the study of radio-loud active galactic nuclei (AGN) and their interaction with the surrounding environment, is structured as follows:

- In Chapter 1, I give an overview of the AGN phenomenon, introducing the radio-quiet/radio-loud dichotomy, focusing on radio galaxies and radio-loud quasars, that are the subject of this thesis; then, concepts as the large-scale environment of radio-loud AGN and the AGN feedback are introduced to give an insight on the current understanding of the interaction AGN/environment;

- In Chapter 2, I summarize the main details of the astronomical facilities used, and the radio, optical and X-ray data reduction procedures adopted in this work;

- In Chapter 3, I present the results obtained from the analysis of some of the radio sources listed in the Third Cambridge Catalog (3C), that are the most powerful radio sources in the northern hemisphere; in particular, I report the results of the radio/optical/IR/X-ray study of a sample of unidentified radio sources, the radio follow-up of the giant radio galaxy 3CR 403.1 and the optical follow-up of the high-redshift quasar 3C 297, possibly a fossil group;

- Chapter 4 is devoted to the analysis, via the optical richness, of the large-scale environment of the wide angle tail radio galaxies class, that is compared to the one of FR Is and FR IIs;

- In Chapter 5, I summarize the results of each work and present a future work of the interaction radio lobes/ICM;
- In the Appendix A, a brief description of the main emission processes observed in the radio and X-ray bands is reported.

List of Acronyms

3C/3CR: Third Cambridge Catalog (Revised) of Radio Sources

AGN: Active Galactic Nucleus/Nuclei

BCG: Brightest Cluster Galaxy

BLR: Broad Line Region

CMB: Cosmic Microwave Background

FR I: Fanaroff-Riley type I

FR II: Fanaroff-Riley type II

FWHM: Full Width Half Maximum

GLEAM: GaLactic and Extragalactic All-sky MWA Survey

GMOS: Gemini Multi-Object Spectrograph

GMRT: Giant Metrewave Radio Telescope

GRG: Giant Radio Galaxy

IC: Inverse Compton

ICM: Intra-Cluster Medium

IFU: Integral Field Unit

IR: Infrared

JVLA: Karl G. Jansky Very Large Array

MUSE: Multi Unit Spectroscopic Explorer

MWA: Murchison Widefield Array

NLR: Narrow Line Region

NRAO: National Radio Astronomy Observatory

NVSS: NRAO VLA Sky Survey

Pan-STARRS: Panoramic Survey Telescope & Rapid Response System

QSO:Quasi-Stellar Object

RL/RLAGN: radio-loud AGN

RM: Rotation Measure

rms: root mean square

RQ: radio-quiet

SDSS: Sloan Digital Sky Survey

SMBH: Super Massive Black Hole

SRT: Sardinia Radio Telescope

SZ: Sunyaev-Zel'dovich

UV: Ultraviolet

VLSSr: Very Large Array Sky Survey Redux

WAT: Wide Angle Tail

WISE: Wide-field Infrared Survey Explorer

List of Publications and Accepted Proposals

Here is the list of publications as first author:

- **Missaglia, V.**, Massaro, F., Capetti, A., Paggi, A., Baldi, R. D., Kraft, R. P., Paolillo, M., Tramacere, A., Campana, R. & Pillitteri, I.; "*Investigating the large-scale environment of wide-angle tailed radio galaxies in the local Universe*"; 2022, Submitted to A&A.

- **Missaglia, V.**, Madrid, J. P., Schirmer, M., Massaro, F., Rodríguez-Ardila, A., Donzelli, C. J., Valencia, M., Paggi, A., Kraft, R. P., Stuardi, C. & Wilkes, B. J.; "*Powerful yet lonely: is 3C 297 a high-redshift fossil group*?"; 2023 ApJS, 264, 6.

- **Missaglia, V.**, Murgia, M., Massaro, F., Paggi, A., Jimenez-Gallardo, A, Forman, W. R., Kraft, R. P. & Balmaverde, B.; "*High radio frequency imaging of 3CR 403.1 with the Sardinia Radio Telescope*"; 2022 ApJ, 936, 10.

- **Missaglia, V.**, Massaro, F., Liuzzo, E., Jimenez-Gallardo, A., Kraft, R. P., Forman, W. R., Paggi, A., Ricci, F., Stuardi, C., Tremblay, G. R., Wilkes, B. J., Baum, S. A., O'Dea, C. P., Kuraszkiewicz, J., Sani, E., Maselli, A., Capetti, A., Balmaverde, B. & Harris, D. E.; "*Hidden Treasures in the Unknown 3CR Extragalactic Radio Sky: A Multiwavelength Approach*"; 2021 ApJS, 255, 18.

- **Missaglia, V.**, Massaro, F., Capetti, A., Paolillo, M., Kraft, R. P., Baldi, R. D. & Paggi, A.; "*WATCAT: a tale of wide-angle tailed radio galaxies*"; 2019 A&A, 626A, 8.

I have also submitted these successful proposals as Principal Investigator:

- 2020 - **Chandra** Cycle 22: "Investigating the X-ray extended emission around the radio galaxy 3CR 297"
- 2020 - **GMRT** Cycle 38: "Probing the presence of re-energized particles in A2395"
- 2020 - **SRT**: "Investigating the radio components of the FR II radio galaxy 3C 403.1"
- 2022 - **GMRT** Cycle 43: "Hunting for the radio cores of powerful radio sources in the Southern Hemisphere"

Chapter 1

Introduction

1.1 Black Hole Paradigm

Active galactic nuclei (AGN) are the most powerful, non-explosive sources (i.e., γ-ray bursts, GRBs) in our Universe. Their emission, that spans across the whole electromagnetic spectrum (more than twenty orders of magnitude in frequency), can reach up to $\approx 10^{48}$ erg s^{-1} as in the case of the most distant quasars, in which the AGN emission outshines that from the stars in the host galaxy. In this thesis I will present the results obtained from the study of the AGN radio-loud class, that includes radio galaxies and quasars.

The hypothesis of a strong gravitational potential in the inner part of the AGN, as that produced by an accreting (and therefore active) supermassive black hole (SMBH), is the key to explain such a powerful emission, as an alternative to stellar nuclear reaction.

In 1963 the first radio-loud quasar was discovered: 3C 273 (Schmidt 1963). The author, on the basis of optical observations, concluded that 3C 273, that showed a stellar like spectrum, but had a redshift z=0.158, should have been the nucleus of a galaxy with a diameter < 1 kpc with an accreting mass in the center to produce such an estimated high luminosity (> 10^{46} erg s^{-1}). This discovery was the start to understand the AGN phenomenon. The redshift of 3C 273 has been updated by Burbidge & Rosenberg (1965) to z=0.540.

To evaluate the luminosity of an accreting SMBH, the origin of the strong inner gravitational potential, let's assume an isotropically radiating point at distance r with a bolometric luminosity L, which radiation pressure is:

$$P_{rad} = \frac{L}{4\pi r^2 c} \tag{1.1}$$

The outward force on a single electron is obtained multiplying P_{rad} for the Thomson cross-section σ_e:

$$F_{rad} = \sigma_e \frac{L}{4\pi r^2 c} \tag{1.2}$$

On the other hand, the magnitude of the gravitational force exerted by a mass M on a mass m at a distance r is:

$$F_{grav} = -\frac{GMm}{r^2} \tag{1.3}$$

The mass m can be accreted on the mass M if:

$$F_{rad} \lesssim -F_{grav} \tag{1.4}$$

that translates into:

$$L \lesssim \frac{4\pi G c m}{\sigma_e} M = 1.26 \times 10^{38} \frac{M}{M_\odot} erg\ s^{-1} \tag{1.5}$$

The luminosity expressed in Equation 1.1 is known as Eddington limit, and it express the maximum luminosity that an AGN can emit before suppressing isotropic accretion on it.

For a typical quasar $L = 10^{46}$ erg s^{-1} and therefore the Eddington mass, that is the minimum mass for a system to be gravitationally bound, is:

$$M_{Edd} \sim 8 \times 10^5 \frac{L}{10^{44}}\ M_\odot \tag{1.6}$$

As a matter of fact, the most efficient way to convert mass in energy is through accretion. Assuming a mass infalling from infinity in to a radius r onto a black hole of mass M_{BH} in a Newtonian approximation there is a conversion of potential energy into kinetic energy, and therefore the luminosity L of the AGN can be related to the gravitational potential U by the equation:

$$L \approx \frac{dU}{dt} = \frac{1}{2}\frac{GM_{BH}}{r}\frac{dm}{dt} = \frac{1}{2}\frac{GM_{BH}\dot{m}}{r} \tag{1.7}$$

where G is the gravitational constant, M_{BH} is the black hole mass, and $\dot{m}$ is the mass accretion rate.

For an accreting system, the luminosity can be also expressed as:

$$L = \eta \dot{m} c^2 \rightarrow \dot{m} = \frac{L}{\eta c^2} \tag{1.8}$$

where c is the speed of light and η the efficiency of the process, that can be therefore expressed, from equations 1.8 and 1.7, as:

$$\eta \approx \frac{GM_{BH}}{2rc^2} = \frac{R_s}{4r} \tag{1.9}$$

with $R_s = \frac{2GM}{c^2}$ being the Schwarzschild radius of the black hole. If we assume r to be of the order of the last stable orbit, where the majority of the optical and ultraviolet (UV) radiation is emitted (Peterson 1997), to be equal to $3R_s$ (as expected for a rotating Kerr black hole), the efficiency is ~10%, far larger than the case of nuclear burning in stars, where η ~0.7%.

1.2 Active Galactic Nuclei Phenomenology: Focus on Radio-Loud AGN

The first optical properties of AGN have been presented by Seyfert (1943), that observed spiral galaxies with a quasar-like nucleus, and high-excitation nuclear lines in the optical

spectra. These galaxies, named Seyfert galaxies, were later divided in two classes by Khachikian & Weedman (1974): in type 1 Seyfert, the optical spectrum shows both narrow and broad Balmer lines, while in type 2 only narrow lines are present. AGN are also classified on the basis of their radio properties: radio-quiet (RQ) mainly Seyfert galaxies and radio-quiet quasars, and radio-loud (RL) radio galaxies, radio-loud quasars and blazars. Radio galaxies and radio-loud quasar are the topic of this thesis (see Section 1.3 for more details). RL differ from RQ AGN on the basis of the ratio R of the radio flux at 5 GHz F_5 to optical flux in B band F_B, that is $R = F_5/F_B$ (Kellermann et al. 1989). AGN with $R \geq 10$ are classified as RL, otherwise they are classified as RQ. In the case of Fanaroff-Riley type I and type II (see Section 1.3 for more details) the radio emission is driven by the presence of large scale radio structures, such as jets, lobes or plumes. From an optical point of view, Laing et al. (1994) introduced the classification in Low Excitation and High Excitation Radio Galaxies (LERG and HERG, respectively), on the basis of the ratios of optical emission lines. Among the RL, another class is that of blazars, whose emission is characterized by variable, non-thermal radiation up to γ-rays, flat radio spectra, apparent superluminal motion. In blazars the relativistic jet is aligned within a small angle to our line of sight (Blandford & Rees 1978). Blazars are classified in Flat-Spectrum Radio-Quasars (FSRQ) when show featureless optical spectra, or BL Lacertae (BL Lac) with strong quasar emission lines and higher radio polarization (Fossati et al. 1998). All these classes are summarized in Table 1.1.

The radio-loud AGN paradigm, as introduced in the early nineties by Urry & Padovani (1995), describes these sources as a supermassive black hole in the center, that is actively accreting matter, distributed in the form of a geometrically thin and optically thick disk (the accretion disk, that emits as a black body a different temperatures, see e.g. Koratkar & Blaes 1999). Particles in the disk lose angular momentum, spiralizing onto the black hole, and emitting in the UV and soft X-rays. Above the disk there are very hot electrons that emit in the hard X-rays (also known as hot corona). Within 2-20$\times 10^{16}$ cm from the black hole there are quickly moving clouds of gas producing broad emission lines in the optical

Table 1.1 Classical AGN classes.

Acronym	Meaning	Properties
Quasar	Quasi-stellar radio source	Radio detection no longer needed
Sey1	Seyfert 1	FWHM $\gtrsim$ 1000 km s^{-1}
Sey2	Seyfert 2	FWHM $\lesssim$ 1000 km s^{-1}
QSO	Quasi-stellar object	Quasar-like, non-radio source object
RQ AGN	Radio-quiet AGN	see Section 1.2
RL AGN	Radio-loud AGN	see Section 1.2
FR I	Fanaroff-Riley class I radio source	radio core-brightened, see Section 1.3
FR II	Fanaroff-Riley class II radio source	radio edge-brightened, see Section 1.3
Blazar	BL Lac and quasar	BL Lacs and Flat Spectrum Radio Quasars (FSRQs)

Note: FWHM: full width half maximum. In this thesis the acronym QSOs will be used to indicate both radio-quiet and radio-loud quasars. Table adapted from Padovani et al. (2017).

spectrum (and therefore called broad line region, BLR). Around the disk there is a dusty torus, absorbing the optical/UV emission. Far from the black hole and the torus, there are slowly moving clouds, producing narrow emission lines (the narrow line region, NLR). All these features are highlighted in Figure 1.1. In the big picture, it is possible to argue that AGN differ on the basis of: orientation (Netzer 2015), accretion rate (Heckman & Best 2014), host galaxy and environment (see Chapter 4). AGN are also variable sources, and the study of the variability is essential to understand the physics of the unresolved inner part of the AGN. In particular, the size of their line emitting region can be obtained from the delays between continuum and line variations (see Ulrich et al. 1997 for a complete review).

AGN can be selected by means of frequency or variability. For each observational method we can investigate different properties, even though every selection method has some biases: in the optical, for example, identifying AGN host galaxies is affected by dust obscuration and spectra extraction is time consuming.

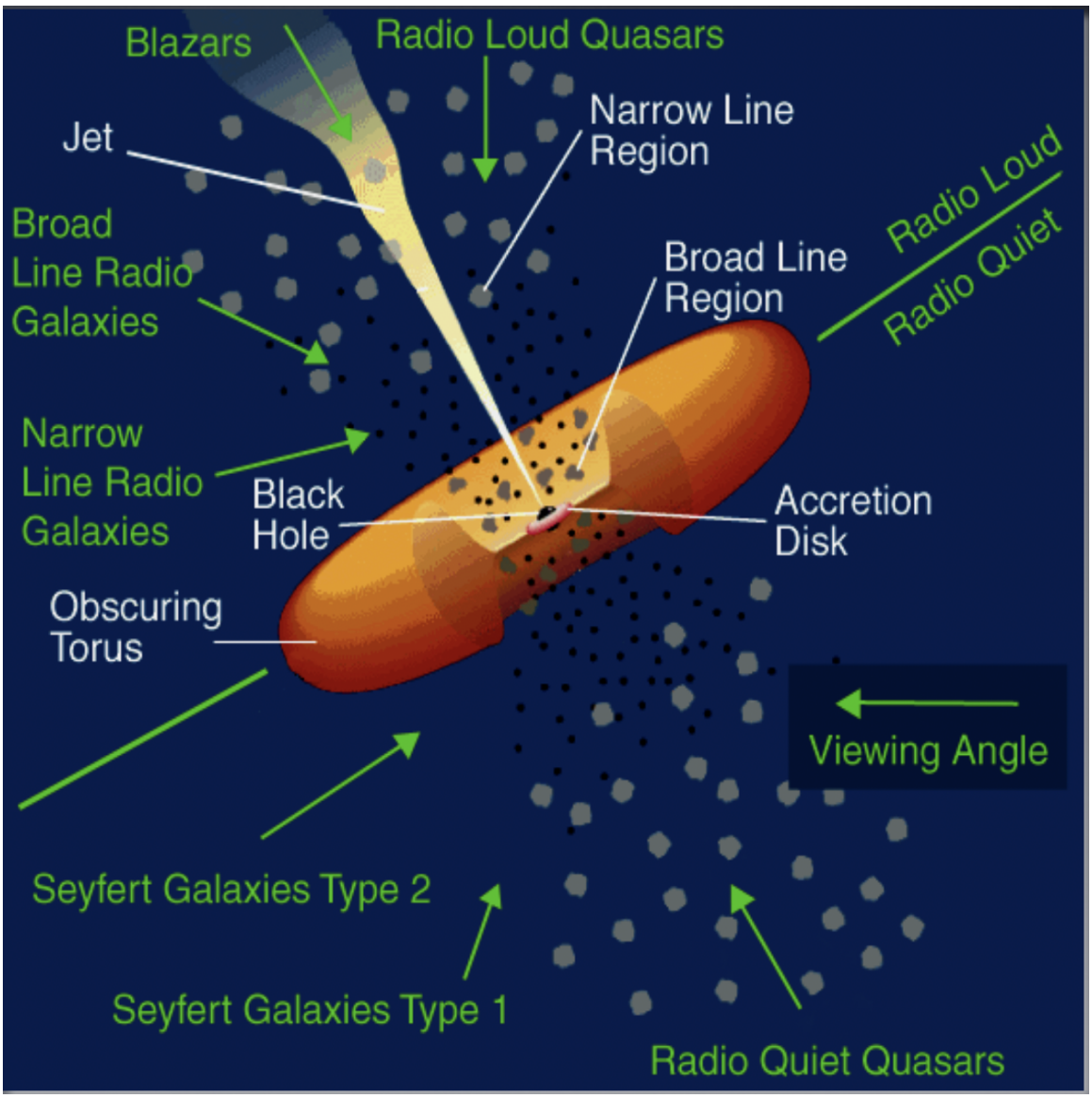

Figure 1.1 Unified AGN model showing the different classifications based on the inclination/viewing angle (green arrows). Seyfert Galaxies type 1 and type 2, for example, are the equivalent radio-quiet to Broad Line and Narrow Line Radio Galaxies. Main components of the AGN are also highlighted (not in scale; adapted from Urry & Padovani 1995).

1.3 Radio Galaxies & Radio-Loud Quasars

As briefly described in Section 1.2, AGN are divided in two main classes: radio-quiet (RQ) and radio-loud (RL, ~20% of the total). In this thesis I will focus only on the RL class, in which the radio emission is driven by jets on scales from pc to Mpc. It might be important to highlight that the classification RQ/RL is obsolete nowadays, and the new terminology for RQ is "non-jetted" and "jetted" for RL (see e.g. the review Padovani et al. 2017).

Fanaroff & Riley (1974) morphologically classified RL galaxies observed as part of the Third Cambridge Revised catalog (see Section 3.1 for more details) in type I (FR I) and type II (FR II). This morphological classification also reflects the luminosity of these sources, with FR Is having a luminosity smaller than $2{\times}10^{25}$ W Hz^{-1}sr^{-1} at 178 MHz, while FR IIs are brighter (Zirbel & Baum 1995). As shown in the left panel of Figure 1.2, FR I radio galaxies are all weak-emission line radio galaxies and are more radio bright near the core. The fainter region is at the extremities of the lobes, and therefore FR Is are also called edge-darkened radio galaxies. FR IIs, instead, have relativistic jets, surrounded by lobes, that show bright features (the hotspots) where they interact with the surrounding ICM, and are therefore called edge-brightened (Figure 1.2, right panel).

Radio observations need to be complemented with X-ray data, capable of imaging both the X-ray emitting hot gas environments of RL AGN and the X-ray inverse-Compton emission from the large-scale radio structures (lobes, plumes and jets; see Appendix A for a summary of the emission processes involved).

Radio-loud Quasars, as 3C 273, have been originally selected in the optical, and show a stellar-like spectrum. As in the case of RG, RL quasars can be classified via radio observations in core-dominated and lobe-dominated, on the basis of the ratio between the flux of the radio core to that of the extended emission.

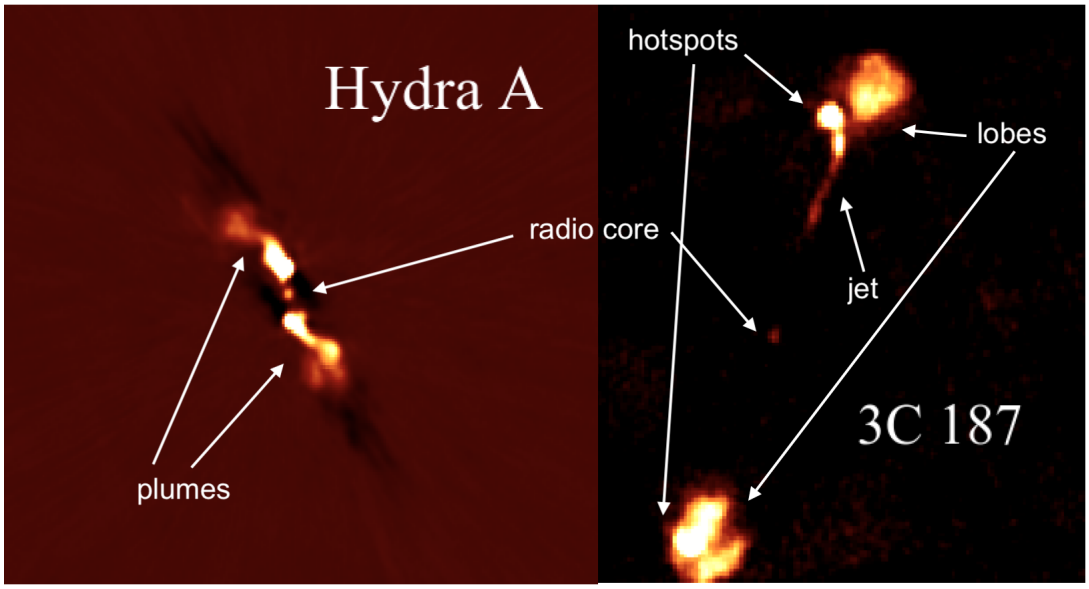

Figure 1.2 *Left panel*: example of FR I source (Hydra A, z=0.055); *Right panel*: example of FR II radio galaxy (3C 187, z=0.46). Images are obtained from the VLASS archive.

1.4 Large Scale Environment of RL AGN

Radio galaxies represent part of the non-thermal components of galaxy clusters, the largest gravitationally bound systems in the Universe, that can reach masses up to $10^{15}M_{\odot}$. The other non-thermal components of clusters are: diffuse radio emission due to re-acceleration of cosmic rays, and radio halos and relics, that are not part of the work of this thesis.

Galaxy clusters, according to the ΛCDM model, are the final stage of matter mergers and growth under the influence of gravity (bottom-up scenario). Galaxy clusters can be detected differently, on the basis of the electromagnetic frequency adopted: in the optical band, galaxies are traced by overdensities of galaxies; in the X-rays, through the bremmstrahlung emission arising from the intracluster medium (ICM), that is the hot plasma that permeates the potential well of a galaxy group/cluster, with a density $n \sim 10^{-2} - 10^{-4} cm^{-3}$ and a temperature of T~ 10^8 K (see Section A.3 in the Appendix); at microwave wavelengths, through the Sunyaev-Zel'dovich (SZ; Sunyaev & Zeldovich 1972) effect, that is the distortion of the CMB black body spectrum due to the IC scattering of ICM electrons. The X-ray emitting ICM accounts for the 10-20% of the total mass of the cluster, galaxies represent

instead only the a few percent of the cluster mass, while dark matter constitute the 80-90% of the mass.

1.4.1 Sunyaev-Zel'dovich Effect

The CMB radiation can be described as the radiation emitted by a black body according to the following:

$$I_\nu(T) = \frac{2h\nu^3}{c^2}\left(\frac{1}{e^{\frac{h\nu}{kT}}-1}\right) \tag{1.10}$$

where ν is the frequency, h is the Planck constant, c is the speed of light, k is the Boltzmann constant and T is the absolute temperature of the body.

The Sunyaev-Zel'dovich effects (thermal, kinematic, non-thermal, polarised, Sunyaev & Zeldovich 1972, 1980) are spectral signatures observed when CMB photons are scattered to higher energies by the hot electrons in the potential well of galaxy clusters, that is ICM electrons (see Figure 1.3 for a schematic representation).

Since the X-ray emitting plasma traces the largest overdensities in galaxy clusters and groups, the thermal SZ effect (tSZ) can be therefore used to detect massive clusters. The inverse Compton scattered CMB photons are moved from the low frequency part of the black body spectrum to higher energies. The spectral distortion due to the tSZ, the so-called Compton y-type distortion, and therefore the change in the CMB intensity, is expressed by:

$$\Delta I_\nu \approx I_0 y \frac{x^4 e^x}{(e^x-1)^2}\left(x\frac{e^x+1}{e^x-1}-4\right) \equiv I_0 y g(x) \tag{1.11}$$

with x=hν/k$_B$T$_{CMB}$ function of frequency and temperature.

Assuming $\Delta I_\nu / I_\nu \ll 1$ the equation can be expressed in terms of of the effective CMB temperature (that is ~2725 K, due to the expansion induced cooling, see Fixsen 2009) as:

$$\frac{\Delta T_{CMB}}{T_{CMB}} \approx y\left(x\frac{e^x+1}{e^x-1}-4\right) = y f(x) \tag{1.12}$$

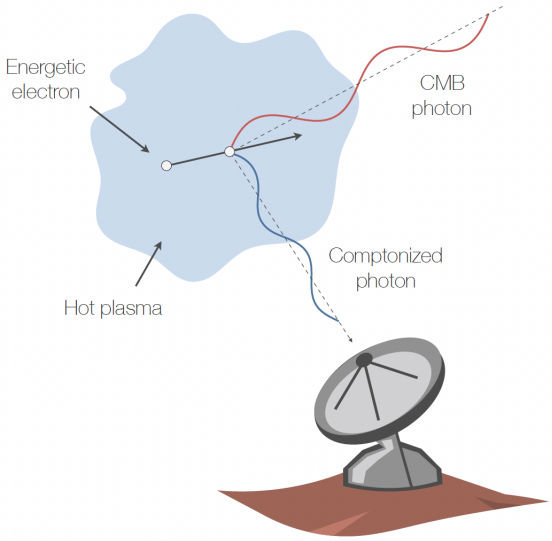

Figure 1.3 Updated illustration by Mroczkowski et al. (2019) based on the classic L. van Speybroeck SZ diagram adapted by J. E. Carlstrom. A CMB photon (red) enters the hot ICM (light blue) from an arbitrary angle, and on average is up-scattered to higher energy (blue) by an electron (black). The total momentum in the interaction is conserved, so the electron is essentially undeflected by the interaction.

where the Comptonization parameter y is:

$$y \equiv \sigma_T \int n_e(l) \frac{kT_e}{m_e c^2} dl = \frac{\sigma_T}{m_e c^2} \int P_e dl \tag{1.13}$$

with m_e the electron mass, n_e electron density as a function of the distance, σ_T the Thomson cross-section and $P_e = n_e k T_e$ the pressure of electrons (see Section 3.3 for more details on the SZ effect and the discussion of a tentative SZ detection).

1.4.2 Dynamical State of Clusters

X-rays can be used also to classify the dynamical state of galaxy clusters: the two main states are relaxed (or cool-core, see e.g. Hudson et al. 2010) and disturbed (or non-cool-core) clusters. At low redshift (z <1) clusters usually appears as relaxed systems, with a spherical shape, no major mergers, and in which the ICM has virialized. In this case, it

is possible to assume hydrostatic equilibrium. Relaxed clusters are also named "cool-core" because the X-ray surface brightness profile shows a peak of emission and a temperature drop in the central region ($\lesssim$100 kpc) of the system, implying gas cooling times shorter than the age of the galaxy. In cool-core clusters more than 50% of the X-ray luminosity is due to the core.

In the case of clusters disturbed by mergers, cool-cores can be disrupted or mixed with the surrounding hot gas through sloshing (see e.g., ZuHone et al. 2010) and the ICM appears disturbed and not symmetric. An example of disturbed cluster is Abell 2395 (z=0.15, see Figure 1.4), in which the two brightest cluster galaxies (BCGs) are clearly detected in the X-rays and are surrounded by the ICM from the two merging systems.

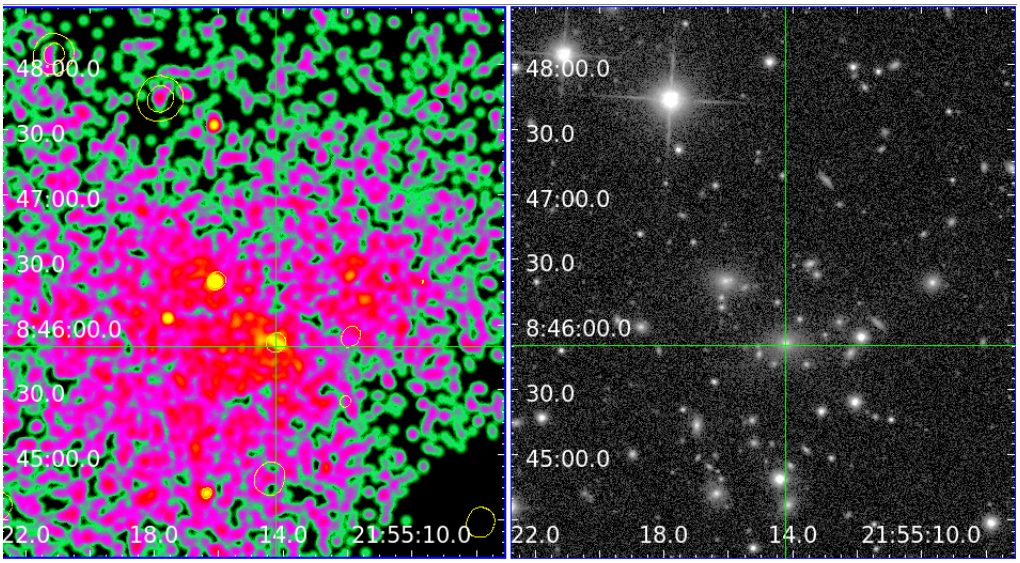

Figure 1.4 *Left Panel*: *Chandra* event file of the galaxy cluster Abell 2395 showing the two brightest cluster galaxies (BCG) interacting, clear hint of the merging state of the system. *Right Panel*: SDSS optical counterparts of the BCG detected in the X-ray (from Missaglia et al., in preparation).

1.5 AGN Feedback

As previously stated, RL AGN launch bright, powerful plasma jets (e.g. Salpeter 1964; Lynden-Bell 1969; Padovani et al. 2017; Blandford et al. 2019) that typically extend over

scales much larger than the host galaxy itself (usually elliptical) and interact with – and sometimes shape – the surrounding ICM and the galaxy itself.

This process, known as feedback (see e.g., Fabian 2012), can act on both galactic and cluster scale. In both cases, the AGN accretion is regulated, but while the feedback on cluster scale affects the ICM properties and distribution and regulates the properties/formation of the cluster, the feedback on galactic scale affects the igniting (positive feedback) or quenching (negative feedback) the star formation and regulates the properties/evolution of galaxies.

According to the "cooling flow" model (Fabian 1994), the ICM loses energy while radiating X-rays, gets compressed by the surrounding gas, that inflows into the cluster center, creating a cooling flow. This process is continuous, with the hot ICM replenishing the cooled gas. A shown in Peterson & Fabian (2006), X-ray spectroscopic observations of the BCGs, that usually host an AGN, show star formation rate not in agreement with the prediction of the cooling flow model. This is the so-called "cooling flow problem".

Jets from RL AGN, propagating through the surrounding environment, heat the ICM, creating surface brightness depressions, that are associated with cavities or bubbles (see Bîrzan et al. 2004). The mechanism described above is the radio-mode AGN feedback (also known as jet-mode, or radiatively inefficient mode), that can solve the cooling flow problem, as shown in McNamara et al. (2000) where the authors, analysing *Chandra* observations of the galaxy cluster Hydra A, report the detection of X-ray surface brightness depressions, devoided of X-ray emitting gas, coincident with the radio lobes (see Figure 1.5).

As shown in Cavagnolo et al. (2010), it is possible to establish a scaling relation between synchrotron luminosity P_{radio} (from VLA observations) and the jet power P_{jet} (from *Chandra* observations) as shown in Figure 1.6. The authors assume that, since cavities mechanical power exceeds the synchrotron power of the radio source, $P_{jet} = P_{cav}$.

The cooling time of the ICM can be derived from the equation:

$$t_{cool} = \frac{H}{\Lambda(T) n_e n_p} \tag{1.14}$$

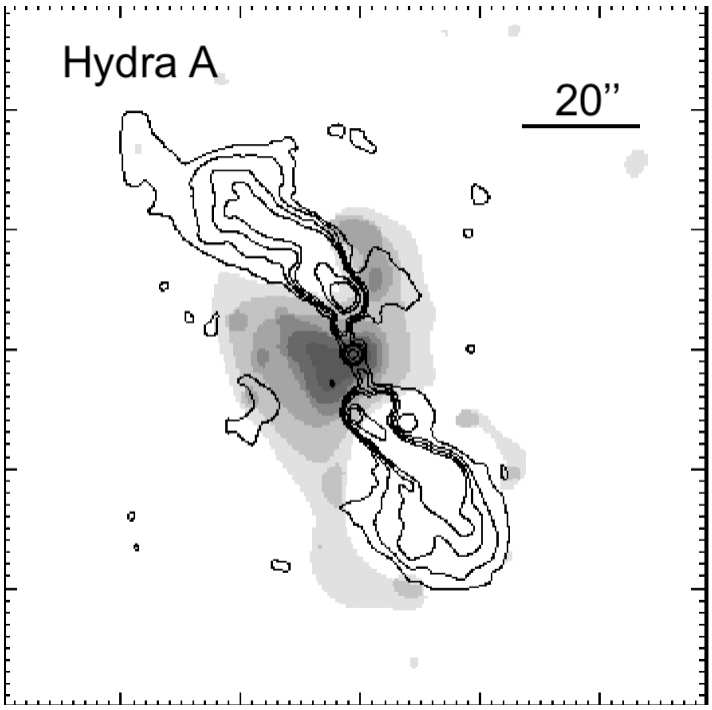

Figure 1.5 *Chandra* 40 ks image of the central region of the Hydra A cluster, with VLA radio contours (from McNamara et al. 2000). In correspondence of the radio lobes there is a decline in the X-ray surface brightness profile that is consistent with the presence of cavities.

where H is the enthalpy, $\Lambda(T)$ is the cooling function (Sutherland & Dopita 1993), n_e and n_p the electron and proton densities, respectively.

In AGN with a high accretion rate ($\frac{L_{bol}}{L_{Edd}} > 0.1$) the feedback is due to powerful outflows/winds, responsible for the reduction of the star formation and enrichment of the ICM (see e.g. Silk & Rees 1998) This is the so-called quasar-mode feedback (or radiative-mode). The outflowing gas, detected via broadened and Doppler-shifted emission/absorption lines in quasar spectra, can be found at different distances:

- nuclear winds, found within a few Mpc from the SMBH in RQ AGN, as Ultra-Fast Outflows (UFOs) detected with *XMM-Newton* as blue-shifted Fe K absorption lines (Tombesi et al. 2010), highly energetic ($\dot{E}_{kin} \simeq$ 42.6-44.6 km s^{-1}) winds of ionized gas, with a mean value of the column density $N_H \sim 10^{23}$ cm^{-2}, and a mean velocity of ~0.1c. They are likely originated, given their proximity to the central SMBH, in

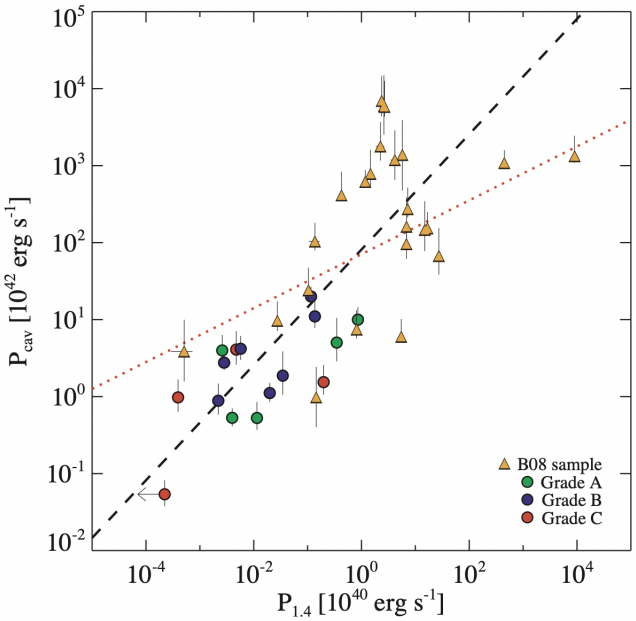

Figure 1.6 Cavity power versus 1.4 GHz radio power: orange triangles are the galaxy clusters and groups from Bîrzan et al. (2008), filled circles are sample of giant elliptical galaxies from Cavagnolo et al. (2010), where colors identify different kinds of cavities. The dotted red lines represent the best-fit power-law relations for the triangles presented in Bîrzan et al. (2008), while the dashed black lines represent the bivariate correlated error and intrinsic scatter best-fit power-law relations as described in Cavagnolo et al. (2010).

relation to accretion disk winds/ejecta. UFOs mass outflow rates can be compared with accretion rate and, therefore, affect SMBH growth.

- galactic-scale outflows, as for example that revealed by forbidden (therefore emitted in low density region, as the NLR) [OIII]λ5007 emission line, which profiles, that usually exhibit a broad and blue-shifted component, has a velocity dispersion that reflects the outflow kinematics (see e.g. Section 3.4.2 where the forbidden line [O II]λ3728 has been used to conclude that there is an extreme gas outflow in the radio-loud quasar 3C 297).

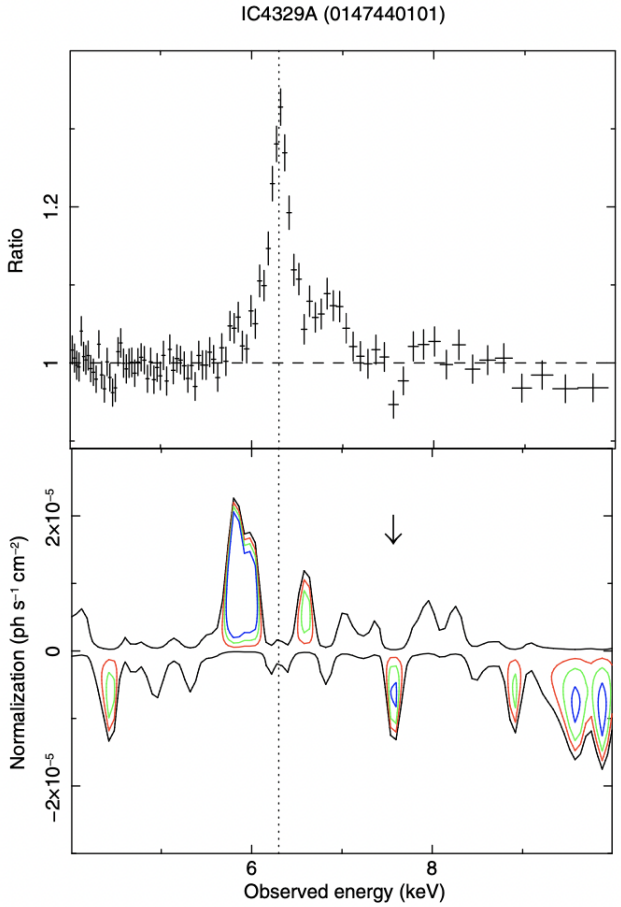

Figure 1.7 *Upper Panel*: ratio against the continuum and *Lower Panel*: contour plots with respect to the best-fit baseline model for the AGN IC 4329A. Red, green and blue are 68%, 90% and 99% levels, respectively. The arrow points to the Fe K absorption line, while the vertical dotted line refers to Fe I Kα (from Tombesi et al. 2010).

1.6 Open Questions

Even with the advent of new generation telescopes, some fundamental questions regarding AGN and their interaction with the ICM still need an answer.

- It is still not clear how jets are formed and why some AGN form jets and some don't. Also, in the presence of jets, how are they kept collimated up to distances of ~ 100 kpc?

- How do jets interact with the environment hosting the RL AGN? How this interaction plays a role in galaxy evolution?
- 3C sources usually live in poorer systems with respect to galaxy cluster. Are there any exceptions?
- Giant radio galaxies are always hosted in low density environments?
- There are observations and simulations of fossil groups at low redshift, but how does the feedback work at high z and is it possible to find fossil groups at $z > 1$?

In this thesis I addressed the last four questions via radio and X-ray observations of RL AGN.

References

Bîrzan, L., McNamara, B. R., Nulsen, P. E. J., Carilli, C. L., & Wise, M. W. 2008, ApJ, 686, 859

Bîrzan, L., Rafferty, D. A., McNamara, B. R., Wise, M. W., & Nulsen, P. E. J. 2004, ApJ, 607, 800

Blandford, R., Meier, D., & Readhead, A. 2019, ARA&A, 57, 467

Blandford, R. D. & Rees, M. J. 1978, in BL Lac Objects, ed. A. M. Wolfe, 328–341

Burbidge, E. M. & Rosenberg, F. D. 1965, ApJ, 142, 1673

Cavagnolo, K. W., McNamara, B. R., Nulsen, P. E. J., Carilli, C. L., Jones, C., & Bîrzan, L. 2010, ApJ, 720, 1066

Fabian, A. C. 1994, ARA&A, 32, 277

—. 2012, ARA&A, 50, 455

Fanaroff, B. L. & Riley, J. M. 1974, MNRAS, 167, 31P

Fixsen, D. J. 2009, ApJ, 707, 916

Fossati, G., Maraschi, L., Celotti, A., Comastri, A., & Ghisellini, G. 1998, MNRAS, 299, 433

Heckman, T. M. & Best, P. N. 2014, ARA&A, 52, 589

Hudson, D. S., Mittal, R., Reiprich, T. H., Nulsen, P. E. J., Andernach, H., & Sarazin, C. L. 2010, A&A, 513, A37

Kellermann, K. I., Sramek, R., Schmidt, M., Shaffer, D. B., & Green, R. 1989, AJ, 98, 1195

Khachikian, E. Y. & Weedman, D. W. 1974, ApJ, 192, 581

Koratkar, A. & Blaes, O. 1999, PASP, 111, 1

Laing, R. A., Jenkins, C. R., Wall, J. V., & Unger, S. W. 1994, in Astronomical Society of the Pacific Conference Series, Vol. 54, The Physics of Active Galaxies, ed. G. V. Bicknell, M. A. Dopita, & P. J. Quinn, 201

Lynden-Bell, D. 1969, Nature, 223, 690

McNamara, B. R., Wise, M., Nulsen, P. E. J., David, L. P., Sarazin, C. L., Bautz, M., Markevitch, M., Vikhlinin, A., Forman, W. R., Jones, C., & Harris, D. E. 2000, ApJ, 534, L135

Mroczkowski, T., Nagai, D., Basu, K., Chluba, J., Sayers, J., Adam, R., Churazov, E., Crites, A., Di Mascolo, L., Eckert, D., Macias-Perez, J., Mayet, F., Perotto, L., Pointecouteau, E., Romero, C., Ruppin, F., Scannapieco, E., & ZuHone, J. 2019, Space Sci. Rev., 215, 17

Netzer, H. 2015, ARA&A, 53, 365

Padovani, P., Alexander, D. M., Assef, R. J., De Marco, B., Giommi, P., Hickox, R. C., Richards, G. T., Smolčić, V., Hatziminaoglou, E., Mainieri, V., & Salvato, M. 2017, A&A Rev., 25, 2

Peterson, B. M. 1997, An Introduction to Active Galactic Nuclei

Peterson, J. R. & Fabian, A. C. 2006, Phys. Rep., 427, 1

Salpeter, E. E. 1964, ApJ, 140, 796

Schmidt, M. 1963, Nature, 197, 1040

Seyfert, C. K. 1943, ApJ, 97, 28

Silk, J. & Rees, M. J. 1998, A&A, 331, L1

Sunyaev, R. A. & Zeldovich, Y. B. 1972, Comments on Astrophysics and Space Physics, 4, 173

—. 1980, MNRAS, 190, 413

Sutherland, R. S. & Dopita, M. A. 1993, ApJS, 88, 253

Tombesi, F., Cappi, M., Reeves, J. N., Palumbo, G. G. C., Yaqoob, T., Braito, V., & Dadina, M. 2010, A&A, 521, A57

Ulrich, M.-H., Maraschi, L., & Urry, C. M. 1997, Annual Review of Astronomy and Astrophysics, 35, 445

Urry, C. M. & Padovani, P. 1995, PASP, 107, 803

Zirbel, E. L. & Baum, S. A. 1995, ApJ, 448, 521

ZuHone, J. A., Markevitch, M., & Johnson, R. E. 2010, ApJ, 717, 908

Chapter 2

Observational Techniques, Instruments and Data Reduction

Multi-wavelength astronomy is the key to study the processes and to understand the phenomena occurring in galaxies, groups and clusters. Complementing observations from the millimeter wavelength to the γ-rays allows us to observe the same particles emitting at different energy ranges. and therefore study the different physical mechanisms responsible for these emission. During my Ph.D., I have learned to reduce and analyze data both in the radio and in the X-ray band, exploiting both ground based and space telescopes. In the following section, I will give a brief overview of the observational techniques used in this thesis, and the description of the adopted data reduction processes.

2.1 Astronomical Facilities

Radio frequency radiation coming from the Milky Way was discovered less than one hundred years ago by Karl G. Jansky (1933). Apart from the old optical astronomy, from that day on, a new observational window on the Universe was opened. Then, with the advent of X–ray astronomy (Uhuru in 1970, EXOSAT in 1983, ROSAT in 1990), it has been possible to investigate the hottest and densest regions of the Universe.

Figure 2.1 JVLA parabolic dishes, on the high-desert Plains of San Agustin (New Mexico).

2.1.1 Karl G. Jansky Very Large Array (JVLA)

The Karl G. Jansky Very Large Array (JVLA, see Figure 2.1), known as Very Large Array (VLA) until 2012, is a radio telescope built in the '70s, located in Socorro (New Mexico, USA) on the Plains of San Agustin (2120 m above sea level) and operated by the National Radio Astronomy Observatory (NRAO). This telescope is constituted by numerous single dish antennas that operates in interferometry: to simulate a telescope with a very large aperture, an array of antennas creates the so called 'synthesized' aperture. For a telescope of diameter D, the angular scale at a certain wavelength λ is defined as $\theta_{\rm res} \sim \lambda/D$ (in radians). In the case of interferometers, it is possible to define the synthesized beam $\theta \sim \lambda/B_{\rm max}$ (in arcsec), where B_{max} is the maximum baseline, and the field of view (FOV) or primary beam λ/D. Another quantity to take into account when planning an observation is the largest recoverable scale defined as $\theta_{\rm LRS} \sim \lambda/{\rm B_{min}}$ (in arcsec). Every antenna samples a different location in the sky and, with the aid of the Earth rotation, all the sky can be sampled (aperture synthesis). The JVLA array configuration consists of 28 parabolic dishes of 25 m diameter (27 active and 1 spare), and the antennas are arranged in a Y shape. Each

antenna has 10 receivers from 74 MHz (band 4) to 43 GHz (Q band). Since the antennas have an intrinsic distance one from the other (called *baseline*), the sampling in the Fourier space (the (u,v) plane) is not complete. Each antenna pair is a point on the (u,v) plane, whose orientation depends on the declination of the source. The JVLA is a reconfigurable interferometer, therefore four possible array configurations exist, from A through D. As reported in Figure 2.2, the A-configuration provides the longest baselines and thus the highest angular resolution for a given frequency, but yields very limited sensitivity to surface brightness. The D-configuration, on the other hand, provides the shortest baselines, translating to a high surface brightness sensitivity at the cost of angular resolution.

Configuration	A	B	C	D
B_{max} (km)	36.4	11.1	3.4	1.03
B_{min} (km)	0.68	0.21	0.035[5]	0.035
Band	**Synthesized Beamwidth θ_{HPBW}**(arcsec)			
74 MHz (4)	24	80	260	850
350 MHz (P)	5.6	18.5	60	200
1.5 GHz (L)	1.3	4.3	14	46
3.0 GHz (S)	0.65	2.1	7.0	23
6.0 GHz (C)	0.33	1.0	3.5	12
10 GHz (X)	0.20	0.60	2.1	7.2
15 GHz (Ku)	0.13	0.42	1.4	4.6
22 GHz (K)	0.089	0.28	0.95	3.1
33 GHz (Ka)	0.059	0.19	0.63	2.1
45 GHz (Q)	0.043	0.14	0.47	1.5
Band	**Largest Angular Scale θ_{LAS}**(arcsec)			
74 MHz (4)	800	2200	20000	20000
350 MHz (P)	155	515	4150	4150
1.5 GHz (L)	36	120	970	970
3.0 GHz (S)	18	58	490	490
6.0 GHz (C)	8.9	29	240	240
10 GHz (X)	5.3	17	145	145
15 GHz (Ku)	3.6	12	97	97
22 GHz (K)	2.4	7.9	66	66
33 GHz (Ka)	1.6	5.3	44	44
45 GHz (Q)	1.2	3.9	32	32

Figure 2.2 B_{max} is the maximum antenna separation, B_{min} is the minimum antenna separation, θ_{HPBW} is the synthesized beam width (FWHM), and θ_{LAS} is the largest angular scale structure recoverable to the array.

Figure 2.3 The 64-meter single-dish of the SRT.

2.1.2 Sardinia Radio Telescope (SRT)

The Sardinia Radio Telescope (SRT, see Figure 2.3) is a fully-steerable 64 m single-dish in the plain of Pranu Sanguni (Cagliari), equipped with a computer-controlled active surface composed by about 1000 individual panels, that make it capable to operate with high efficiency in the frequency range from 0.3 to 100 GHz. It can also operate in the Very Long Baseline Interferometry (VLBI) mode. The SRT has a Gregorian shaped optical configuration with a 7.9 m diameter secondary mirror and supplementary beamwave-guide (BWG) mirrors. In its initial configuration, the SRT was equipped with three receivers, one per focal position: a 7-beam K-band (18–26 GHz, the one used for the work presented in Section 3.3) receiver, a mono-feed C-band receiver, centered at the 6.7 GHz methanol line, and a coaxial dual-feed L/P band receiver, with central frequencies of 350 MHz and 1.55 GHz, respectively (see Table 2.1 for all the details). A single dish telescope has a brightness sensitivity better than that of an aperture synthesis array of equal collecting area, and is therefore better suited for detecting faint, extended radio structures.

Table 2.1 Reference values for relevant parameters of the SRT first-light receivers, from Prandoni et al. (2017).

Receiver	RF band (GHz)	BW_{max} (MHz)	G (K/Jy)	HPBW (arcmin)	Focal position & focal ratio (f/D)
L/P-band	0.305-0.41 (P)	105	0.53	55	Primary: f/D=0.33
	1.13-1.8 (L)	500	0.52	12.5	
C-band	5.7 - 7.7	2000	0.60	2.8	BWG: f/D=1.37
K-band	18.26.5	2000	0.65	0.82	Gregorian: f/D=2.35

Col. 1: Receiver; Col. 2: RF is radio frequency band covered by the receiver; Col. 3: BW_{max} is the maximum instantaneous bandwidth; Col. 4: G is the gain; Col. 5: HPBW is the beam width at half power of the main lobe of the telescope beam; Col. 6: the focal position (primary, Gregorian, and BWG) at which the receiver is mounted and the focal ratio (f/D, where f is the focal length and D is the telescope diameter).

2.1.3 Gemini Observatory

The Gemini Observatory consists of two identical 8.1-meter diameter optical/infrared telescopes located on Mauna Kea in Hawai'i and Cerro Pachón in Chile (see Figure 2.4). Gemini Observatory's telescopes can collectively access the entire sky, and excel in a wide variety of optical and infrared capabilities. The two Gemini Multi-Object Spectrographs (GMOS), one on each telescope, provide 0.36-1.03 µm long-slit and multi-slit spectroscopy and imaging over a 5.5 square arcminute field of view. Each GMOS is also equipped with an Integral Field Unit (IFU) making it possible to obtain spectra from a 35 square arcsecond area with a sampling of $0.2''$. The Nod-and-Shuffle mode, which enables superior sky subtraction, is available with both GMOS-N and GMOS-S in most spectroscopic modes. Gemini is operated by an international partnership that includes the United States, Canada, Brazil, Argentina and Chile.

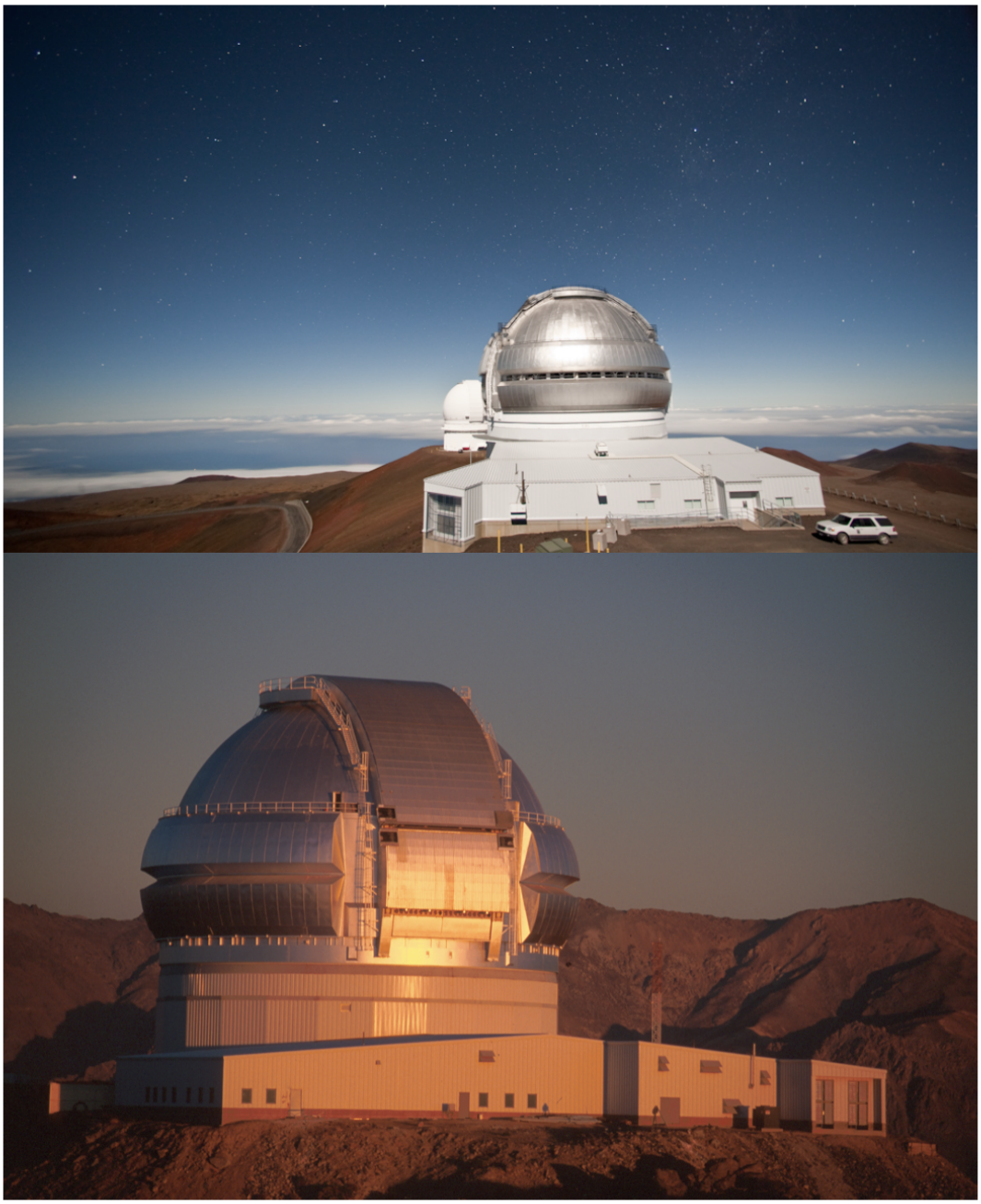

Figure 2.4 Domes hosting Gemini North (*upper panel*) on Hawaii's Mauna Kea and Gemini South (*lower panel*) on Cerro Pachón.

2.1.4 *Chandra* X-ray Observatory (CXO)

The *Chandra* X-ray Observatory (CXO, see Figure 2.5), born as Advanced X-ray Astrophysics Facility (AXAF), operated by NASA, was designed to detect X-ray photons in the energy range 0.1-10 keV from astronomical sources, and launched in 1999. Given the high energy of these particles, mirrors (4 paraboloid and hyperboloid pair) are shaped and aligned nearly parallel to incoming X-rays, to obtain a grazing incidence. There are four instruments on board of the spacecraft: the Advanced CCD Imaging Spectrometers (ACIS-I and ACIS-S) and the High Resolution Camera (HRC) in the focal plane, and the High and Low Energy Transmission Grating Spectrometer (HETGS and LETGS, respectively). In the works presented in this thesis, I made use of ACIS-S data. *Chandra* ACIS detectors are characterized by an unmatched spatial resolution (0.5″) with respect to other X-ray telescopes, and a low background. X-ray photons collected on ACIS are detected individually and their position, energy and arrival time are recorded. The effective area of the instrument is stored in the arf (ancillary response file; see Figure 2.6), while the spectral energy distribution, that assigns a specified energy to photons detected in each channel, is stored in the rmf (redistribution matrix file).

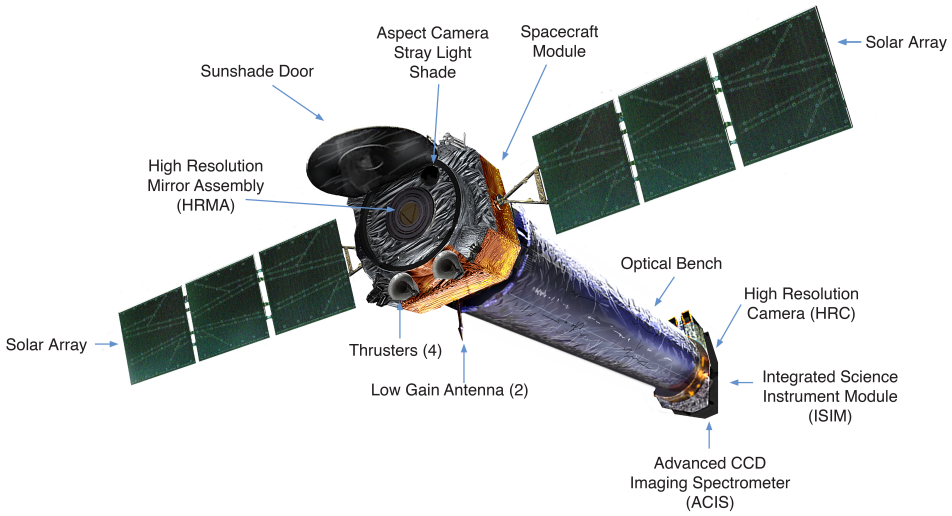

Figure 2.5 *Chandra* spacecraft and instruments. See Section 2.1.4 for more details.

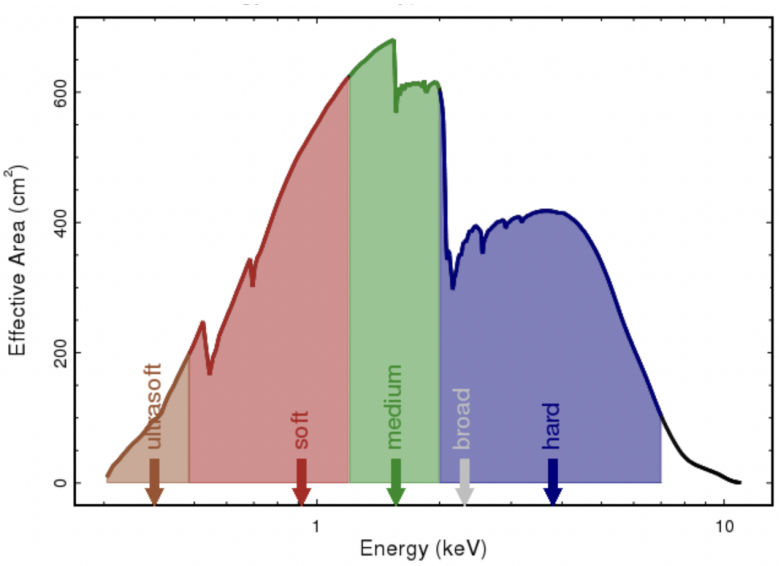

Figure 2.6 *Chandra* nearly on axis ACIS arf. The arrows identify the monochromatic energy used with each band: ultrasoft (0.2-0.5 keV) with a monochromatic energy of 0.4; soft (0.5-1.2 keV) @ 0.92 keV; medium (1.2-2.0 keV) @ 1.56 keV; hard (2.0-7.0 keV) @ 3.8 keV. Broad band goes from 0.5 to 7.0 with a monochromatic energy of 2.3 keV.

2.2 Data Reduction Procedures

This Section is devoted to the description of the data reduction and analysis procedures adopted in the works presented in Chapter 3.

2.2.1 Radio Frequencies

Radio maps of 3CR unidentified sources

Calibration and imaging were performed in CASA[1] v5.1.1-5 (McMullin et al. 2007) adopting manual standard procedures. For the sources presented in Section 3.2, if available, I reduced observations in L, C and X radio bands (at 1.5, 6 and 10 GHz nominal frequencies, respectively). For all bands, after inspecting the observation log, I manually flagged antennas with bad data. Then, I performed the calibration adopting the following steps: 1) I provided a flux density value for the amplitude calibrator, 2) I derived corrections for the complex antenna gains, 3) I used the flux calibrator to determine the system response to a

[1] https://casa.nrao.edu/

source of known flux density and finally 4) I applied the calibrations to the calibrators and the target. Bandpass correction is not necessary given that all observations are performed in single channel mode. As a last step, I performed self-calibration on CASA with the task *tclean*, changing the weight parameter (robust) in every step of the cleaning process to recover all the extended emission, and setting manual boxes.

Follow-up observations of 3CR 403.1 at high radio frequencies

Data reduction and imaging of 3CR 403.1 (see details in Section 3.3) were performed using the SCUBE software package (Murgia et al. 2016), according to standard procedures. Corrections for both the variation of telescope gain and atmosphere opacity with elevation were applied. In the case of 3CR 403.1, about 6% of the data were flagged because affected by the Radio Frequency Interference (RFI) both in the frequency and time-domain. The flux density was brought to the scale of Perley & Butler (2017) using the calibrators 3C 147 and 3C 286. The latter was also used as absolute reference for the linear polarization position angle. Calibration for the on-axis instrumental polarization was also performed, using the radio source 3C 84 (J0319+4130) which is assumed to be virtually unpolarized[2].

Baseline emission was removed from each individual sub-scan by fitting a 2nd-order polynomial to the "cold-sky" region around 3CR 403.1. To this aim, the emission from the entire radio source was masked using a circular region of $9.5'$ in diameter, and the NRAO VLA Sky Survey (NVSS) image was also used to identify and mask the point sources in the field of view. Then the best-fit polynomial model obtained from the unmasked portions of the image was subtracted from the original sub-scan data. In this way, the unwanted contributions from the receiver noise, the atmospheric emission, and the large-scale foreground sky emission were removed, retaining the target emission only.

Spectral cubes of the full-Stokes parameters R, L, U and Q using a pixel size of $15''$ were produced. To reduce the scanning noise, R.A. and Dec. images of all the seven feeds were combined using the wavelet stacking algorithm described in Murgia et al. (2016). To further

[2] https://science.nrao.edu/facilities/vla/docs/manuals/obsguide/modes/pol

increase the sensitivity, all spectral channels were averaged to produce the final images of total intensity and polarization (see Figure 3.17).

2.2.2 Optical Observations of Companion Galaxies around 3C 297

The data reduction was carried out following a sequence of PYRAF Gemini/GMOS routines. Biases and flatfields were reduced using the tasks GBIAS and GSFLAT. Spectra for science targets and the CuAr lamps were processed with the GSREDUCE task. The GSWAVELENGTH routine was used to derive the wavelength calibration from the CuAr frames that were applied to the science spectra with GSTRANSFORM. Sky subtraction was performed with GNSSKYSUBTRACT and final 1-D spectra extraction was carried out with the routine GSEXTRACT.

Flux calibration was achieved using GMOS longslit observations of the spectroscopic standard star *Feige66* made during the observing run. All spectra were flux calibrated and extinction corrected with the GSCALIBRATE task. Lastly, all 1D spectra were combined into a single spectrum for each target using GEMCOMBINE.

In order to measure the flux, centroid position and full-width at half maximum (FWHM) of the emission lines, Gaussian functions were fitted to individual lines, or to sets of blended lines, using PYTHON scripts written by our team. Usually, one or two Gaussian components were used to reproduce the observed profile. The criterion for the best solution was the minimum value of the reduced χ^2.

Typically, one Gaussian is needed to properly fit the observed lines but in the case of 3C 297 two components were used to fit [O II]. Throughout this process, the underlying continuum emission was approximated by a linear fit. Figure 3.30 shows examples of the Gaussian fitting for [Ne V] and [O II]. Table 3.9 lists the integrated emission line fluxes of all lines measured at a 3σ level, the centroid position and the FWHM. Notice that all lines but Mg II and [O II] broad are spectroscopically unresolved (the instrumental FWHM is 6.8 Å.)

2.2.3 X-ray Energies

Chandra data reduction and analysis have been carried with the *Chandra* Interactive Analysis of Observations (CIAO; Fruscione et al. 2006) following the standard procedures and threads[3], complemented with the use of the *Chandra* Calibration Database (CALDB). Images are all produced according to the same procedure followed for all observations of the 3CR *Chandra* Snapshot Survey (see e.g., Massaro et al. 2015, for more details). Level 2 event files were created using the CIAO task CHANDRA_REPRO.

Astrometry

For the unidentified 3C sources presented in Section 3.2, the astrometric registration between radio and X-ray images was performed by aligning the X-ray position of each core with that of the radio images, as in previous papers on the 3CR *Chandra* Snapshot Survey (see Massaro et al. 2011; Massaro et al. 2012; Massaro et al. 2018; Stuardi et al. 2018). In Table 3.3 radio/X-ray shift is reported, that for all sources is less than $2''$, corresponding to $\sim 90\%$ of the Chandra Point-Spread Function (PSF). 3CR 409 is the only source out of the seven presented in this work that could not be registered due to the lack of a radio core detection. Wide-field Infrared Sky Explorer (WISE) and Panoramic Survey Telescope & Rapid Response System (Pan-STARRS) datasets are not registered to the radio position, as done for the X-ray data, thus small shifts (i.e., less than $\sim 1''$) may be seen when overlaying radio contours on IR and optical images, consistent with their astrometric uncertainty[4] [5] and seeing in the Pan-STARRS case (Magnier et al. 2020). However this does not affect associations of radio and X-ray nuclei with their mid-IR and optical counterparts since below $\sim 1''$ the chance probability of a spurious association is less than 0.1% (see e.g., Massaro et al. 2014; D'Abrusco et al. 2019, for details).

[3] http://cxc.harvard.edu/ciao/threads/
[4] https://wise2.ipac.caltech.edu/docs/release/allwise/
[5] https://panstarrs.stsci.edu

In the case of 3C 297 (see Section 3.4), instead, after the removal of the flares from lightcurves[6], new Chandra data absolute astrometry was registered using as a reference the coordinates of the radio hotspot as detected in the 8.44 GHz VLA observation (A configuration, 1990 May 10th), reported in Stuardi et al. (2018). Each Chandra X-ray image was smoothed with a Gaussian kernel with 1x1 image pixel sigma and I evaluated the centroids of the X-ray emission using a circular region with a radius of $1''$ centered on the brightest pixel of the hotspot as imaged by Chandra. Finally, I registered each observation in order to match the X-ray hotspot centroids with the coordinates of the radio hotspot using the WCS_UPDATE CIAO task. After the registration, the observations were merged using the CIAO task MERGE_OBS.

X-ray photometry of nuclei of radio galaxies: 3CR unidentified sources & 3C 297

I used unbinned and unsmoothed X-ray images restricted to the 0.5 - 7 keV band to search for the X-ray nuclei of the 3CR unidentified sources. X-ray detection significance, reported as Gaussian equivalent standard deviation (σ), was estimated measuring the number of photons in both the nuclear region, if present, and a background region. The background region was chosen to be a circular aperture with a radius of $10''$, i.e. 5 times larger in radius than the one used for the X-ray detection of nuclei, and located far enough from the radio galaxy (i.e., at least a few tens of arcsec) to avoid the off-axis degradation of the Point Spread Function (PSF) on Charge Coupled Device (CCD) borders and contamination from the source, if extended. Adopting a Poisson distribution for the number of photons in the background, I computed the level of significance for X-ray excesses associated with the position of radio cores, if any. For 3CR 409, where no registration was possible, I centered the nuclear regions at the position corresponding to the emission peak in the 4 - 7 keV band.

[6] https://cxc.harvard.edu/ciao/ahelp/deflare.html

I also created flux maps in the X-ray energy ranges: 0.5 – 1 keV (soft), 1 – 2 keV (medium), 2 – 7 keV (hard), taking into account both exposure maps and effective areas. To this end, I used monochromatic exposure maps set to the nominal energies of 0.75, 1.4, and 4 keV for the soft, medium and hard band, respectively. All flux maps were converted from units of counts $\mathrm{cm}^{-2}\,\mathrm{s}^{-1}$ to cgs units by multiplying each map pixel by the nominal energy of each band. I made the necessary correction to recover the observed $\mathrm{erg}\,\mathrm{cm}^{-2}\,\mathrm{s}^{-1}$, when performing X-ray photometry (see e.g., Madrid et al. 2018; Hardcastle et al. 2012, for details). This is the same procedure adopted for X-ray photometry in all previous analyses of the 3CR *Chandra* Snapshot Survey (see e.g., Massaro et al. 2015; Stuardi et al. 2018; Jimenez-Gallardo et al. 2020) .

Flux maps were then used to measure observed fluxes for all the X-ray detected nuclei and extended components associated with radio structures. Uncertainties are computed assuming Poisson statistics (i.e., square root of the number-of-counts) in the source and background regions. X-ray fluxes for the cores are not corrected for the Galactic absorption, and are reported in Table 3.4.

Surface brightness profiles

For 3CR 409 and 3CR 454.2, significant diffuse X-ray emission in the 0.5 - 7 keV band, extending beyond the radio structure, was detected. Thus, to estimate the extension of this X-ray emission, I derived their surface brightness profiles.

Firstly, I detected and removed X-ray point-like sources (including the X-ray nuclei of the radio galaxies) in the 0.5 - 7 keV images using the WAVDETECT task, available in CIAO. I adopted a sequence of $\sqrt{2}$ wavelet scales, from 1 to 16 to cover different sized sources, and a false-positive probability threshold set to the value of 10^{-6}, which is the value recommended for a 1024 × 1024 image in the CIAO threads[7]. This value was chosen to ensure not to over-subtract point sources. Corresponding source regions were generated using the ROI task.

[7] https://cxc.harvard.edu/ciao/threads/wavdetect/

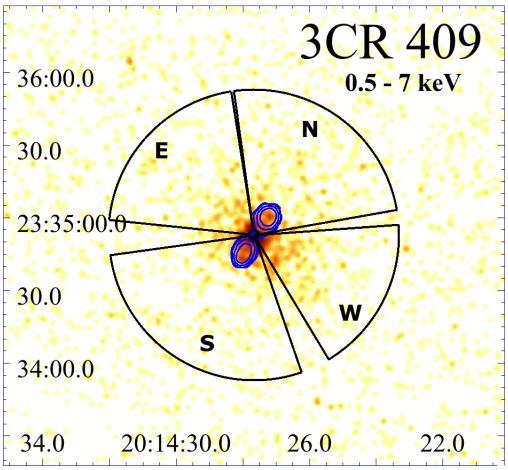

Figure 2.7 Directions used in source 3CR 409 to extract the surface brightness profiles shown in Figure 2.8. The four sectors extend up to 60″ from the core (that I have excluded, starting from a distance of 2″ from the position of the core, as reported in the NVSS, see Table 3.2). In blue VLA contours from Figure 3.9 are shown.

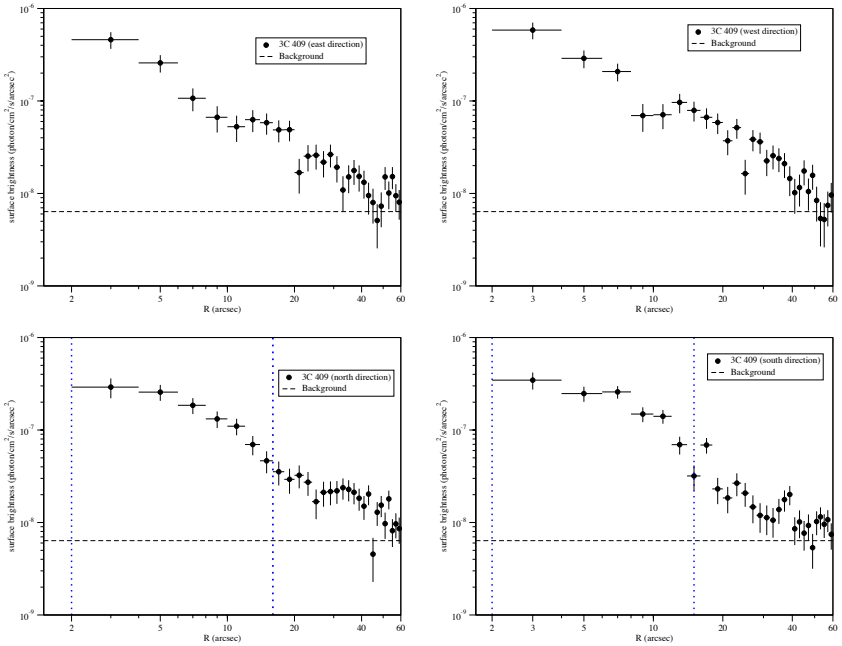

Figure 2.8 Surface brightness profiles for 3CR 409 extracted in the directions shown in Figure 2.7. Sectors are divided in bins of 2″ width. The inner and outer radii of the lobes are indicated with blue vertical dotted lines. In the eastern profile (*upper right panel*) I estimated a jump in the surface brightness between the third and fourth annulus, with 2.8σ.

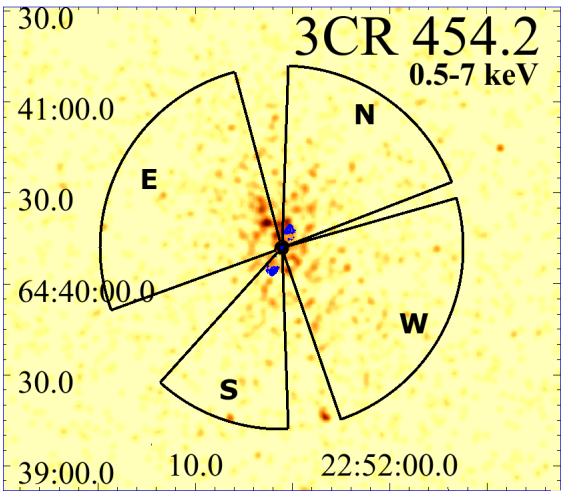

Figure 2.9 Directions used in source 3CR 454.2 to extract the surface brightness profiles shown in Figure 2.10. The four sectors extend up to 60″ from the core (that I have excluded, starting from a distance of 2″ from the position of the core, as reported in the NVSS, see Table 3.2). In blue VLA contours from Figure 3.13 are shown.

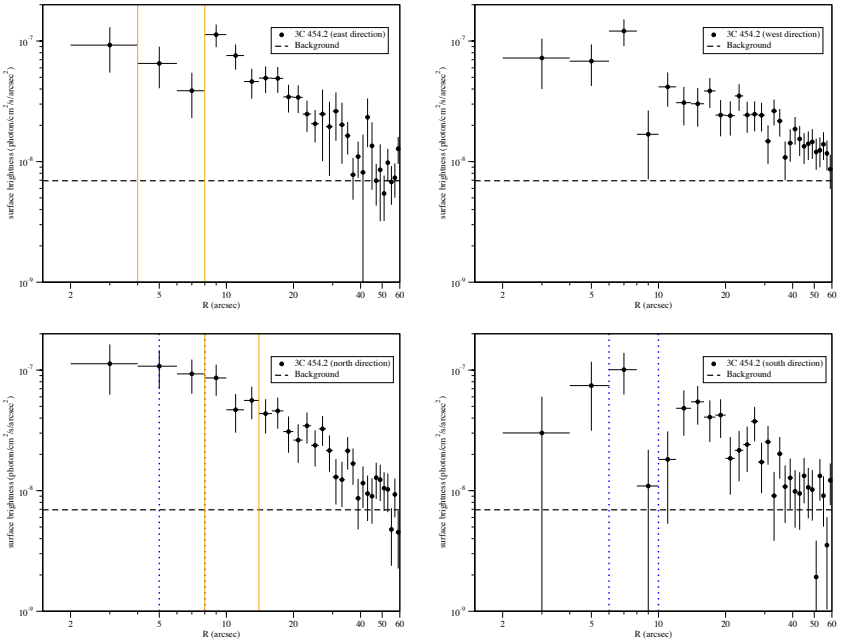

Figure 2.10 Surface brightness profiles for 3CR 454.2 extracted in the directions shown in Figure 2.9. Sectors are divided in bins of 2″ width. In the northern and southern profiles (bottom panels of Figure 2.10) inner and outer radii of the lobes are indicated with blue vertical dotted lines. In the northern and eastern profiles the areas occupied by the cavities are included between orange vertical lines.

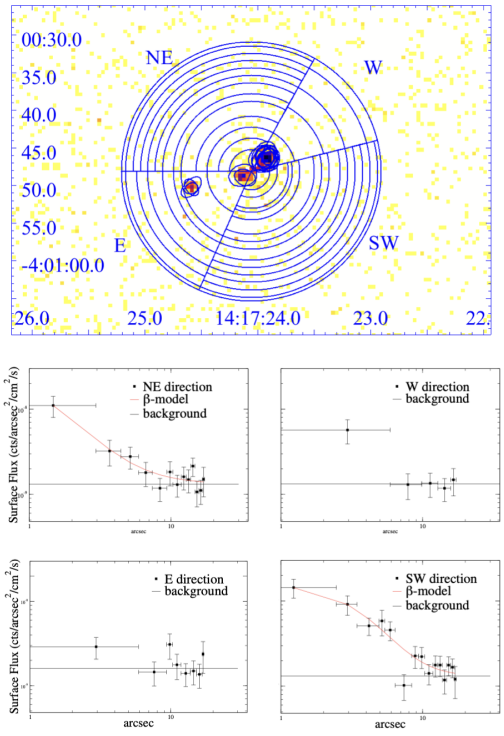

Figure 2.11 *Top Panel*: Merged *Chandra* X-ray image (0.5-7 keV) showing the annuli used to extract surface brightness profiles in four sectors. Blue ellipses represent the point sources excluded from each observation before merging the separate pointings. The source in the eastern region is unrelated. *Bottom Panel*: Surface brightness profiles for the regions highlighted in the top panel. In the western and eastern directions the emission can not be fitted with a β-model.

I computed the 0.5 - 7 keV, exposure corrected X-ray surface brightness profiles in four quadrants (north, south, east, west). The background was estimated as a circular region of $\sim 80''$ radius, far from the source, and free of detected sources. A similar procedure was used in Jimenez-Gallardo et al. (2021) to search for X-ray counterparts of radio hotspots.

In the case of 3C 297 I extracted the surface brightness profiles in four directions (see Figure 2.11) choosing sections with an outer radius of $30''$ and a signal-to-noise ratio of 3 in each radial bin. I then extracted the spectra with the SPECEXTRACT[8] script and then performed the fitting with SHERPA[9] (Freeman et al. 2001).

[8] https://cxc.cfa.harvard.edu/ciao/ahelp/specextract.html
[9] http://cxc.harvard.edu/sherpa

X-ray spectral analysis: 3CR unidentified sources & 3C 297

I performed spectral analysis for the X-ray counterparts of radio cores of four out of seven unidentified radio sources having more than 400 photons (as reported in Table 3.4), within a circular region of $2''$, centered on the radio core position (namely, 3CR 91, 3CR 390, 3CR 409 and 3CR 428) and in more extended regions corresponding to X-ray diffuse emission. This analysis was carried out to determine X-ray spectral indices α_X, the presence of significant intrinsic absorption, if any, and to estimate the temperature, abundances and density for the intracluster medium (ICM) of the two galaxy clusters detected (namely 3CR 409 and 3CR 454.2).

The spectral data for the X-ray cores were extracted from a $2''$ aperture, as for photometric measurements, using the CIAO routine `specextract`, thereby automating the creation of count-weighted response matrices. In the cases of the sources hosted in clusters, namely 3CR 409 and 3CR 454.2, I have extracted the spectrum from a circular region of $\sim 1'$ excluding a $2''$ aperture covering the nucleus. Background spectra were extracted in nearby circular regions of radius $80''$ free of detected sources. The source spectra were then filtered in energy between 0.5-7 keV and binned to allow a minimum number of 20 counts per bin to ensure the use of the χ^2 statistic. I used Sherpa (Freeman et al. 2001) modeling and fitting package to fit the spectra.

For the nuclear spectra, as performed in all the previous analyses of sources observed during the 3CR *Chandra* Snapshot Survey, I adopted an absorbed power-law model with the hydrogen column density N_H fixed at the Galactic values and a contribution of intrinsic absorption (xswabs*xszwabs*xspowerlaw). When considering the fitting model, the two main free parameters - namely the intrinsic absorption $N_{H,int}$ and the spectral index α_X - were allowed to vary, to quantify the degree to which $N_{H,int}$ and α_X are degenerate. In all cases, I adopted the photometric redshift obtained from WISE counterpart magnitudes, as described in Glowacki et al. (2017). These authors, using the WISE two-color plot (W1-W2 versus W2-W3), were able to distinguish LERGs (typically associated with passive elliptical galaxies), HERGs (associated with smaller but higher star-forming galaxies hosting radiative

Table 2.2 Results of nuclear X-ray spectral analysis of 3C unidentified.

3CR name	z	$N_{H,int}$ (10^{22}cm^{-2})	α_X	ν	χ^2_ν	Luminosity ergs^{-1}
91	0.23	$0.33^{+0.25}_{-0.23}$	0.8*	25	0.91	$1.37^{+0.12}_{-0.11} \times 10^{44}$
91	0.23	0*	0.50 ± 0.12	25	0.77	$1.23^{+0.22}_{+0.18} \times 10^{44}$
91	0.19	$0.31^{+0.23}_{-0.21}$	0.8*	25	0.91	$8.87^{+0.72}_{-0.78} \times 10^{43}$
91	0.19	0*	0.50±0.12	25	0.77	$8.07^{+1.50}_{-1.22} \times 10^{43}$
390	0.41	$0.50^{+0.18}_{-0.20}$	0.8*	45	0.86	$6.03^{+0.40}_{-0.33} \times 10^{44}$
390	0.41	0*	0.50±0.08	45	0.75	$5.45^{+0.60}_{-0.62} \times 10^{44}$
390	0.30	$0.40^{+0.16}_{-0.15}$	0.8*	45	0.86	$2.89^{+0.18}_{-0.17} \times 10^{44}$
390	0.30	0*	0.50 ± 0.08	45	0.75	$2.62^{+0.27}_{-0.25} \times 10^{44}$
409	1.04	$14.4^{+1.74}_{-1.56}$	0.8*	25	0.71	$7.51^{+0.65}_{-0.53} \times 10^{45}$
409	1.04	$11.19^{+3.00}_{-2.77}$	$0.45^{+0.28}_{-0.27}$	24	0.68	$6.22^{+3.28}_{-2.71} \times 10^{45}$
409	0.55	$6.80^{+0.76}_{-0.70}$	0.8*	25	0.68	$1.40^{+0.10}_{-0.11} \times 10^{45}$
409	0.55	$5.66^{+1.51}_{-1.41}$	$0.53^{+0.31}_{-0.30}$	24	0.68	$1.21^{+0.64}_{-0.52} \times 10^{45}$
428	2.38	$23.37^{+5.96}_{-5.64}$	0.8*	23	0.64	$4.32^{+0.40}_{-0.39} \times 10^{46}$
428	2.38	$19.89^{+16.65}_{-14.81}$	$0.71^{+0.38}_{-0.36}$	22	0.67	$4.09^{+2.66}_{-2.14} \times 10^{46}$
428	2.27	$21.49^{+5.52}_{-5.20}$	0.8*	23	0.63	$3.86^{+0.34}_{0.34} \times 10^{46}$
428	2.27	$18.37^{+14.92}_{-13.16}$	$0.71^{+0.36}_{-0.34}$	22	0.66	$3.71^{+2.49}_{-1.94} \times 10^{46}$

Col. (1): The 3CR name. Col. (2): Photometric redshifts, obtained from WISE magnitudes in 3.4 and 4.6 μm filters as described in the text, used for the spectral analysis. Col. (3): Intrinsic Absorption, $N_{\rm H,int}$, as used in the spectral model. Col. (4): X-ray Spectral index. Col. (5): Degree of freedom. Col. (6): Reduced statistic. Col. (7): Luminosity of the nucleus, obtained in SHERPA with the function SAMPLE_FLUX. Parameters fixed in the spectral fitting are indicated with *.

AGNs) and QSOs. The method described to estimate the redshift offers, therefore, also the probability of a radio source to be either a LERG, or a HERG or a QSO, using the kernel density estimation (KDE) (for more information about this method see Section 2.2 in Glowacki et al. 2017). These probabilities are used to weight the redshift estimation made for each class (see Table 2 in Glowacki et al. 2017). In Table 2.2 photometric redshifts and results of the X-ray spectral analysis of the cores are reported.

For 3CR 91, from the pileup map generated through the CIAO task PILEUP_MAP, I estimated the amount of pileup to be ~ 15%. For this reason, before performing the spectral analysis of the X-ray counterpart of the radio core, pixels most affected by the pileup (five

pixels) have been excluded, obtaining a better fit with respect to the one adopting the jdpileup [10] model.

For the spectral analysis of 3CR 403.1, I used unbinned and unsmoothed X-ray images restricted to the 0.5 - 7 keV energy range to select both source and background regions. No astrometric registration was performed since the position of the X-ray nucleus is not clearly detected (as already noticed in Jimenez-Gallardo et al. 2021). Light curves were extracted in source-free regions to check for the presence of high background intervals, that were not detected. For all analyses, blank-sky background files were used to estimate the background level at the source position. For the spectral analysis, the exposure time of the blank-sky files was adjusted so their count rates matched those of the source data in the 9.5-12 keV band (Hickox & Markevitch 2006).

For 3C 297, the spectral analysis focused on three distinct areas with sufficient counts: the northern hotspot, the extended region, and the nucleus (see Figure 2.12).

I extracted the spectrum of the hotspot within a circular aperture of $\sim 1.5''$ diameter in the reprojected observations (see Subsection 2.2.3), and combined these spectra using SPECEXTRACT CIAO tool. Adopting a model with Galactic absorption and a power-law (xstbabs.absgal*xspowerlaw.pl) setting the Galactic absorption to the value of 3.49×10^{20} cm^{-2}, as reported in HI4PI Collaboration et al. (2016), I obtained a photon index $\Gamma = 1.8 \pm 0.16$ and an X-ray luminosity of the hotspot $L_X = 2.82^{+0.57}_{-0.46} \times 10^{44}$ erg s^{-1} between 0.5-7 keV.

Then, I performed the spectral analysis of the extended emission in the south-western direction. I extracted spectra from an elliptical region (see Figure 2.12) with semi-major and minor axes of $12''$ and $7''$, respectively. The axes were selected based on the surface brightness profile in the south-western direction (see Section 3.4 for more details).

[10] https://cxc.cfa.harvard.edu/sherpa/ahelp/jdpileup.html

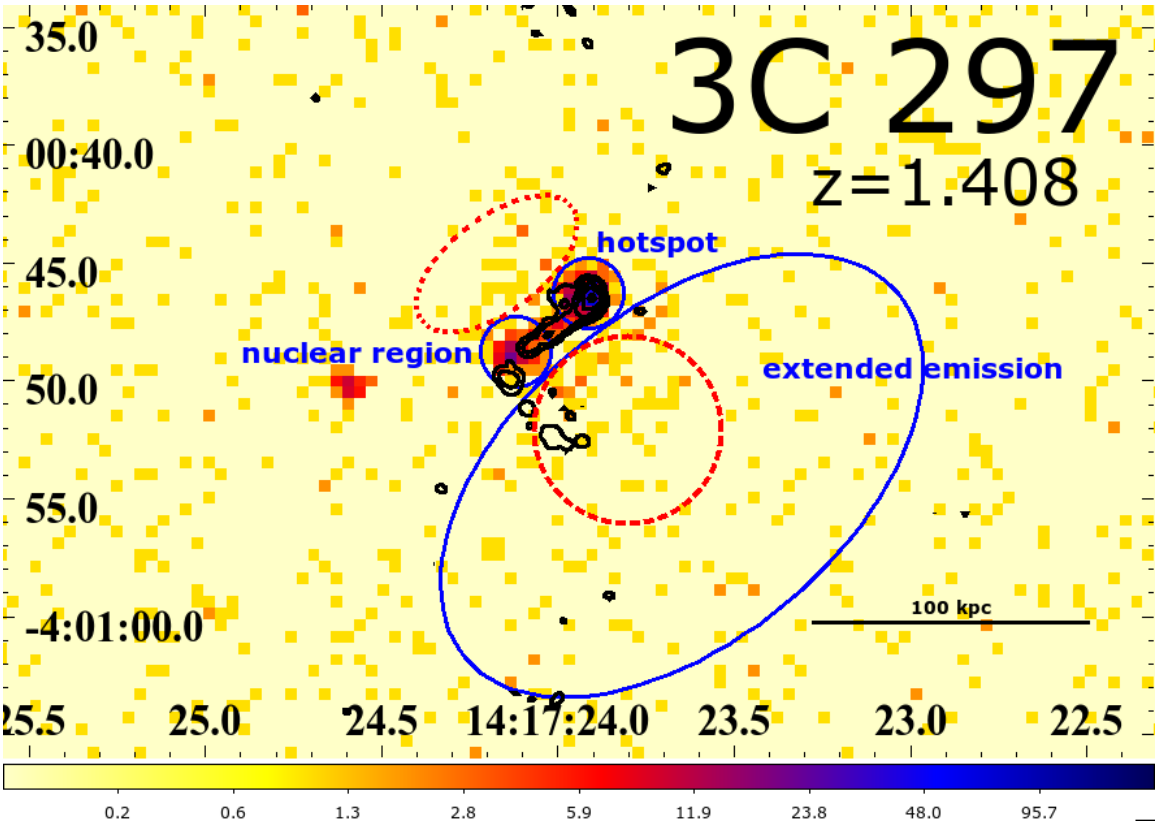

Figure 2.12 Unbinned, unsmoothed *Chandra* merged image of 3C 297 in the energy band 0.3-7 keV. The three regions in which spectral analyses have been performed are highlighted in the blue regions (two circles and one ellipse). 159 net counts are detected in the extended emission region, 115 net counts in the nuclear region and 315 net counts in the hotspot region. The red dashed circle and ellipse mark the regions in which an X-ray counts excess can be observed, due to the outflow (see Section 3.4.2 for more details).

References

D'Abrusco, R., Álvarez Crespo, N., Massaro, F., Campana, R., Chavushyan, V., Landoni, M., La Franca, F., Masetti, N., Milisavljevic, D., Paggi, A., Ricci, F., & Smith, H. A. 2019, ApJS, 242, 4

Freeman, P., Doe, S., & Siemiginowska, A. 2001, in Society of Photo-Optical Instrumentation Engineers (SPIE) Conference Series, Vol. 4477, Astronomical Data Analysis, ed. J.-L. Starck & F. D. Murtagh, 76–87

Fruscione, A., McDowell, J. C., Allen, G. E., Brickhouse, N. S., Burke, D. J., Davis, J. E., Durham, N., Elvis, M., Galle, E. C., Harris, D. E., Huenemoerder, D. P., Houck, J. C., Ishibashi, B., Karovska, M., Nicastro, F., Noble, M. S., Nowak, M. A., Primini, F. A., Siemiginowska, A., Smith, R. K., & Wise, M. 2006, in Society of Photo-Optical Instrumentation Engineers (SPIE) Conference Series, Vol. 6270, Society of Photo-Optical Instrumentation Engineers (SPIE) Conference Series, ed. D. R. Silva & R. E. Doxsey, 62701V

Glowacki, M., Allison, J. R., Sadler, E. M., Moss, V. A., & Jarrett, T. H. 2017, arXiv e-prints, arXiv:1709.08634

Hardcastle, M. J., Massaro, F., Harris, D. E., Baum, S. A., Bianchi, S., Chiaberge, M., Morganti, R., O'Dea, C. P., & Siemiginowska, A. 2012, MNRAS, 424, 1774

HI4PI Collaboration, Ben Bekhti, N., Flöer, L., Keller, R., Kerp, J., Lenz, D., Winkel, B., Bailin, J., Calabretta, M. R., Dedes, L., Ford, H. A., Gibson, B. K., Haud, U., Janowiecki,

S., Kalberla, P. M. W., Lockman, F. J., McClure-Griffiths, N. M., Murphy, T., Nakanishi, H., Pisano, D. J., & Staveley-Smith, L. 2016, A&A, 594, A116

Hickox, R. C. & Markevitch, M. 2006, ApJ, 645, 95

Jansky, K. 1933, Proceedings of the Institute of Radio Engineers, 21, 1387

Jimenez-Gallardo, A., Massaro, F., Paggi, A., D'Abrusco, R., Prieto, M. A., Peña-Herazo, H. A., Berta, V., Ricci, F., Stuardi, C., Wilkes, B. J., O'Dea, C. P., Baum, S. A., Kraft, R. P., Forman, W. R., Jones, C., Mingo, B., Liuzzo, E., Balmaverde, B., Capetti, A., Missaglia, V., Hardcastle, M. J., Baldi, R. D., & Morabito, L. K. 2021, ApJS, 252, 31

Jimenez-Gallardo, A., Massaro, F., Prieto, M. A., Missaglia, V., Stuardi, C., Paggi, A., Ricci, F., Kraft, R. P., Liuzzo, E., Tremblay, G. R., Baum, S. A., O'Dea, C. P., Wilkes, B. J., Kuraszkiewicz, J., Forman, W. R., & Harris, D. E. 2020, ApJS, 250, 7

Madrid, J. P., Donzelli, C. J., Rodríguez-Ardila, A., Paggi, A., Massaro, F., & Schirmer, M. 2018, ApJS, 238, 31

Magnier, E. A., Schlafly, E. F., Finkbeiner, D. P., Tonry, J. L., Goldman, B., Röser, S., Schilbach, E., Casertano, S., Chambers, K. C., Flewelling, H. A., Huber, M. E., Price, P. A., Sweeney, W. E., Waters, C. Z., Denneau, L., Draper, P. W., Hodapp, K. W., Jedicke, R., Kaiser, N., Kudritzki, R. P., Metcalfe, N., Stubbs, C. W., & Wainscoat, R. J. 2020, ApJS, 251, 6

Massaro, F., Harris, D. E., & Cheung, C. C. 2011, ApJS, 197, 24

Massaro, F., Harris, D. E., Liuzzo, E., Orienti, M., Paladino, R., Paggi, A., Tremblay, G. R., Wilkes, B. J., Kuraszkiewicz, J., Baum, S. A., & O'Dea, C. P. 2015, ApJS, 220, 5

Massaro, F., Masetti, N., D'Abrusco, R., Paggi, A., & Funk, S. 2014, AJ, 148, 66

Massaro, F., Missaglia, V., Stuardi, C., Harris, D. E., Kraft, R. P., Paggi, A., Liuzzo, E., Tremblay, G. R., Baum, S. A., O'Dea, C. P., Wilkes, B. J., Kuraszkiewicz, J., & Forman, W. R. 2018, ApJS, 234, 7

Massaro, F., Tremblay, G. R., Harris, D. E., Kharb, P., Axon, D., Balmaverde, B., Baum, S. A., Capetti, A., Chiaberge, M., Gilli, R., Giovannini, G., Grandi, P., Macchetto, F. D., O'Dea, C. P., Risaliti, G., Sparks, W., & Torresi, E. 2012, ApJS, 203, 31

McMullin, J. P., Waters, B., Schiebel, D., Young, W., & Golap, K. 2007, in Astronomical Society of the Pacific Conference Series, Vol. 376, Astronomical Data Analysis Software and Systems XVI, ed. R. A. Shaw, F. Hill, & D. J. Bell, 127

Murgia, M., Govoni, F., Carretti, E., Melis, A., Concu, R., Trois, A., Loi, F., Vacca, V., Tarchi, A., Castangia, P., Possenti, A., Bocchinu, A., Burgay, M., Casu, S., Pellizzoni, A., Pisanu, T., Poddighe, A., Poppi, S., D'Amico, N., Bachetti, M., Corongiu, A., Egron, E., Iacolina, N., Ladu, A., Marongiu, P., Migoni, C., Perrodin, D., Pilia, M., Valente, G., & Vargiu, G. 2016, MNRAS, 461, 3516

Perley, R. A. & Butler, B. J. 2017, ApJS, 230, 7

Prandoni, I., Murgia, M., Tarchi, A., Burgay, M., Castangia, P., Egron, E., Govoni, F., Pellizzoni, A., Ricci, R., Righini, S., Bartolini, M., Casu, S., Corongiu, A., Iacolina, M. N., Melis, A., Nasir, F. T., Orlati, A., Perrodin, D., Poppi, S., Trois, A., Vacca, V., Zanichelli, A., Bachetti, M., Buttu, M., Comoretto, G., Concu, R., Fara, A., Gaudiomonte, F., Loi, F., Migoni, C., Orfei, A., Pilia, M., Bolli, P., Carretti, E., D'Amico, N., Guidetti, D., Loru, S., Massi, F., Pisanu, T., Porceddu, I., Ridolfi, A., Serra, G., Stanghellini, C., Tiburzi, C., Tingay, S., & Valente, G. 2017, A&A, 608, A40

Stuardi, C., Missaglia, V., Massaro, F., Ricci, F., Liuzzo, E., Paggi, A., Kraft, R. P., Tremblay, G. R., Baum, S. A., O'Dea, C. P., Wilkes, B. J., Kuraszkiewicz, J., Forman, W. R., & Harris, D. E. 2018, ApJS, 235, 32

Chapter 3

Powerful Radio Galaxies in the Northern Hemisphere

In this chapter I present the multi-wavelength analysis performed on radio sources from the Third Cambridge Catalog (3C). In Section 3.1 I give an overview on the brightest low-frequency-selected AGN sample, the 3C, while in Section 3.2 results of multi-wavelength observations of seven extragalactic radio sources, listed as unidentified in the 3C, are reported. X-ray observations, performed during *Chandra* Cycle 21, were compared to VLA, WISE and Pan-STARRS observations in the radio, infrared and optical bands, respectively. Sections 3.3 and 3.4 are devoted to the follow-up observations of the sources 3CR 403.1 and 3C 297. 3CR 403.1 is a nearby (z=0.055), extended (~0.5 Mpc) radio galaxy hosted in a small galaxy group, for which I obtained new high frequency radio observations from the Sardinia Radio Telescope (SRT), that augmented with archival low frequency radio observations allowed me to perform a multifrequency analysis of the galaxy properties. 3C 297 is a high-redshift quasar (z=1.408), that I speculate is a fossil group because of the presence of a X-ray halo and the absence of companion galaxies.

Unless otherwise stated, cgs units are adopted for numerical results, and a flat cosmology with H_0 = 69.6 km s^{-1} Mpc^{-1}, Ω_M = 0.286 and Ω_Λ = 0.714 (Bennett et al. 2014) is assumed. Spectral indices, α_X, are defined by flux density, $S_\nu \propto \nu^{-\alpha_X}$.

3.1 Third Cambridge Catalog of Radio Sources

The Third Cambridge Catalog (3C) of radio sources is a northern hemisphere sample of radio galaxies and quasars, originally detected at 159 MHz. Its first edition was published in 1959 (Edge et al. 1959), while two revised versions were released in 1962 (i.e., the 3CR, Bennett 1962) and later in 1983 (i.e., the 3CRR, Laing et al. 1983), respectively, both performed at 178 MHz with the same threshold of 9 Jy for the limiting flux density. The 3C catalog, and all its revised versions (see e.g. Spinrad et al. 1985), are still a paramount tool to study RL AGN and the interaction with their environments at all scales (i.e., feedback processes: Kraft et al. 2005; Fabian 2012; Heckman & Best 2014; Dasadia et al. 2016).

On the basis of the 3CR radio observations at 178 MHz, Fanaroff & Riley (1974) proposed a classification for radio sources based on the relative position of regions of high and low surface brightness in their extended structures, distinguishing between FR I, i.e. edge-darkened, and FR II, i.e. edge-brightened, types. Since 1974, a lot more has been learned on the FR I/FR II dichotomy, as reported in Bridle (1984); Baum et al. (1995); Chiaberge et al. (2000); Mingo et al. (2019). Between '80s and '90s, an additional classification was proposed, on the basis of the relative intensity of high and low excitation lines in the optical spectra (Hine & Longair 1979; Laing et al. 1994). Two populations of radio galaxies were then defined: high-excitation radio galaxies, or HERGs, and low-excitation radio galaxies, or LERGs. These two classes are believed to represent intrinsically different types of objects, since they show different accretion rates (Chiaberge et al. 2002; Hardcastle et al. 2009; Best & Heckman 2012), host galaxies and redshift evolution (Pracy et al. 2016).

Since the early sixties, follow up multifrequency observations began, aimed at obtaining a full overview of the 3C radio sources (Law-Green et al. 1995; de Koff et al. 1996; McCarthy et al. 1997). Initial observational campaigns carried out optical spectroscopic observations aimed at estimating the source redshifts (Minkowski 1960; Lynds et al. 1965; Sandage 1966, 1967; Smith et al. 1976; Smith & Spinrad 1980). These then evolved into more complete studies with wider broadband coverage using several telescopes (e.g., Karl G.

Jansky Very Large Array, Spitzer, Herschel, Hubble Space Telescope Harvanek & Hardcastle 1998; Chiaberge et al. 2000; Cleary et al. 2007; Podigachoski et al. 2015; Tremblay et al. 2009; Madrid et al. 2006). These campaigns were recently augmented thanks to X-ray observations of the 3CR *Chandra* Snapshot Survey started in 2008 (Massaro et al. 2010, 2013). The main aim of this high energy survey is to detect X-ray emission arising from nuclei, lobes, jet knots and hotspots, as that of the intergalactic medium for those radio sources harbored in galaxy-rich large scale environments (Madrid et al. 2018; Ricci et al. 2018; Paggi et al. 2021; Jimenez-Gallardo et al. 2021a).

3.2 3CR Unidentified Sources

Note: Section adapted from Missaglia et al. (2021).

In the *Chandra* archive, 150 out of 298 3CR extragalactic sources were already present before the beginning of the 3CR *Chandra* Snapshot Survey. 123 3CR sources have been observed as part of the Snapshot Survey, and X-ray emission has been detected in 119 out of 122 radio cores, in addition to the discovery of the X-ray counterpart for eight jet knots, 23 hotspots, with marginal detection for another nine, and 17 radio lobes (see Jimenez-Gallardo et al. 2020, for the latest run of Chandra observations). Diffuse X-ray emission was also detected around several 3C radio sources, potentially associated with either their radio lobes or radiation arising from the ICM when harbored in galaxy clusters/groups.

During the *Chandra* campaign, it was determined that 25 3CR sources out of the total 298 were optically unidentified, that is, lacking an optical counterpart of their core, and therefore have neither optical classification nor redshift (see Massaro et al. 2013). This means that there is no detected emission from the host galaxy in the optical band, and this could be due to multiple reasons. These sources might, in fact, be either high redshift quasars/radiogalaxies, or highly-absorbed/obscured lower-z active galaxies, or optically faint LERGs, that lack radiatively efficient AGN signatures in the optical emission (see Section 3.2.1 for more information on individual sources properties).

Maselli et al. (2016) carried out an optical-to-X-ray campaign, that includes data from the *Swift* Observatory. These authors found that a total of 21 out of the 25 unidentified sources observed by *Swift* have a National Radio Astronomy Observatory (NRAO) Very Large array (VLA) Sky Survey (NVSS, Condon et al. 1998) counterpart. 13 of them also show mid-infrared (IR) emission as detected in the AllWISE (Wide-field Infrared Survey Explorer mission, Wright et al. 2010) Source Catalog, and nine out of these 21 have an X-ray counterpart detected in the 0.5-10 keV energy range, above 5σ level of confidence.

Here I present the results of *Chandra* follow-up observations for seven of the nine unidentified 3C sources with the *Swift* X-ray counterpart, all observed in 2020. The two remaining sources have been observed in April 2021 and are still unpublished.

I also present, for the first time, radio observations available for the selected sample in the historical VLA archive. Both radio and X-ray observations are also compared with data collected with the Panoramic Survey Telescope & Rapid Response System (Pan-STARRS, Chambers et al. 2016) and Wide-field Infrared Survey Explorer (WISE, Wright et al. 2010). WISE magnitudes in the nominal bands at 3.4 (W1), 4.6 (W2), 12 (W3), and 22 (W4) μm are in the Vega system while Pan-STARRS1 adopts the AB magnitude system (Oke & Gunn 1983).

To search for optical and infrared counterparts of the selected targets, I firstly retrieved all radio observations from the historical VLA archive, managed by the NRAO, aiming at detecting their radio cores. A summary of all radio observations is presented in Table 3.1 where it is reported: (1) 3C designation, (2) NRAO observing project identification, (3) observing date, (4) spectral windows, (5) telescope configuration in which the observation was performed, (6) clean beam size, (7) surface brightness of the source, (8) peak flux of the radio image, (9) observation time on source, (10) Root Mean Square noise of the clean image and (11) contour levels used in the radio maps.

After data reduction (see Section 2.2.1), I overlaid radio contours on optical, IR and X-ray images. In Table 3.2 I report: (1) 3C designation, (2,3) coordinates in J2000 Equinox, (4) Galactic absorption as reported in Kalberla et al. (2005), (5,6) *Chandra* observation ID

Table 3.1 Summary of radio observations of 3C unidentified sources.

3CR Name	NRAO ID	Obs. Date yyyy-mm-dd	Frequency (GHz)	Configuration	Beam size ($arcsec^2$)	Total Flux (Jy)	Peak Flux (Jy/beam)	TOS (s)	RMS (σ) (10^{-3}Jy/beam)	contour levels (σ)
91	AH976	2008-10-09	8.44, 8.49	AB	1 × 0.5	0.63±0.06	4.25×10^{-2}	70	1.4	6, 8, 16, 32, 64, 72, 74, 78
-	AP001	1986-09-15	1.45	B	5.1 × 4.2	3.39±0.17	1.43	150	1.23	9, 27, 81, 243, 729, 1162
131	AH976	2008-10-09	8.44, 8.49	A	0.28 × 0.22	0.36±0.04	1.28	70	0.33	5, 20, 80, 320, 1280, 5120
-	AP001	1986-09-15	1.45	B	7 × 6	2.8±0.14	1.3	150	2.8	4, 8, 16, 32, 64, 128, 256, 512
158	AH976	2008-10-09	8.44, 8.49	A	0.22 × 0.20	0.63±0.03	1.28×10^{-1}	70	0.44	3, 9, 27, 81, 243
-	AR069	1983-10-13	4.84, 4.89	A	0.5 × 0.4	0.58±0.03	1.57×10^{-1}	260	0.29	3, 6, 12, 24, 48, 96, 192, 384, 548
-	AF156	1989-07-21	4.84, 4.89	BC	5.52 × 4.17	0.58±0.03	3.93×10^{-1}	310	0.17	5, 9, 27, 81, 243, 729, 2187, 2258
390	AT147	1993-03-24	4.84, 4.89	B	1.3 × 1.2	1.17±0.06	3.04×10^{-1}	370	0.10	10, 40, 160, 640, 2560
-	AK100	1984-02-27	1.41, 1.64	B	4.1 × 3.5	4.42±0.22	2.145	400	0.69	8, 16, 32, 64, 128, 256, 512, 1024, 2048, 3110
-	AP001	1986-11-28	1.45	C	23.9×16.6	4.6±0.23	2.4×10^{-1}	210	2.8	6, 12, 24, 48, 96, 192, 384, 768, 1536
409	AP001	1986-09-15	1.45	BC	3.5 × 3.1	12.54±0.63	2.06×10^{-1}	190	4	5, 20, 80, 320, 1280
-	AC169	1986-08-09	1.39, 1.42, 1.46, 1.51, 1.63, 1.66	B	-	-	-	980	-	-
428	AF102	1985-07-30	4.84, 4.89	C	6.4 × 3.5	0.51±0.02	2.06	300	0.26	2, 4, 8, 16, 32, 64, 128, 512, 1024, 8000
-	AH147	1984-09-19	1.45, 1.5	D	43.2 × 38	2.16±0.11	1.17	4680	0.45	6, 12, 24, 48, 96, 192, 384, 768, 1536, 3072
454.2	AH976	2008-10-09	8.44, 8.49	A	0.34 × 0.28	0.25±0.02	1.11×10^{-2}	80	0.29	3, 6, 12, 24, 38
-	AS238	1985-07-14	4.84, 4.89	C	5.7 x 4	0.66±0.03	1.82×10^{-1}	270	0.27	6, 12, 24, 48, 96, 192, 384, 674

Col. (1): The 3CR name. Col. (2): The NRAO observing project (or proposal) identification. Col. (3): Date of the observation. Col. (4): Frequency of the VLA observation. Col. (5): Array configuration. Col. (6): Size of the elliptical clean beam (major axis × minor axis). Col. (7): Total flux of the source, as obtained from the self-calibration. Col. (8): Peak flux of the radio image. Col. (9): Observation Time On Source (TOS). Col. (10): Root Mean Square (RMS) noise of the clean image. Col. (11): Contours levels in units of RMS.

Table 3.2 Summary of X-ray observations of 3C unidentified sources.

3CR name	R.A. (J2000) (hh mm ss)	Dec. (J2000) (dd mm ss)	$N_{H,Gal}$ ($10^{21}cm^{-2}$)	*Chandra* Obs. ID	Obs. date yyyy-mm-dd	Exposure (ks)	S_{178} (Jy)	Counterpart	Radio nucleus	Cluster
91	03 37 43.032	+50 45 47.622	4.88	22626	2019-11-18	18.9	14.1	IR, opt	yes	no
131	04 53 23.337	+31 29 27.826	2.36	22627	2019-12-29	23.8	14.6	IR	yes	no
158	06 21 41.041	+14 32 13.035	4.95	22629	2020-01-10	23.75	18.1	IR, opt	yes	no
390	18 45 37.601	+09 53 44.998	3.00	22630	2020-02-28	19.8	21.0	IR, opt	yes	no
409	20 14 27.74*	+23 34 58.4*	2.49	22631	2019-11-29	19.81	76.6	IR	no	yes
428	21 08 21.985	+49 36 41.820	10.9	22632	2019-12-23	20.79	16.6	IR	yes	no
454.2	22 52 05.530	+64 40 11.940	7.48	22633	2019-11-17	19.8	8.8	IR	yes	yes

Col. (1): The 3CR name. Col. (2-3): The celestial positions obtained from the radio images (the only exception is 3CR 409 where I used the NVSS counterpart coordinates). Col. (4): Galactic Neutral hydrogen column densities $N_{H,Gal}$ along the line of sight (Kalberla et al. 2005). Col. (5): The *Chandra* observation ID. Col. (6): The date when the *Chandra* observation was performed. Col. (7): Exposure time in ks, as reported in the *Chandra* Archive. Col. (8): S_{178} is the flux density at 178 MHz, from Spinrad et al. (1985). Col. (9-11): Remarks of the results of this work.

and date, (7) exposure time in ks, (8) flux at 178 MHz retrieved from Spinrad et al. (1985), (9-11) remarks on the sources.

3.2.1 Results and Details on Individual 3C Unidentified Sources

For all the unidentified 3CR sources presented here, I also show radio contours with band and configuration at which the observation was performed: L band (1.5 GHz), C band (6 GHz) and X band (10 GHz), in A (maximum baseline, B_{max}, equal to 35 km), B (B_{max}=10 km), C (B_{max}=3.5 km) or D (B_{max}=1 km) configuration. In the bottom left corner of each radio map, the clean beam is shown as a black filled ellipse.

3CR 91

From the historical VLA archive, I retrieved radio observations of 3CR 91 performed at 1.4 and 8 GHz in B and AB configurations, respectively. In the 8 GHz image (see red contours in Figure 3.1 and right panel of Figure 3.2) the radio core is clearly detected (i.e., above 5σ confidence level), while in the VLA image at 1.4 GHz (see Figure 3.2, left panel) the radio core is not visible. 3CR 91 is a double-lobed radio source in the VLA image at 1.4 GHz.

On the other hand, in the 8 GHz radio map, the emission arising from the southern radio lobe, clearly seen at lower frequencies, is not detected, but the northern lobe resembles an FR II radio galaxy.

I found both the IR and the optical counterpart of the radio core in the Pan-STARRS and WISE images, as shown in the left panel of Figure 3.1. The WISE counterpart to the core, J033743.02+504547.6, detected in all IR filters, is clearly the same object found within the *Swift* XRT uncertainty circle, at small angular separation ($1.4''$) from its radio position. This source, as reported in Maselli et al. (2016), has an associated NVSS counterpart, J033743+504552. The WISE counterpart is included in D'Abrusco et al. (2014) all-sky catalogue of infrared selected, radio-loud active galaxies, due to its peculiar infrared colors, and also in D'Abrusco et al. (2019). Since 3CR 91 has a WISE counterpart, adopting the method described in Glowacki et al. (2017), I was able to obtain a photometric redshift

estimate of $z = 0.23 \pm 0.18$ from the 3.4 μm magnitude, and an estimate of $z = 0.19^{+0.18}_{-0.14}$ from the 4.6 μm magnitude, with 82% probability of being a QSO. In the *Chandra* image (Figure 3.1, right panel), there is a clear detection of the radio core in the 0.5-7 keV energy range. 3CR 91 also shows extended X-ray emission up to ~9″ from the nucleus. I did not detect any X-ray counterpart for hotspots and lobes.

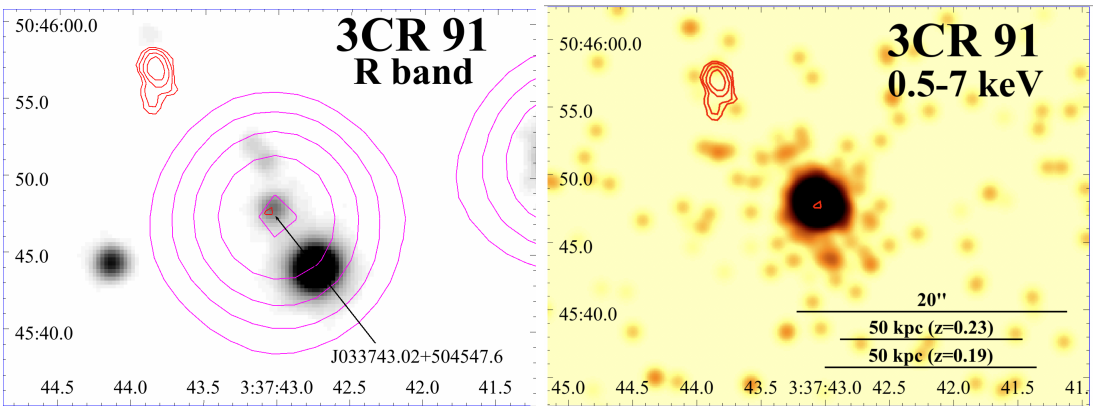

Figure 3.1 *Left Panel*: Pan-STARRS R band image with WISE 3.4 μm filter magenta contours of the IR counterpart of the radio source overlaid. IR contours are drawn at 12.54, 16.91, 22.89, 31.07 and 42.27 in arbitrary flux scale. In red, 8 GHz VLA contours are shown, the same used in the *Chandra* image. The four radio contour levels were computed starting at 0.01 Jybeam^{-1}, increasing by a factor of 2. The arrow points to the WISE counterpart of the radio core. *Right panel*: 0.5-7 keV *Chandra* image of 3CR 91 with VLA 8 GHz contours overlaid. The image has not been rebinned, but smoothed with a 3 pixel (equivalent to 1.48″) Gaussian kernel. In the bottom right of the image, kpcscale measured using the photometric redshifts obtained using the method described in Glowacki et al. (2017) are indicated.

Since for 3CR 91 the number of photons within a circular region of 2″ radius, centered on the radio position, is larger than 400, I carried out a nuclear X-ray spectral analysis. I adopted an absorbed power-law model with the hydrogen column density N_H fixed at the Galactic value (see Table 3.2, (4) column). As reported in Table 2.2, for both photometric redshifts, I obtained the best fit values setting $N_{H,int}$ as free parameter, obtaining a value $\sim 10^{23}$ cm^{-2}, similar to that of the Galactic N_H. Since 3CR 91 is a moderate-z QSO, I did not expect a detection of the optical counterpart, in agreement with my results.

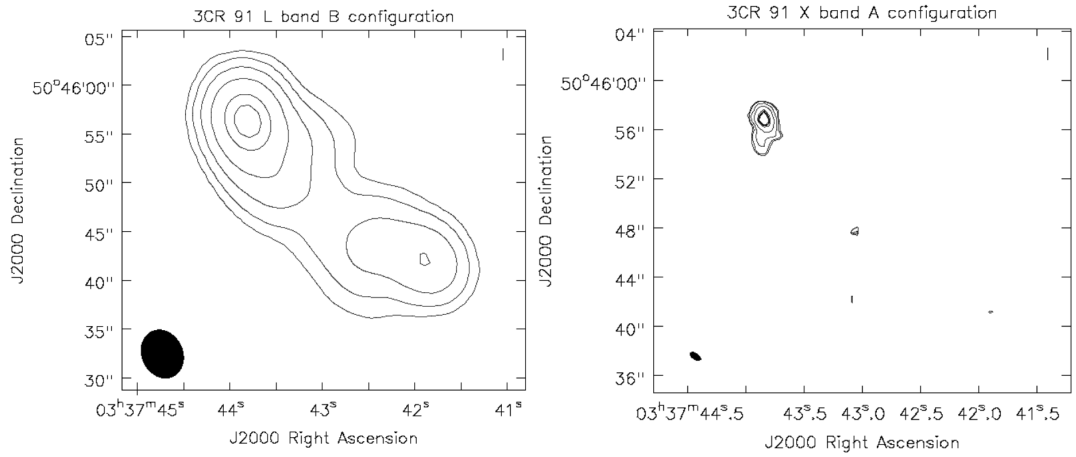

Figure 3.2 Radio VLA contours of 3CR 91. The name of the source, the observing band, and array configuration are reported on the top of each panel. The clean beam is shown as a black filled ellipse in the bottom left of the image. Radio contours levels are reported in the last column in Table 3.1. On the top of each panel, name, band and configuration are reported.

3CR 131

For 3CR 131, I reduced VLA data at 8 GHz (see red and blue radio contours in Figure 3.3, both panels) and at 1.4 GHz (see Figure 3.4 right panel). In the 8 GHz image, I detected the emission of both lobes and the nucleus, at 5 times the rms noise level, and a single radio hotspot in the southern lobe. The presence of the northern hotspot could suggest that 3CR 131 is an FRII radio galaxy. Using the method described in Glowacki et al. (2017), I obtained a photometric redshift estimate of $z = 0.41^{+0.13}_{-0.12}$ from the 3.4 μm magnitude value, and an estimate of $z = 0.4 \pm 0.13$ the 4.6 μm magnitude, and a 59% probability for this source to be a LERG.

I found the nuclear counterpart of 3CR 131 only in the IR image. In WISE W_1 filter (3.4 μm) image (see Figure 3.3, left panel), there are two nearby objects at angular separation $4''$ ~ from the position of NVSS J045323+312924 (Maselli et al. 2016). Only one object, WISE J045323.34+312928.4 (indicated by an arrow in Figure 3.3 left panel), is within the positional uncertainty of the *Swift*-XRT source. This WISE source is cospatial

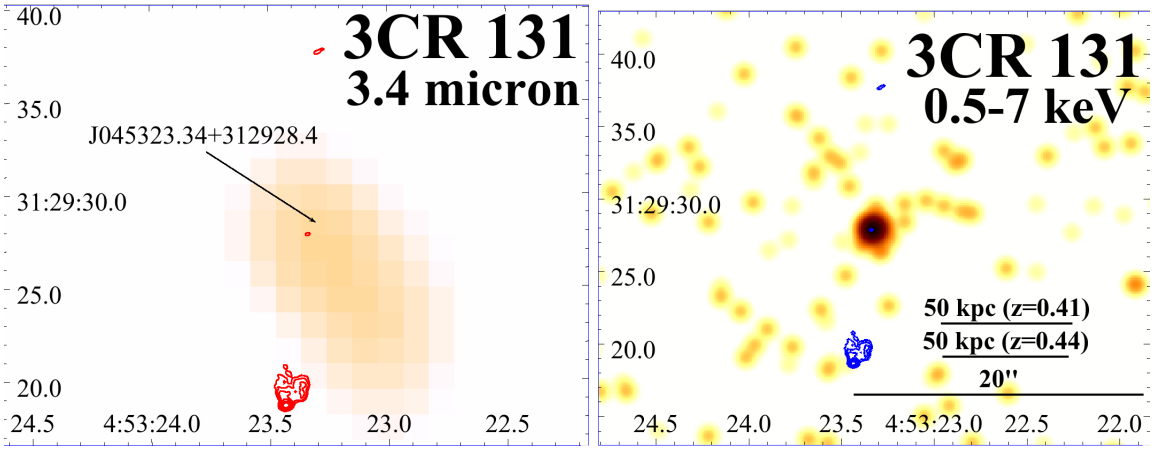

Figure 3.3 *Left panel*: WISE 3.4 μm filter image of 3CR 131. The arrow points to the IR counterpart of the radio nucleus. No optical counterpart has been detected for this source. The six VLA 8 GHz radio contours levels (red) starts from 0.002 Jybeam^{-1} and are increased by a factor of 2. *Right panel*: 0.5-7 keV *Chandra* image of 3CR 131, with VLA 8 GHz band contours overlaid in blue. *Chandra* image is not rebinned, but has been smoothed with a 5 pixel (2.46″) Gaussian kernel. In the bottom right of the image, kpcscale measured using the photometric redshifts obtained using the method described in Glowacki et al. (2017) are indicated.

with the position of the nucleus in the 8 GHz radio map, and it is therefore likely its IR counterpart.

In the *Chandra* image (Figure 3.3, right panel) the core is clearly detected and associated with the radio core, but the southern hotspot is not detected in the 0.5 - 7 keV energy range.

3CR 158

3CR 158, at 8 GHz, is a lobe dominated radio source (see red/cyan contours in Figure 3.5). The core is clearly detected in this band, as well as both the southern and northern lobes (see red and cyan contours in both panels of Figure 3.5 and left panel of Figure 3.6). In particular, in the northern side there are two knots and one hotspot, hint that the source could be classified as FR II. The two knots in the southern radio structure are probably part of the same lobe but are not detected in the 4.5 GHz image (see Figure 3.6 middle panel).

The core is also detected in both optical and IR images (see Figure 3.5 left panel). Maselli et al. (2016) reported that the X-ray source XRT J062141.2+143212 matches the

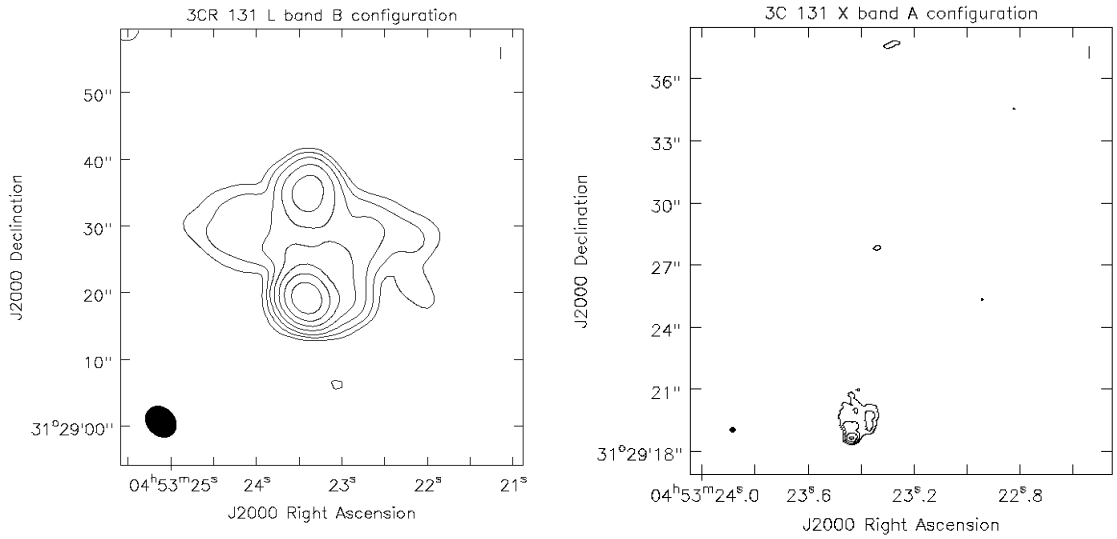

Figure 3.4 Radio VLA contours of 3CR 131. The name of the source, the observing band, and array configuration are reported on the top of each panel. The clean beam is shown as a black filled ellipse in the bottom left of the image. Radio contours levels are reported in the last column in Table 3.1.

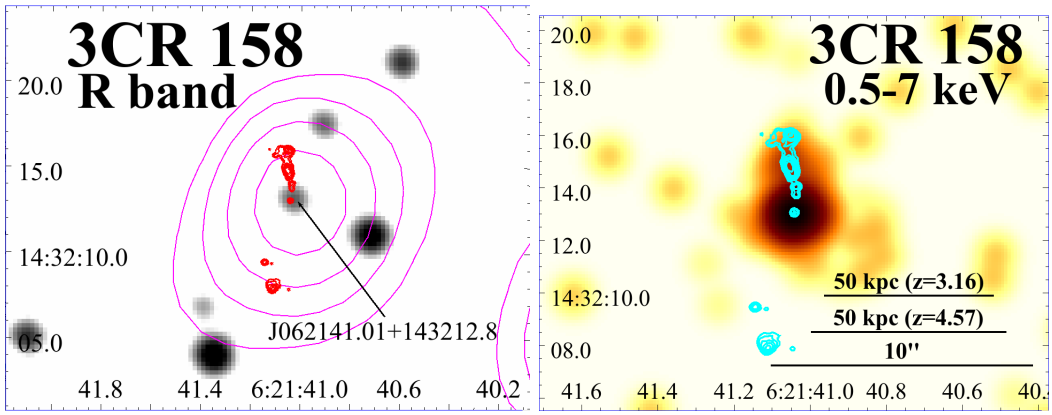

Figure 3.5 *Left panel*: Pan-STARRS R band image with WISE 3.4 μm filter magenta contours of the IR counterpart of the radio source overlaid. In red 8 GHz VLA contours are shown, the same used in the *Chandra* image (in cyan). VLA contours start from 0.002 mJ/beam, increasing by a factor of 2 up to 0.064 Jybeam^{-1}. IR contours are drawn at 13.40, 13.75, 14.21, 14.80 in arbitrary flux scale. The arrow points to the WISE counterpart of the radio core. *Right panel*: *Chandra* X-ray image of 3CR 158 in the 0.5-7 keV energy band, binned to 0.123″pixel^{-1} and smoothed with a 5 pixel Gaussian kernel (equivalent to 0.615″). The northern radio jet has a clear X-ray counterpart. In the bottom right of the image, kpcscale measured using the photometric redshifts obtained using the method described in Glowacki et al. (2017) are indicated.

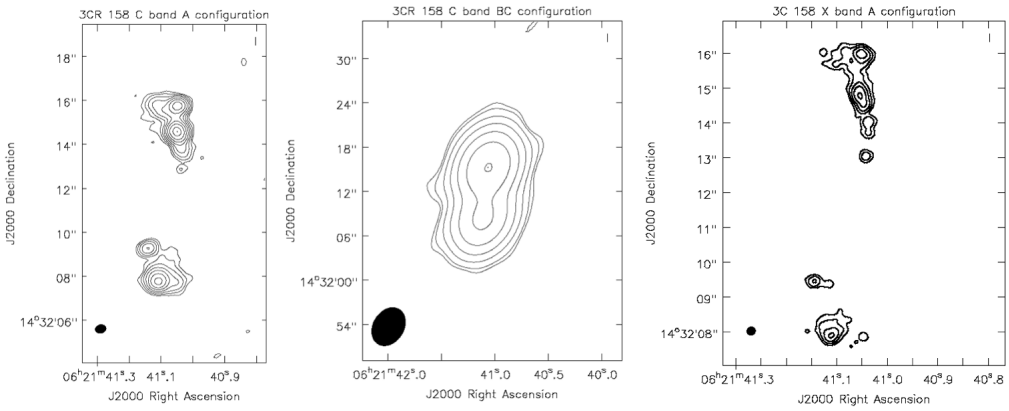

Figure 3.6 Radio VLA contours of 3CR 158. The name of the source, the observing band, and array configuration are reported on the top of each panel. The clean beam is shown as a black filled ellipse in the bottom left of the image. Radio contours levels are reported in the last column in Table 3.1.

NVSS source J062141+143211, within the 3C positional uncertainty region of 3CR 158. An infrared counterpart in the AllWISE Source Catalogue, WISE J062141.01+143212.8, is found at 1.5″ from the NVSS source, probably its counterpart (I remind that at these separations the chance probability of spurious association is below 0.1%). No infrared/optical candidate counterpart has been previously reported in the literature for this radio source. Adopting the procedure described in Glowacki et al. (2017), using the 3.4 μm WISE magnitude I obtained a photometric median redshift of $z = 4.57^{+0.68}_{-3.14}$ and using the 4.6 μm WISE magnitude, a photometric median redshift of $z = 3.16^{+2.09}_{-2.19}$, with a probability of 82% for this source of being a QSO. This is the source with the highest predicted photometric redshift of the sample. Since the Pan-STARRS counterpart is detected, even at such high redshift, a spectroscopic optical campaign is required to verify this prediction.

I found X-ray extended emission aligned with the radio jet structure in the northern side of our *Chandra* observation (see Figure 3.5 right panel). The flux of of the X-ray counterpart is $(1.51\pm0.30)\times10^{-14}\,\mathrm{erg\,cm^{-2}\,s^{-1}}$ in the 0.5-7 keV band. Given the alignment with the jet rather than the lobe, the jet is most likely the source of the X-rays.

3CR 390

3CR 390 is a lobe dominated radio source, as shown in the VLA image at 4.5 GHz (see red/blue contours in both panels of Figure 3.7 and Figure 3.8 left panel). The IR counterpart of the radio core is detected in the WISE 3.4 μm filter image (see Figure 3.7, left panel).

In the Pan-STARRS R band image, there are both an optical source corresponding to the radio core, in the same position of the WISE counterpart, and an optical source located on the position of the western radio knot (see Figure 3.7, left panel) that is likely to be a background source.

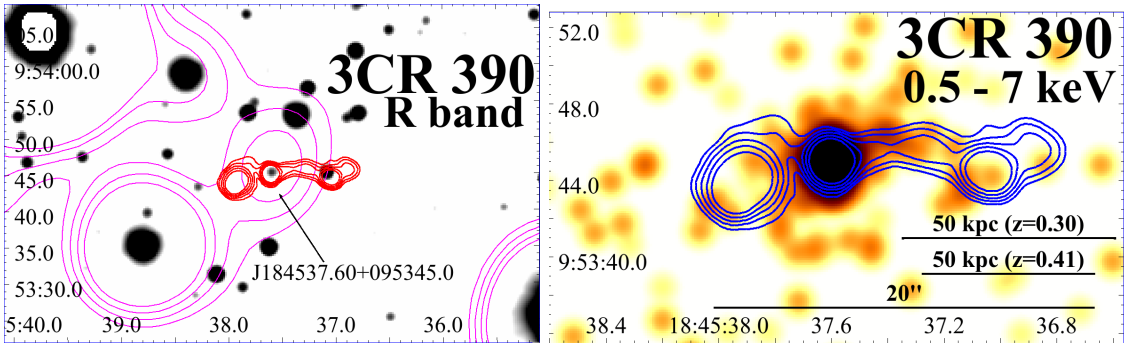

Figure 3.7 *Left panel*: Pan-STARRS R band image of the field of 3CR 390, with WISE 3.4 μm filter magenta contours overlaid. IR contours are drawn at 16.64, 19.28, 22.42, 26.15 in arbitrary flux scale. VLA red contours at 4.5 GHz are overlaid, starting from 0.002 Jy/beam and increased by a factor of two up to 0.032 Jybeam^{-1}. The black arrow points to the position of the IR counterpart of the radio nucleus. *Right panel*: *Chandra* X-ray image of 3CR 390 in the 0.5-7 keV band, binned to 0.246″pixel^{-1} and smoothed with a 5 pixel Gaussian kernel (equivalent to 1.23″). The X-ray image shows extended emission spatially coincident with the radio bridge in the western direction. In the bottom right of the image, kpcscale measured using the photometric redshifts obtained using the method described in Glowacki et al. (2017) are indicated.

To verify if the X-ray emission on the western side of the source is related to the diffuse radio emission or if it is an optical source, I measured the p-chance of the hotspot association considering the source density in a 80″ circular region around 3CR 390, taking into account the correct distance between the core and tentative hotspot. I obtained a p-chance < 4%. As reported in Maselli et al. (2016), the whole radio structure is associated with NVSS J184537+095344 and the X-ray source: XRT J184537.6+095349. The NVSS

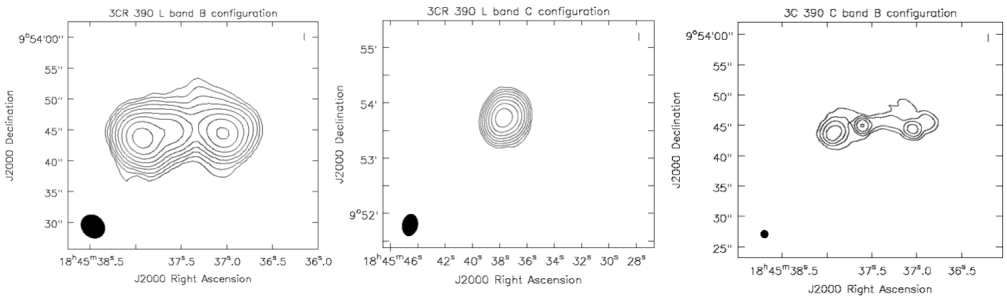

Figure 3.8 Radio VLA contours of 3CR 390. The name of the source, the observing band, and array configuration are reported on the top of each panel. The clean beam is shown as a black filled ellipse in the bottom left of the image. Radio contours levels are reported in the last column in Table 3.1.

source, not well centred with respect to the 3CR positional uncertainty region, is located within the XRT positional uncertainty region. The infrared counterpart, namely: WISE J184537.60+095345.0, was also included in the all-sky catalogue of blazar candidates by D'Abrusco et al. (2014) due to its peculiar infrared colours, and in D'Abrusco et al. (2019). Adopting the procedure described in Glowacki et al. (2017), using the 3.4 μm WISE magnitude, I obtained a photometric median redshift of $z = 0.41^{+0.28}_{-0.32}$, and using the 4.6 μm WISE magnitude a photometric median redshift of $z = 0.30^{+0.21}_{-0.25}$, with a probability of 57% for the source to be a QSO. In the *Chandra* image the core is clearly detected and I also found extended X-ray emission spatially coincident with the radio bridge connecting the two intensity peaks visible at 4.5 GHz (see Figure. 3.8 left panel). Given the large number of X-ray photons measured within 2″ circular region from the radio core position (i.e., above the threshold of 400 counts) I performed the X-ray spectral analysis. Adopting a power-law model with both Galactic and intrinsic absorption, I obtained the best fit results, for both values of the photometric redshifts, setting $N_{H,int}$ as free parameter. In these cases, I obtain an $N_{H,int}$ that is comparable with the Galactic N_H ($\sim 10^{22}$cm^{-2}), and this result is not unexpected given the detection of the optical counterpart in Pan-STARRS and the moderate-z of 3CR 390.

3CR 409

For 3CR 409, a lobe dominated radio source, I merged two VLA observations, both at 1.4 GHz, obtained in different configurations (see column (5) of Table 3.1 and black/blue contours in Figure 3.9). This is the only radio source of the sample to have been previously classified as an FR II (Massaro et al. 2013). I manually flagged and calibrated both datasets separately, and then I performed the self-calibration of both observations together. In the final radio map (see Figure 3.10) the core is not clearly detected, and overlaying radio contours to the optical image I did not find a plausible counterpart located between the two lobes. On the other hand there is a WISE source, namely: J201427.59+233452.6, detected in all four filters and corresponding to the intensity peak of the *Chandra* image.

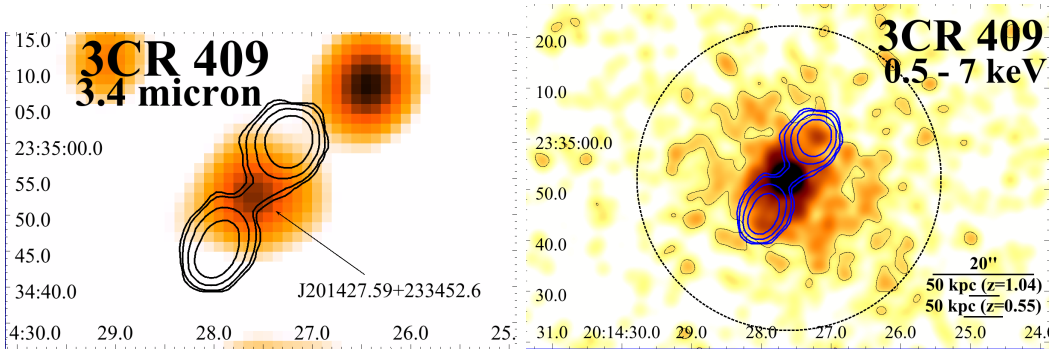

Figure 3.9 *Left Panel*: WISE 3.4 μm filter image of 3CR 409. The arrow points to the IR counterpart of the radio nucleus. No optical counterpart has been detected for this source. VLA black contours at 4.5 GHz are overlaid, starting from 0.02 Jybeam^{-1} increasing by a factor of two, up to 0.64 Jy/beam. *Right Panel*: *Chandra* X-ray image of 3CR 409, filtered in the 0.5-7 keV band, rebinned to 0.123″pixel^{-1} and smoothed with a 4.92″ Gaussian kernel. VLA contours are the same used in the left panel. The dotted black circle has a 0.5′ radius. The black contours trace the X-ray emission at 3×10^{-18} erg cm^{-2} s^{-1}. The X-ray image shows emission associated with the radio lobes as well as more extended emission extending to 60″. In the bottom right of the image, kpcscale measured using the photometric redshifts obtained using the method described in Glowacki et al. (2017) are indicated.

The source *Swift* J201427.5+233455, detected with S/N=11.6, lies in the field of view of 3CR 409 and matches the coordinates of NVSS J201427+233452 with an angular separation of 1.9″. The mid-IR counterpart WISE J201427.59+233452.6 is located at only 0.3″ from the NVSS source. This WISE infrared object is included in the all-sky catalogue of blazar-

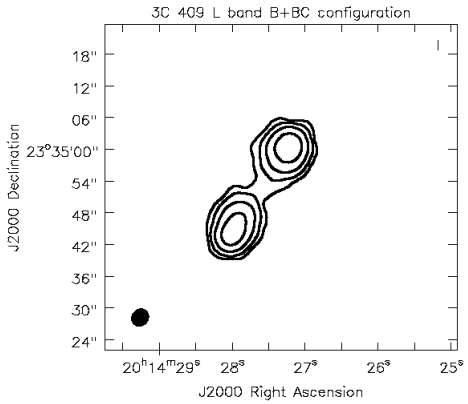

Figure 3.10 Radio VLA contours of 3CR 409. This map has been obtained merging two observations in B and BC configuration, respectively, as described in Section 3.3.2. The name of the source, the observing band, and array configuration are reported on the top of each panel. The clean beam is shown as a black filled ellipse in the bottom left of the image. Radio contours levels are reported in the last column in Table 3.1.

like radio-loud sources by D'Abrusco et al. (2014) and in D'Abrusco et al. (2019). As for previous sources, adopting the procedure described in Glowacki et al. (2017), using the 3.4 μm WISE magnitude I obtained a median redshift of $z = 1.04^{+0.71}_{-0.74}$, and using the 4.6 μm WISE magnitude a median redshift of $z = 0.55^{+0.38}_{-0.46}$ and a probability of 60% of being a QSO.

In the *Chandra* image there is some extended emission around the core, suggesting the presence of a cluster, that I investigated in more details. I have derived the surface brightness profiles in the directions shown in Figure 2.7. Northern and southern directions have been selected to encompass the radio lobes contours, while eastern and western directions are that away from the lobes. From these profiles I have estimated the extension of the diffuse emission, that appears to be symmetrical around the source up to a distance of $\sim 60''$ from the radio core. In the west direction, at a distance of $\sim 10''$ there is a jump in the surface brightness, and the same behaviour can be observed at the same distance in the east direction.

Since I detected more than 400 photons in the nuclear region of the *Chandra* image, I also performed the spectral analysis of the X-ray core, adopting an absorbed power-law model. I obtained the best fit results with $N_{H,int}$ as a free parameter, for both choices of redshift. $N_{H,int}$ has a value of $\sim 10^{23}$ cm^{-2}, and this is probably the reason I did not detect an optical counterpart, under the assumption of a normal gas to dust ratio.

I also analysed the extended X-ray emission, adopting a thermal APEC model with Galactic absorption. As specified in Section 2.2.3, I have excluded a $2''$ circular region where I expect to find most of the nuclear emission and all the detected point sources. However, I also took into account the contribution of *Chandra* PSF wings extending into the region selected for the spectral extraction, that accounts for about ~2% of the 0.5-7 keV net counts. I therefore included such a contribution in the model used to fit the extended emission. I have tested four models: abundance fixed to 0.25 solar and redshift $z = 1.04$ (or $z = 0.55$); redshift $z = 1.04$ (or $z = 0.55$) and free abundance; abundance fixed to 0.25 solar and free redshift, and both abundance and redshift free to vary during the fit. The $z = 0.55$ models yield the best fit statistics, with a poorly constrained temperature $\gtrsim 11$keV. Such temperatures have been reported for clusters at higher redshifts (e.g., $z = 0.89$, Jones et al. 2004), and therefore deeper *Chandra* observations are needed to draw firm conclusions on the nature of this extended X-ray emission.

3CR 428

3CR 428 is a lobe dominated radio source at 4.5 GHz with a clearly detected core (see black/red contours in Figure 3.11, both panels). There is no optical counterpart in the Pan-STARRS R band image of the nucleus while there is a detection at IR frequencies associated with WISE J210822.08+493641.6 located within the XRT positional uncertainty region at an angular separation of $0.5''$. The core is also clearly detected in the *Chandra* image, but there are no clear counterparts of radio lobes or hotspots. The X-ray source XRT J210822.1+493642 also matches the NVSS J210822+493637 position at an angular separation of $5.6''$.

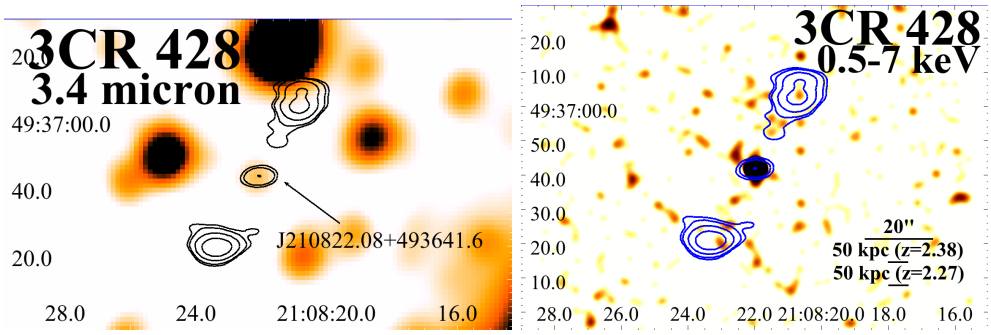

Figure 3.11 *Left Panel*: WISE 3.4 μm filter image of 3CR 428. VLA contours (black) at 4.5 GHz are the same used in the *Chandra* image (red). Radio contours start from 0.002 Jybeam^{-1} and increase by a factor of 2. The arrow points to the IR counterpart of the radio nucleus. No optical counterpart has been detected for this source. *Right Panel*: *Chandra* X-ray image of 3CR 428, filtered in the 0.5-7 keV band. Image has not been rebinned, but smoothed with a 6 pixel Gaussian kernel (equivalent to 2.952″). In the bottom right of the image, kpcscale measured using the photometric redshifts obtained using the method described in Glowacki et al. (2017) are indicated.

As for 3CR 91, 3CR 390, and 3CR 409, the WISE counterpart has been recently included in the all-sky catalogue of blazar candidates of D'Abrusco et al. (2014). Adopting the procedure described in Glowacki et al. (2017), using the 3.4 μm WISE magnitude I obtained a photometric redshift of $z = 2.38^{+1.62}_{-1.66}$, and using the 4.6μm WISE magnitude a photometric redshift of $z = 2.27^{+1.59}_{-1.58}$, with a probability of 70% for the source being a QSO.

Since I detected more than 400 photons in the nuclear region of the *Chandra* image, I also performed a spectral analysis of the X-ray core, adopting an absorbed power-law model. As in the case of 3CR 409 I obtained a value of $N_{H,int} \sim 10^{23}$ cm^{-2}, explaining the non-detection of an optical counterpart.

3CR 454.2

3CR 454.2 is a lobe dominated radio source in the 8 GHz VLA image, in which I clearly detected the core and two lobes and hotspots (see black contours in the left panel of Figure 3.13). In the Pan-STARRS image there is no optical counterpart located at the radio core position.

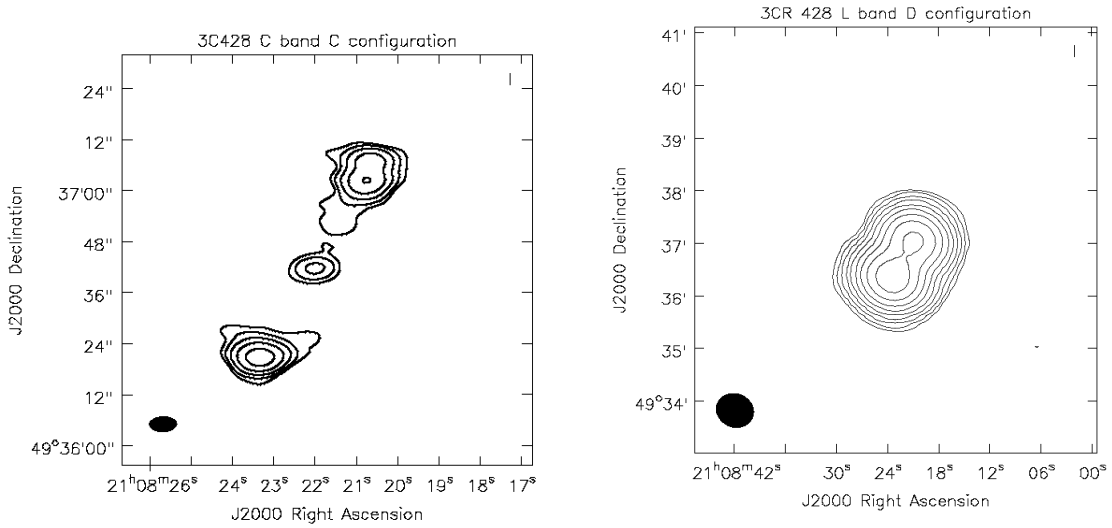

Figure 3.12 Radio VLA contours of 3CR 428. The name of the source, the observing band, and array configuration are reported on the top of each panel. The clean beam is shown as a black filled ellipse in the bottom left of the image. Radio contours levels are reported in the last column in Table 3.1.

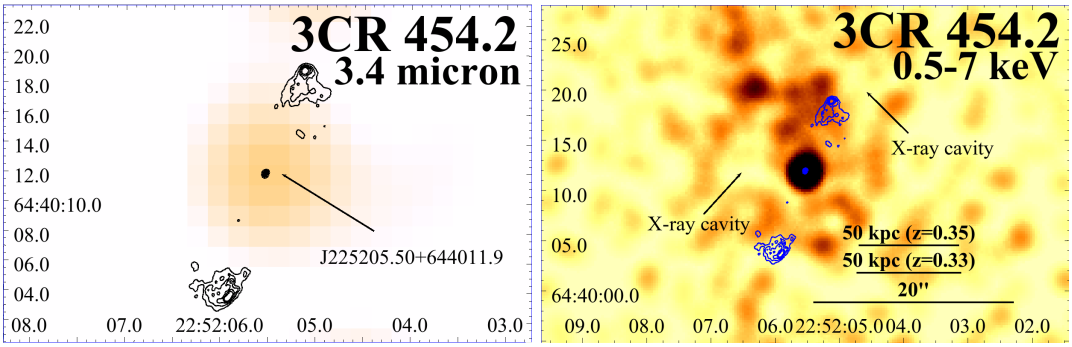

Figure 3.13 *Left Panel*: WISE 3.4 μm filter image of 3CR 454.2. VLA contours (black) are the same used in the *Chandra* image (blue) and start from 0.001 Jy/beam and increasing by a factor of 0.001 Jybeam^{-1} to 0.005 Jybeam^{-1}. The arrow points to the IR counterpart of the radio nucleus. No optical counterpart has been detected for this source. *Right Panel*: *Chandra* X-ray image of 3CR 454.2, filtered in the 0.5-7 keV band, binned up to 0.246″pixel^{-1} and smoothed with a 8 pixels Gaussian kernel (equivalent to 1.968 arcsec). Cavities are indicated by arrows. In the bottom right of the image, kpcscale measured using the photometric redshifts obtained using the method described in Glowacki et al. (2017) are indicated.

In Maselli et al. (2016) a soft X-ray source XRT J225205.2+644013 was detected, at an angular separation of 4.6″ from the coordinates of NVSS J225205+644010 within its 3CR

positional uncertainty region. At an angular separation of 2.3″ from this NVSS source, the IR source WISE J225205.50+644011.9 was also found in the AllWISE Catalogue, being its potential counterpart. It is well detected in all filters but the 22 μm filter. Adopting the procedure described in Glowacki et al. (2017), using the 3.4 μm WISE magnitude, I obtained a photometric redshift value of $z = 0.35^{+0.12}_{-0.11}$, and using the 4.6 μm WISE magnitude a value of $z = 0.33^{+0.12}_{-0.10}$, with a probability of 96% for the source of being a LERG.

In the *Chandra* image, I highlight the presence of extended X-ray emission and the possible presence of at least two cavities (reported in the left panel of Figure 3.13 and, at a larger scale, in Figure 3.14). As in the case of 3CR 409 I have derived the surface brightness profiles in the directions shown in Figure 2.9. Again, northern and southern directions have been selected to encompass the radio lobes contours, while eastern and western directions are that away from the lobes. I found evidence for diffuse emission up to ~ 50″ from the core (see Figure 2.10). The northwestern cavity has less than 2σ level significance, while the southeastern one has a significance of 3.4σ. To evaluate the significance of the cavities, I have estimated the counts in each cavity, using circular regions of appropriate radii, and the average level of the diffuse emission at the same distance from the core using several circular regions with the same radii of the cavity regions. Then, using Poisson statistics, I evaluated the Gaussian σ equivalent of the cavities significance. I have performed a spectral analysis of the diffuse X-ray emission, adopting a thermal model, in every possible combination of redshift and abundance values, fixed or free. As specified in Subsection 2.2.3, I have excluded a 2″ circular region including the nuclear emission, but since the contribution of the wings of the PSF was lower than 1%, I have excluded this contribution in the thermal model of the extended emission. Due to low count statistics, all fits are poorly constrained and the uncertainties on the temperature are large. Also in this case, deeper *Chandra* observations are needed to properly constrain the properties of the cluster ICM.

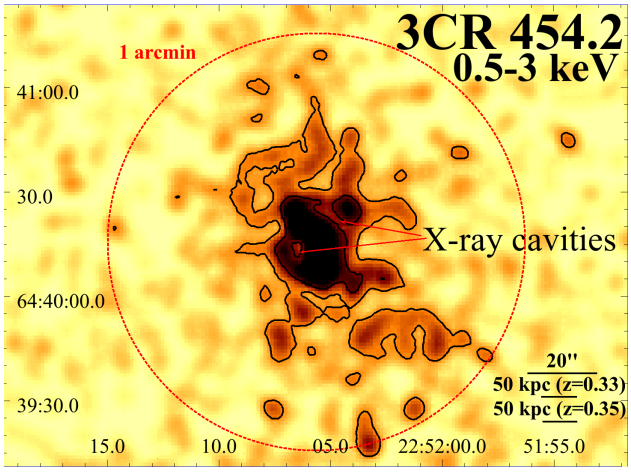

Figure 3.14 *Chandra* X-ray image of 3CR 454.2, filtered in the 0.5-3 keV band, binned up to $0.984''$pixel^{-1} and smoothed with a $4.92''$ Gaussian kernel. The black circle has a $0.5'$radius. The black contours trace the X-ray emission at 0.1 and 0.2 counts pixel^{-1}. In the bottom right of the image, kpcscale measured using the photometric redshifts obtained using the method described in Glowacki et al. (2017) are indicated.

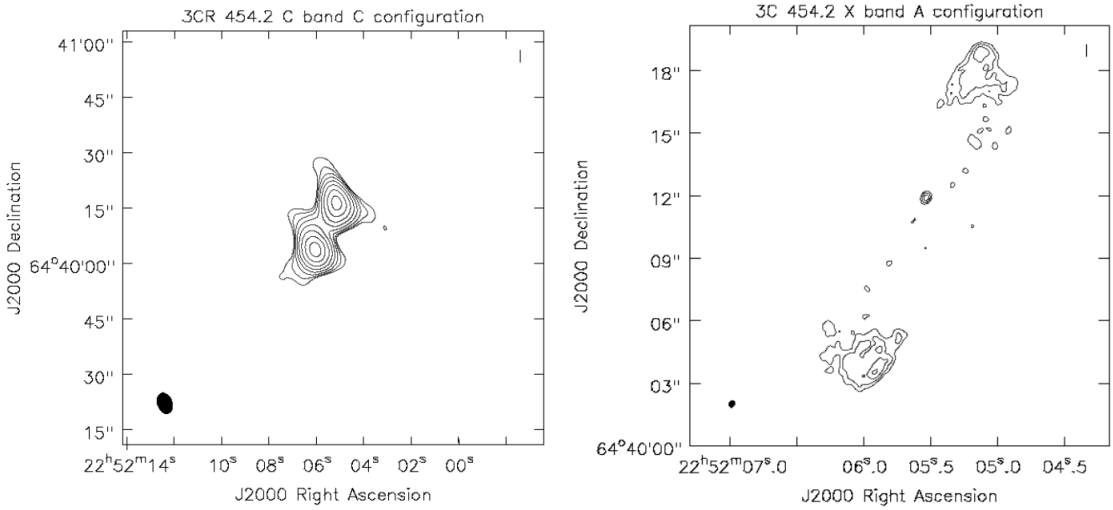

Figure 3.15 Radio VLA contours of 3CR 454.2. The name of the source, the observing band, and array configuration are reported on the top of each panel. The clean beam is shown as a black filled ellipse in the bottom left of the image. Radio contours levels are reported in the last column in Table 3.1.

Table 3.3 Summary of optical and IR observations of 3C unidentified sources.

3CR name	NVSS name	WISE name	E(B-V) (mag)	w1 (mag)	w2 (mag)	w3 (mag)	R band (mag)	z_{w1}	z_{w2}	VLA/*Chandra* (arcsec)
91	J033743+504552	J033743.02+504547.6	1.05±0.05	11.885±0.022	10.80±0.021	7.936±0.020	20.29±0.05	0.23 ± 0.18	$0.19^{+0.18}_{-0.14}$	0.43
131	J045323+312924	J045323.34+312928.4	0.83±0.02	14.98±0.041	14.77±0.082	12.306	-	$0.41^{+0.13}_{-0.12}$	0.44 ± 0.13	0.65
158	J062141+143211	J062141.01+143212.8	0.77±0.02	15.133±0.046	13.953±0.043	11.131±0.189	20.62±0.06	$4.57^{+0.68}_{-3.14}$	$3.16^{+2.09}_{-2.19}$	0.35
390	J184537+09534	J184537.60+095345.0	0.49±0.01	12.546±0.043	11.575±0.024	9.150±0.029	18.80± 0.06	$0.41^{+0.28}_{-0.32}$	$0.30^{+0.21}_{-0.25}$	0.02
409	J201427+233452	J201427.59+233452.6	0.57±0.03	13.547±0.050	12.377±0.027	9.005±0.027	-	$1.04^{+0.71}_{-0.74}$	$0.55^{+0.38}_{-0.46}$	*
428	J210822+493637	J210822.08+493641.6	2.59±0.07	14.559±0.064	13.097±0.035	10.143±0.056	-	$2.38^{+1.62}_{-1.66}$	$2.27^{+1.59}_{-1.58}$	1.09
454.2	J225205+644010	J225205.50+644011.9	1.26±0.04	14.652±0.030	14.341±0.042	13.121±0.467	-	$0.35^{+0.12}_{-0.11}$	$0.33^{+0.12}_{-0.10}$	0.72

Col. (1): The 3CR name. Col. (2): Associated NVSS source. Col. (3): Associated WISE source. Col. (4): Extinction, as reported in the NASA/IPAC Infrared Science Archive (IRSA). Col. (5): Magnitude in the WISE w1 filter (3.4 μm). Col. (6): Magnitude in the WISE w2 filter (4.6 μm). Col. (7): Magnitude in the WISE w3 filter (12 μm). Col. (8): Magnitude in the Pan-STARRS R band. Col. (9): Median redshift value obtained from 3.4 μm filter magnitude. Col. (10): Median redshift value obtained from 4.6 μm filter magnitude. Col. (11): Angular separation between the position of the radio core detected in the VLA maps and that of the associated X-ray counterpart in the *Chandra* images (see Section 2.2.3) . *Since I was unable to detect the position of the radio core of 3CR 409, the swift is missing. ** For the estimate of the photometric redshift I have used dereddened values of the WISE magnitude corrected for Galactic absorption using reddening estimates from Schlafly & Finkbeiner (2011a) and the extinction model from Fitzpatrick & Massa (2007).

Table 3.4 Properties of nuclear X-ray emission of 3C unidentified sources.

3CR name	Net counts	$F^{*}_{0.5-1\ keV}$ (cgs)	$F^{*}_{1-2\ keV}$ (cgs)	$F^{*}_{2-7\ keV}$ (cgs)	$F^{*}_{0.5-7\ keV}$ (cgs)
91	1938.5 (44.0)	2.5 (0.5)	21.5 (0.8)	92.4 (2.7)	116.4 (2.8)
131	62.4 (8.0)	–	0.2 (0.1)	3.8 (0.5)	3.9 (0.5)
158	288.4 (17.0)	0.5 (0.2)	2.8 (0.3)	9.2 (0.7)	12.5 (0.8)
390	1068.5 (32.7)	4.1(0.6)	12.7 (0.6)	40.2 (1.7)	57.0 (1.9)
409	596.5 (24.4)	0.3 (0.2)	3.6 (0.3)	35.3 (1.6)	39.2 (1.7)
428	557.5 (23.6)	0.2 (0.1)	3.9 (0.3)	28.5 (1.4)	32.6 (1.4)
454.2	33.5 (5.8)	–	0.1 (0.1)	2.1 (0.4)	2.2 (0.4)

Col. (1): 3CR name. Col. (2): Background-subtracted number of photons within a circle of radius $r = 2''$ in the 0.5 - 7 keV band. Col. (3): Measured X-ray flux between 0.5 and 1 keV. Col. (4): Measured X-ray flux between 1 and 2 keV. Col. (5): Measured X-ray flux between 2 and 7 keV. Col. (6): Measured X-ray flux between 0.5 and 7 keV. Note:
(*) Fluxes are given in units of 10^{-14}erg cm^{-2} s^{-1} and 1σ uncertainties in the number of photons computed assuming Poisson statistics are given in parenthesis. The uncertainties on the flux measurements are computed as described in Section 2.2.3. Fluxes were not corrected for Galactic absorption and were computed adopting the same X-ray photometric measurements of Massaro et al. (2015).

3.3 3CR 403.1 Imaging with the Sardinia Radio Telescope

Note: Section adapted from Missaglia et al. (2022).

During a follow up analysis of several targets of the 3CR *Chandra* Snapshot Survey, extended X-ray emission around 3CR 403.1, a nearby radio galaxy, was discovered (Massaro et al. 2012; Jimenez-Gallardo et al. 2021b), at larger scales with respect to previous literature analyses.

3CR 403.1 (a.k.a. 4C -01.51) is a classical FR II radio galaxy (Fanaroff & Riley 1974) at $z = 0.055$. As reported in Bolton & Ekers (1966) the optical counterpart is elliptical, and it has a low-ionization galaxy-like optical spectrum (Baldi et al. 2010). Hα and [OIII]λ5007 luminosities are in the range between 10^{39} and 10^{40} erg s^{-1} (Buttiglione et al. 2011), while the radio luminosity at 178 MHz is $\log_{10}(P_{178}) = 32.98$ (Spinrad et al. 1985).

A suite of available archival radio observations of 3CR 403.1 (see Figure 3.16) is available. In particular, this radio source was observed with the VLA as part of the NVSS in 1993, as part of the VLSSr in 2003 and with the MWA as part of GLEAM Survey in 2013. The NVSS Catalog covers the sky north of -40 deg declination (~ 35000 sq. deg.). The images all have 45″ FWHM angular resolution and nearly uniform sensitivity, with rms brightness fluctuations approximately of 0.45 mJy beam^{-1} = 0.14 K (Stokes I). The VLSSr has a resolution of 75″, and an average map rms noise level of σ ~ 0.1 Jy beam^{-1}. VLSSr covers ~ 30000 sq. deg. above an irregular southern boundary. GLEAM is an all-sky survey at 74-231 MHz, with angular resolution of 100″ and sensitivity between 6 and 10 mJybeam^{-1}, covering a sky area of ~ 30000 sq. deg.

In radio archival images, 3CR 403.1 shows two prominent radio lobes, extending in the north-west to south-east direction on a scale of ~ 0.5 Mpc and thus being the second most extended 3C source among the 37 sources at redshift $z < 0.1$. In particular, the large scale structure of 3CR 403.1, including the two lobes, is visible at 1.4 GHz in the NRAO VLA Sky Survey (NVSS, Condon et al. 1998) and at lower frequencies at 74 MHz in the Very Large Array Sky Survey Redux (VLSSr, Lane et al. 2014) observations, as well as in the GaLactic

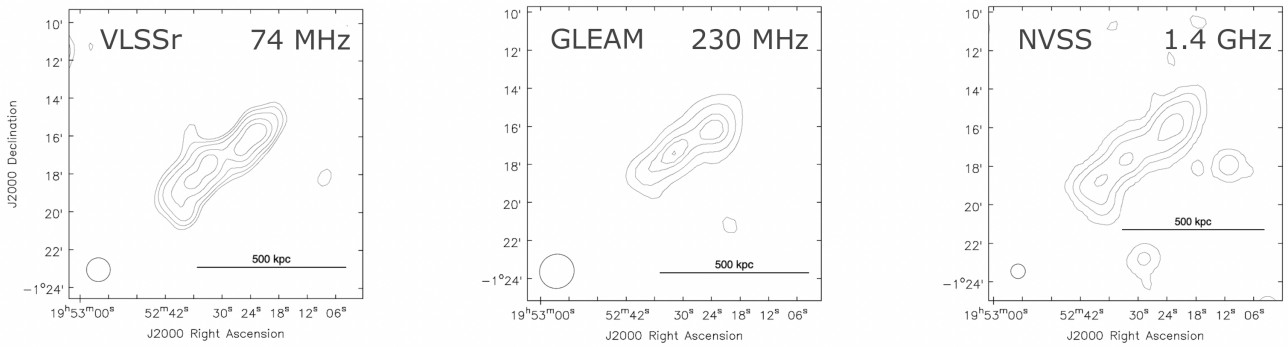

Figure 3.16 Radio maps of 3CR 403.1 as seen at: (*left panel*) 74 MHz (VLSSr), with contours drawn at (5, 7, 10, 15, 20)σ, (*central panel*) 230 MHz (GLEAM) with contours drawn at (3, 5, 7, 8, 9)σ, and (*right panel*) 1.4 GHz (NVSS) with contours drawn at (3, 30, 100, 300)σ. At all frequencies, a radio structure extending 500 kpc is detected, composed of two prominent radio lobes and core.

and Extragalactic All-sky MWA (GLEAM) Survey, which is a continuum survey conducted using the Murchison Widefield Array between 72 and 231 MHz (Wayth et al. 2015). At all radio frequencies, the radio core and lobes are detected above 5σ level of confidence. The radio morphology of 3CR 403.1 is peculiar since at low radio frequencies (i.e., archival VLA P band observation, 230-470 MHz) it shows two radio knots elongated on the west-east direction, separated by 105 kpc, and perpendicular to the radio axis marked by its large scale structure detected at low frequencies, that correspond to small scales cavities in the X-rays (Jimenez-Gallardo et al. 2021b). This emission lies also at the opposite sides of the radio core, detected in the Very Large Array Sky Survey at 2-4 GHz (VLASS, Lacy et al. 2020). In FR II sources, as shown in Massaro et al. (2011), X-ray emission is usually detected along the large scale radio structure. Such emission is typically thought to be due to X-rays produced by relativistic electrons in the lobes that up-scatter ambient cosmic microwave background (CMB) photons via inverse-Compton scattering (IC/CMB) from lobes (see e.g. Harris & Krawczynski 2002). However, diffuse X-ray emission surrounding 3CR 403.1 is detected perpendicular to the large scale radio structure and, thus, it is most likely due to thermal emission from the intracluster medium (ICM) (see e.g. results in Jimenez-Gallardo et al. 2021b). Therefore, given its proximity, 3CR 403.1 is a good candidate to study the

relationship between the ambient ICM and the radio structure at comparatively high spatial resolution.

Here I present follow up observations of 3CR 403.1 with the Sardinia Radio Telescope (SRT; Bolli et al. 2015; Prandoni et al. 2017). These observations were carried out at the end of 2020 to (1) investigate the spectral shape at higher frequency of the radio structure, (2) perform a spatially resolved, spectral analysis at radio frequencies, given the clear detection of the radio components shown in Figure 3.16, and (3) carry out radio polarimetric observations. Polarimetric radio observations, in combination with X-ray observations, permit the study of the properties of the magnetic field permeating the ICM in which radio lobes are embedded.

This work is organized as follows. In Section 3.3.1 I provide details about the available archival radio data and the data reduction procedure adopted for SRT and *Chandra* observations. In Section 3.3.2 I report a brief optical overview of the source and I discuss (1) the radio spectral analysis, (2) the test performed to confirm the presence of a possible Sunyaev-Zel'dovich (SZ) effect, (3) the measurements of the magnetic field by means of the rotation measure (RM).

According to the cosmological parameters of (Bennett et al. 2014), $1''$ corresponds to 1.076 kpc at the 3CR 403.1 redshift (i.e., $z_{\rm src}$ =0.055), while its luminosity distance is 246.9 Mpc.

3.3.1 Radio and X-ray Observations

New SRT data were collected to deeply investigate the radio components of 3CR 403.1 (see Figure 3.17).

3CR 403.1 was pointed with the SRT K-band seven feed receiver between November, 19th and December, 19th 2020 (project ID 30-20; see Table 3.5 for details). A field-of-view of about $15' \times 15'$ centered on R.A.$_{\rm J2000}$=19h52m30s and Dec.$_{\rm J2000}$=-01d17m35s was imaged. Multiple on-the-fly scans in the equatorial frame were acquired, moving at a speed of $1'$/sec along the orthogonal R.A. and Dec. directions. The scanning speed was set as a

Table 3.5 Details of the SRT observations of 3CR 403.1.

Frequency (GHz)	Resolution (arcsec)	TOS (hrs)	Observing date	OTF Mapping	calibrators	SRT Project
18–19.2	57	7	19-Nov-2020	10 R.A.×10 Dec.	3C 286, 3C 84, 3C 147	30-20
		6	20-Nov-2020	9 R.A.×9 Dec.	3C 286, 3C 84, 3C 147	30-20
		7	19-Dec-2020	10 R.A.×9 Dec.	3C 286, 3C 84, 3C 147	30-20

Col. 1: SRT frequency range; Col. 2: SRT resolution; Col. 3: Time on source; Col. 4: Date of observation; Col. 5: Number of images on the source; Col. 6: Calibrators; Col. 7: SRT project name.

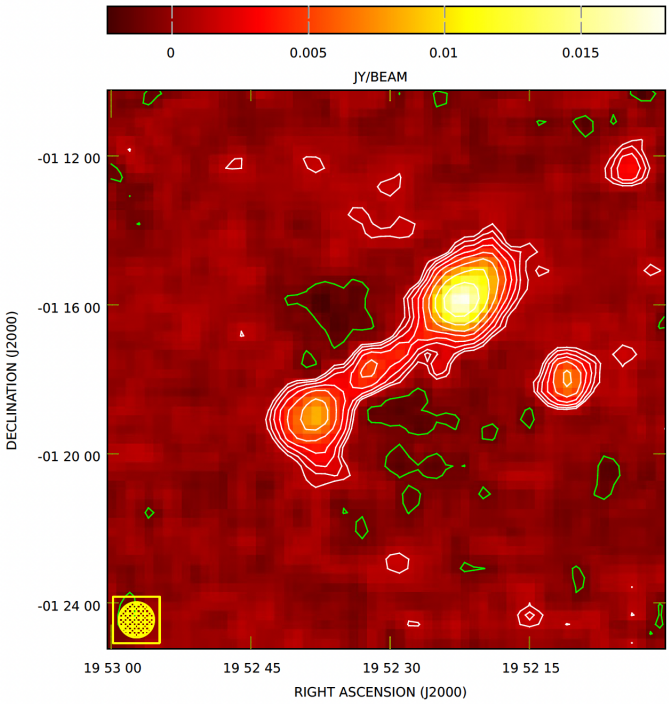

Figure 3.17 3CR 403.1 total intensity image at 18.6 GHz. Contours start at 1.2 mJy/beam (3σ) and increase by $\sqrt{2}$. The negative green contour is traced at -1.2 mJy/beam.

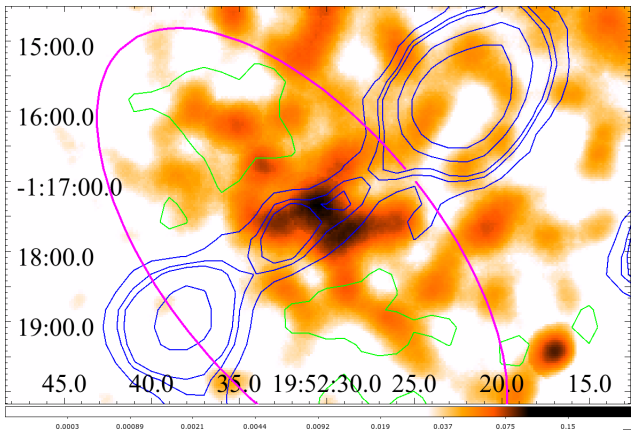

Figure 3.18 *Chandra* X-ray image of 3CR 403.1, filtered in the 0.5–3 keV band, binned up to 1.968″ pixel^{-1} and smoothed with a 25.6″ Gaussian kernel. Radio contours (SRT, 18.6 GHz) are drawn at (3, 5, 6, 10, 15, 30, 50)σ. The negative green contour is traced at -1.2 mJy/beam (see Figure 3.17). The magenta ellipse indicates the region used to extract the X-ray spectrum. This region is cospatial with the flux decrement observed in the SRT image. See Section 2.2.3 for more details.

compromise between mapping efficiency and the need to reduce the 1/f noise produced by the atmospheric and receiver gain fluctuations.

The source has been observed in full-Stokes spectral–polarimetric mode in the frequency range from 18.0 to 19.2 GHz with a central frequency of 18.6 GHz, using the SARDARA back-end (Melis et al. 2018). Data were acquired at a rate of about 33 spectra s^{-1} at a spectral resolution of 1.46 MHz. The full width at high maximum (FWHM) of the SRT beam at this frequency is 57″, and I used a pixel size of 15″ in the imaging to match the transverse separation between the sub-scans. In this way, the separation of the sub-scans is equivalent to one pixel and the beam FWHM is sampled with about four independent pixels. For each pixel, I collected eight different spectra, that I averaged to increase the signal-to-noise ratio. All the details of the imaging and analysis of the SRT data are described in Section 2.2.1.

3CR 403.1 was also observed for ~ 8 ks with *Chandra* X-ray Observatory in 2010 (see Figure 3.18), as part of the 3CR *Chandra* Snapshot Survey (Massaro et al. 2010) in Observation Cycle 22 (Proposal number 12700211). In the first analysis, presented in Massaro et al. (2012), only a marginal X-ray detection of a relatively weak radio core was

reported. In Jimenez-Gallardo et al. (2021b) the same *Chandra* observation was re-analysed and X-ray extended emission on tens of kpc scale, aligned with radio emission detected only at ~ 250 MHz, was claimed at 5σ level of significance.

I reanalyzed the *Chandra* dataset and used it to carry out an X-ray spectral analysis (see Sec. 2.2.3 for the details of the data reduction).

3.3.2 3CR 403.1: Optical and Radio Analysis

MUSE Overview

3CR 403.1 was recently observed as part of the MUSE RAdio Loud Emission line Snapshot survey (MURALES, Balmaverde et al. 2019, 2021), thus optical spectroscopic observations of surrounding galaxies are reported here aiming at confirming the presence of a galaxy group around 3CR 403.1.

As reported in Balmaverde et al. (2019), the line morphology in this source is particularly complex, and the observations reveal the presence of a central region (~ 9 kpc in size), with well ordered rotation and elongated structures with knots (eastern and south-eastern directions), extending up to ~ 35 kpc from the galaxy nucleus, with similar velocities and redshifted by ~ 150-200 km s^{-1}. These structures are due to ionized gas, visible as line emitting gas (mainly Hα). The spatial distribution of the ionized gas has a "ring-like" shape, as the other companion galaxies in the group. There are several galaxies in the MUSE field of view, but only a few emission line knots are associated with them.

Thanks to the MUSE observations it was possible to identify and estimate the redshift for several companion galaxies around 3CR 403.1. To obtain the redshift, each line was fitted with a Gaussian, using QFitsView[1], which also takes into account the continuum. Spectra were extracted in each case from a circular region of 5 pixels radius, i.e., 1″ to match the seeing of the MUSE observation, using QFitsView. I discovered five nearby companions all marked in Figure 3.19 together with their redshifts. I measured the velocity dispersion of the five nearby companions, obtaining a value of the sample estimate of the

[1] https://www.mpe.mpg.de/~ott/dpuser/qfitsview.html

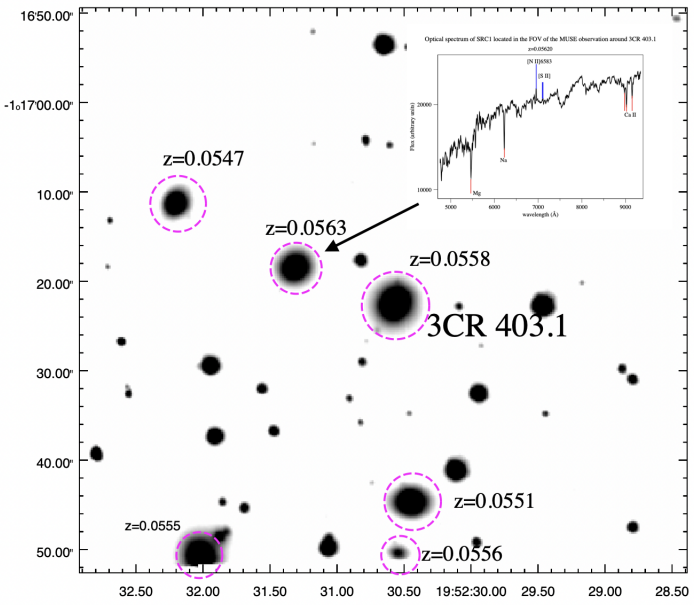

Figure 3.19 MUSE white-light observation of the 3CR 403.1 field (1′ square or 4168 kpc^2). Sources in the same group as our target are indicated with magenta circles. For the other sources in the field, an estimate of z was not possible due to a low signal-to-noise ratio. For one of the sources in the group, the spectrum used to estimate the redshift is added.

radial velocity dispersion to be σ_v = 143 km s^{-1}. According to the analysis carried out in Massaro et al. (2020), assuming that this group is virialized and that galaxies have random uncorrelated velocity vectors, I estimate the total mass of the large scale environment, including dark matter, galaxies and ICM within a radius of 158 kpc (that is, the equivalent radius of the elliptical region chosen for the X-ray spectral analysis, see Section 3.3.2) as $M_{env} = 7.5 \times 10^{11} M_{\odot}$. Since this estimate of M_{env} is achieved with a low number of sources, I did not compute the statistical uncertainty. Given the mass of the environment, the size (~ 2-3 kpc) and optical luminosities (~ $10^9 L_{\odot}$, obtained from Pan-STARRS r-filter magnitudes, see Staveley-Smith et al. 1992 for comparison) of the sources, this is in agreement with 3CR 403.1 belonging to a small group of dwarf galaxies (for typical masses of a small group of dwarf galaxies see e.g. Makarov & Uklein 2012). The mass estimate was computed using only six sources, with a signal to noise ratio such that it was possible to firmly measure their redshifts (see Figure 3.19 for an example of the used spectra).

I estimated the equipartition field, B_{eq}, following the same procedure discussed in Murgia et al. (2012), and I obtained a value of B_{eq} = 2.4 μG, that led to a spectral age of the source of ~ 93 Myr, evaluated according to the equation:

$$t_{\rm syn} = 1590 \frac{B^{0.5}}{(B^2 + B^2_{\rm CMB})[(1+z)\nu_{\rm b}]^{0.5}} \ {\rm Myr}, \tag{3.1}$$

where B and $B_{\rm CMB} = 3.25(1+z)^2 \mu$G are the source magnetic field and magnetic field with the same energy density of the CMB, respectively, and assuming an isotropic distribution of electron pitch angles (see e.g. Murgia et al. 2011; Massaro & Ajello 2011a).

SRT Analysis

I first measured the flux density of 3CR 403.1 in four radio bands (VLSSr at 74 MHz, GLEAM at 230 MHz, NVSS at 1.4 GHz and SRT at 18.6 GHz) for the entire source, and I compared these values with other global measurements taken from the literature. The global radio spectrum is determined by the sum of the spectra of both (a) the freshly accelerated electrons, whose spectrum is assumed to be a power-law, and (b) the spectra of the older electron populations, whose spectrum cuts-off at high-frequency because of the radiative losses. For this reason, I make the hypothesis that the radio source is currently in the active phase, during which the radio lobes are continuously replenished with new particles by the AGN. I then analysed the spatially resolved spectra at an intermediate resolution for three components: the northern lobe, the southern lobe, and the inner region in between, correspondent to the radio core. All components are defined using a 3σ limit. The flux density of the entire source was measured convolving with the VLSSr beam ($75''$), and using the 3σ level contour from the NVSS image. For the radio components, I convolved all the images with the GLEAM beam (~ $111''$) and then used the new 3σ level limit of the images to define the components. I then investigated the spectral index image of the source between 1.4 and 18.6 GHz at a slightly finer angular resolution of about $57''$. Measurements are summarized in Table 3.6.

Table 3.6 Flux densities of 3CR 403.1 and of its morphological features. Fluxes of core and lobes regions have been measured using GLEAM convolved beam.

Frequency (GHz)	Flux density core region (mJy)	Flux density southern lobe (mJy)	Flux density northern lobe (mJy)	Flux density entire (mJy)
0.074	4210±580	5560±690	4500±610	14800±200
0.230	2000±230	2000±230	2820±300	3490±100
1.4	394±40	455±50	672e±70	1500±1
18.6	2.51±1.39	16.9±2.2	47±5	67.4±0.5

Col. 1: Frequency; Col. 2: Flux density of the core region; Col. 3: Flux density of the southern lobe; Col. 4: Flux density of the northern lobe; Col. 5: Flux density of the entire source.

In Figure 3.20, comparison of SRT total integrated flux measurements are compared with literature data taken from the NASA/IPAC Extragalactic Database[2] and Astrophysical CATalogs support System[3] finding a good agreement.

The integrated spectrum was fitted with a continuous injection model (C.I.; Pacholczyk 1970) making use of the SYNAGE software (Murgia et al. 1999). This model is characterized by three free parameters: the injection spectral index (α_{inj}), the break frequency (ν_b), and the flux normalization. In the context of the C.I. model, it is assumed that the spectral break is due to the energy losses of the oldest relativistic electrons in the source. For high-energy electrons, energy losses are primarily due to the synchrotron radiation itself and to inverse Compton scattering on CMB photons. The spectral break marks the transition to high-frequency power-law characterized by a steeper index $\alpha = \alpha_{inj} + 0.5$. During the active phase, the evolution of the integrated spectrum is determined by the shift with time of ν_b to lower and lower frequencies. Indeed, the spectral break can be considered to be a clock indicating the time elapsed since the injection of the first electron population. The best fit of the C.I. model yields ν_b=1.9 ± 0.7 GHz.

The spectra of the three components are plotted in Figure 3.20 along with the fit of the JP model (Jaffe & Perola 1974). The JP model describes the radiative ageing of a single population of electrons with an initial power-law distribution, assuming that energy losses

[2] https://ned.ipac.caltech.edu
[3] http://www.sao.ru/cats/

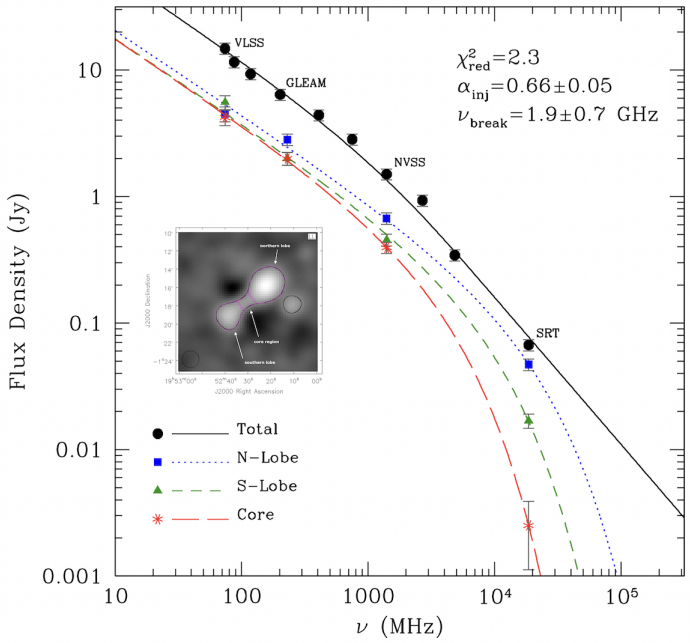

Figure 3.20 Total radio spectrum of 3CR 403.1. Black circles represent the flux densities measured in this work, complemented with values taken from the literature. The continuous black line is the best-fit of the CI model and shows the presence of a spectral break at a frequency of 1.9 GHz, followed by a moderate steepening. Blue squares, green triangles, and red stars represent the spectra of the north lobe, the south lobe, and the core regions respectively (highlighted in the image added on the plot). These components were modelled using a Jaffe-Perola whose best-fit is represented by the blue dotted, green short-dashed, and red long-dashed lines.

due to the inverse Compton scattering of seed photons arising from the CMB are as relevant as radiative losses due to synchrotron emission. In these conditions, the initial power-law with index α_{inj} develops a high-frequency exponential cut-off beyond a break frequency ν_b. The radiative age and the break frequency are related again by Equation 3.1.

The spatially resolved spectral analysis, shown in Figure 3.20, indicates that the spectrum of the inner parts of the radio lobes (those close to the radio source's core) is steeper than that of the outer lobes. Using basic physics, it is possible to conclude that this is due to the presence of a spectral break that shifts to lower frequencies. Indeed, in 3CR 403.1 I found that the oldest electrons are close to the core, while the electrons are younger at the tip of the lobes. This is the typical scenario found in type-2 sources (see Parma et al. 1999), where radio jets have deposited old electrons back as they make their way through the ambient gas.

Finally, I investigated the spectral properties of 3CR 403.1 at a slightly higher angular resolution by analysing the spectral index map of the source between 1.4 (NVSS) and 18.6 GHz (SRT) (see Figure 3.21) according to the following steps: (1) I smoothed the NVSS image to the same resolution as that of the SRT ($57''$), (2) I aligned the two images using as a reference the point-like source south-west of the northern lobe and (3) I regridded the images with the new coordinates. In the spectral index map, only pixels with surface brightness above 3σ, both in the NVSS and in the SRT images, were used. Uncertainties are computed using standard uncertainty propagation formulas. It is observed a steepening of the spectral index from the lobe outer edge inward to the core region, indeed confirming the characteristic trend typical of spectral type-2 sources.

Investigating the Possible Presence of 'SZ' Signatures

In the SRT total intensity image I noticed two regions, lying on opposite sides of the large scale radio structure, along the west-east direction, where I measured a negative intensity at 18.6 GHz with respect to the image background, as already highlighted in Figure 3.17.

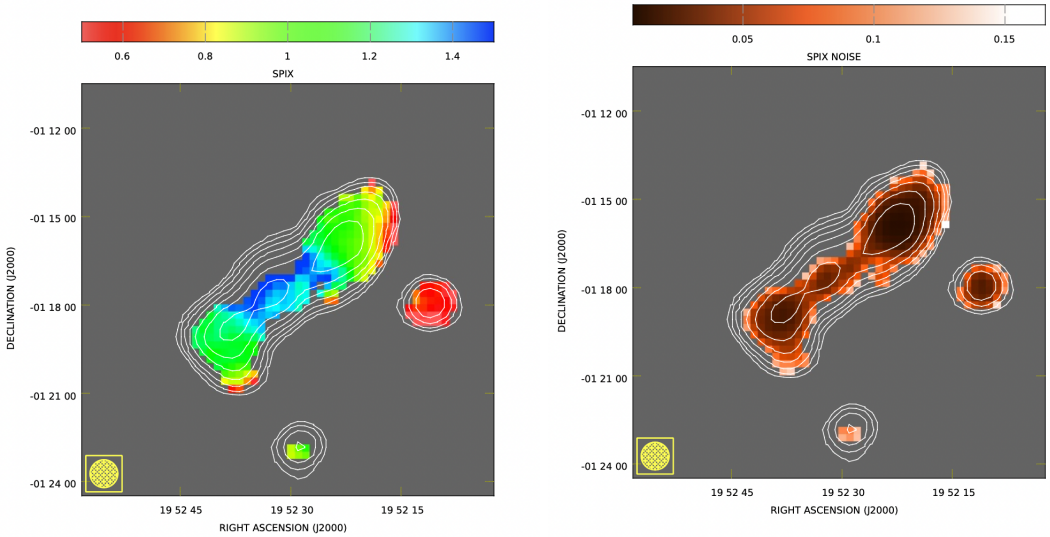

Figure 3.21 *Left Panel*: Spectral index map of 3CR 403.1 between 1.4 GHz (NVSS) and 18.6 GHz (SRT) at a resolution of 57″, as shown in the bottom left corner. The noise levels in the NVSS and SRT images are of 0.73 mJy/beam and 0.37 mJy/beam, respectively. The spectral index is calculated only in those pixels where the signal is above 3σ at both frequencies. White contours show the NVSS emission at 1.4 GHz and are drawn at 3σ increasing by a factor of 2. The average statistical uncertainty on the spectral index *(right panel)* is 0.05.

I estimate that the radio intensity decrement at 18.6 GHz is significant at more than a 3σ level with respect to the fluctuations of the background in the SRT image (rms= 4.66×10^{-4} Jy beam^{-1}).

The negative signal in the SRT image is spatially associated with the extended X-ray emission revealed in the *Chandra* image (see the magenta ellipse in Figure 3.18). The X-ray emission is interpreted as thermal radiation from the gas of the ICM because it is not spatially associated with either GHz or MHz radio counterparts. In order to carry out a deeper investigation into the origin of the negative radio signal, I compared its properties with the values I measured for the X-ray spectral parameters for the surrounding medium of 3CR 403.1.

Assuming that a fraction of the radio background of the SRT observations is due to CMB, when looking in the direction of the galaxy cluster I expect a decrease of the radio intensity due to inverse Compton emission by relatively hot electrons of the ICM that upscatter the CMB radiation (Sunyaev & Zeldovich 1972). Since all flux measurements are reported with respect to the background level, constituted by the CMB radiation and corresponding to the "zero level", I can consider the SZ effect a "true" negative signal in the radio images (Birkinshaw 1999). Thus I estimated the Comptonization parameter y from both radio and X-ray observations, respectively, and compared them.

At radio frequencies I computed the y_R parameter starting from the change in temperature of the CMB due to the SZ effect:

$$\frac{\Delta T}{T_{\rm CMB}} = f(x) y_R \tag{3.2}$$

with f(x) being the frequency spectrum of the temperature variation and y_R the Comptonization parameter.

In the Rayleigh-Jeans approximation for the black body spectrum of the CMB at 18.6 GHz I have $f(x) = -2$ and then equation 3.2 becomes:

$$\frac{\Delta T_{\rm RJ}}{T_{\rm CMB}} = -2y_R \tag{3.3}$$

At radio frequencies, I use a simplified expression for the flux intensity in a given instrument beam as reported in Basu et al. 2016:

$$\left(\frac{I_\nu}{\rm mJy/beam}\right) = \frac{1}{340}\left(\frac{\Delta T_{\rm RJ}}{\rm mK}\right)\left(\frac{\nu}{\rm GHz}\right)^2\left(\frac{\Omega_{\rm beam}}{\rm arcmin^2}\right) \tag{3.4}$$

Replacing equation 3.3 in 3.4 I obtain:

$$y_R = -170\left(\frac{I_\nu}{\rm mJy/beam}\right)\left(\frac{\rm GHz}{\nu}\right)^2\left(\frac{\rm mK}{T_{\rm CMB}}\right)\left(\frac{\rm arcmin^2}{1.13\ \theta^2_{\rm FWHM}}\right) \tag{3.5}$$

where the solid angle $\Omega_{\rm beam}$ can be approximated as $\Omega_{\rm beam} = 1.13\ \theta^2_{\rm FWHM}$ where $\theta_{\rm FWHM}$ is the half-power beam width.

I measured the decrease of the flux intensity in an elliptical region with semiaxes ~ 125x254 kpc (see magenta ellipse in Figure 3.18) with an area equal to 0.1 Mpc^2, corresponding to 15.1 SRT beams, encompassing the nucleus of 3CR 403.1 (masking the nucleus and the jets), where I detected the highest value of the negative signal. I obtained a flux intensity equal to I_ν=-0.9 ± 0.1 mJy beam^{-1} that corresponds to an integrated flux S_ν=-21±2 mJy (in 22.3 SRT beams, assuming that the masked 7.2 beams have the same intensity). From our SRT observations I have $\theta_{\rm FWHM} = 0.95'$, and assuming $T_{\rm CMB}$=2726 mK this leads to an estimate of $y_R = (2.0 \pm 0.2) \times 10^{-4}$ corresponding to a value of (2.0±0.4)×10^{-5} Mpc^2 when measured per unit of area.

In the X-rays the Comptonization parameter, y_X, is indeed related to the line-of-sight integral of the ICM pressure distribution, according to the following equation:

$$y_X = \frac{\sigma_T}{m_e c^2}\int_{L.O.S.} P_e(r) dl \tag{3.6}$$

where $P_e(r) \sim n_e kT$ is the pressure profile of the thermal electrons in the ICM while n_e and T are the gas density and temperature, respectively.

I analyzed the X-ray spectrum extracted from an ellipsoidal region cospatial with the flux decrement in the background CMB radiation (see Figure 3.18), adopting a thermal APEC model with Galactic absorption. I have excluded a 2″ circular region centered on the location of the radio core where I expect to find most of the nuclear emission. Adopting for the thermal component a heavy element abundance equivalent to 0.25 of Solar, a redshift $z = 0.055$ and Galactic absorption equal to 0.117×10^{22} cm^{-2} as reported in HI4PI Collaboration et al. (2016) I obtained a value of the temperature $kT = 0.85^{+0.07}_{-0.08}$ keV and a gas density $n_e = (4.6 \pm 0.3) \times 10^{-4}$cm^{-3}. The mass of the gas in this ellipsoidal volume estimated as reported in Messias et al. (2021) is equal to $M_{gas} \simeq (2.2 \pm 0.1) \times 10^{11} M_{\odot}$.

I estimated y_X using the values of temperature and density obtained from the spectral fit in the ellipse. With $P_e \sim n_e kT$ I obtained $P_e = 6.11^{+0.63}_{-0.69} \times 10^{-13}$ erg cm^{-3}. Assuming a constant value for P_e, from Equation 3.6 I obtained $y_X = 3.82^{+0.40}_{-0.43} \times 10^{-7}$, corresponding to a value of $3.82^{+0.40}_{-0.43} \times 10^{-8}$ Mpc^2 when measured per unit area.

The two values I obtained from the X-ray and radio analysis, are not in agreement, with a discrepancy of three orders of magnitude.

The thermal energy of a gas can be computed starting from the ideal gas law as: $E_{th}=\frac{3}{2}nKTV$ where in this case n and T are respectively the density and temperature obtained from the X-ray spectral analysis in the ellipsoidal volume $V=4.9\times10^{71}$ cm^3. This expression results in $E_{th}=4.46^{+0.46}_{-0.50} \times 10^{59}$ erg. It is possible to calculate the thermal energy also making use of the Comptonization parameter as described in equation 3.6 using for y the value obtained in the radio ($y_R=(2.0\pm0.2)\times10^{-4}$). This results in $E_{th}=\frac{3}{4} y_R \frac{m_e c^2}{\sigma_T} \frac{V}{R}$ where V is again the volume of the ellipse and $R=3.9\times10^{23}$ cm is the semiaxe of the ellipse used to compute the y_R parameter. In this case I obtain $E_{th}=(2.34\pm0.23) \times 10^{62}$ erg. I observe the same discrepancy obtained for the radio-X-ray Comptonization parameters.

I indeed considered the possibility that the negative bowl in the radio image is an artifact left from the data reduction process. Numerous tests were run to determine if the

radio diminution could be considered an artifact or not, such as comparison of the first and last SRT observations, baseline subtraction, more tailored masking, but the results are not conclusive (see details in Appendix 3.3.3).

If I assume that the negative signal is not affected by artifacts, I can then make the hypothesis that the discrepancy of the radio and X-ray values of the Comptonization parameter could be partially due to the presence in the ICM around 3CR 403.1 of a pool of non thermal, mildly relativistic "ghost" electrons, produced during a past activity of the radio source. I assume that the electrons should be mildly relativistic otherwise a thermal bath of electrons would have a same total thermal energy of a relatively massive group or cluster, making this unreliable. These electrons have energy to radiate at such low radio frequencies that cannot be detected but they could still scatter the CMB photons causing the observed negative signal around 3CR 403.1 at 18.6 GHz. Another hint to the AGN past activity is also the presence of the radio knots seen in the seen in an archival VLA P-band observation (not shown), in the same direction of the negative radio signal.

To summarize, there are many possibilities for this decrement (real and artifacts): 1) SZ effect from ICM; 2) imaging artifacts; 3) a pool of non thermal, mildly relativistic "ghost" electrons emitted during a past activity of the radio source, that then cooled and can partially explain the discrepancy of the X-ray and radio Comptonization parameter values (see Appendix 3.3.3 for more details). I also highlight that this is the first time a similar effect has been detected in a radio galaxy at such low redshift, thus deeper observations are needed to investigate this effect in more detail.

ICM Magnetic Field Measurements

I used SRT data combined with NVSS to derive the rotation measure (RM) image of 3CR 403.1 (see Figure 3.23). The RM provides information on the intracluster magnetic fields, since a magnetized plasma changes the properties of the polarized emission coming from a radio source embedded in (or in the background of) the galaxy group/cluster. The position angle of the linearly polarized radiation rotates by an amount that is proportional

to the integral of the magnetic field along the line-of-sight, times the electron density of the ICM (Faraday rotation effect, Dennison 1979).

In the case of an external Faraday screen, i.e. if the magnetoionic medium is located between the radio source and the observer, the polarization angle rotates according to the λ^2-law:

$$\psi_{obs}(\lambda) = \psi_{Int} + \lambda^2 RM \tag{3.7}$$

where ψ_{obs} is the observed polarization at wavelength λ while ψ_{Int} is the intrinsic polarization angle (see e.g. Govoni & Feretti 2004).

By measuring the angle at different frequencies it is possible to derive the RM by a linear fit to Equation 3.7. In this case I simply measured the difference $\Delta\psi$ in the polarization angle between the SRT and the NVSS images (see Figure 3.22) and I computed the RM as:

$$RM = \Delta\psi/(\lambda_1^2 - \lambda_2^2) \qquad \text{rad m}^{-2} \tag{3.8}$$

where λ_1= 0.016 m and λ_2=0.21 m are the wavelengths corresponding the SRT and NVSS images.

The RM image is shown in Figure 3.23 and has been derived considering only those pixels where the uncertainty in the polarization angle is less that 10° and the total intensity is above the 3σ level at both frequencies. The SRT data provide a polarization angle very close to ψ_{Int}, since the rotation is negligible at such a high frequency for typical cluster RMs. However, since I have only two measurements it is not possible to resolve possible $n\pi$-ambiguities on the observed polarization angle in the NVSS image. I observe a net asymmetry in the RM of the two lobes. As shown in Figure 3.23, the southern lobe has an average $RM \simeq -26$ rad m^{-2} while for the northern lobe I observe an average Faraday rotation as low as $RM \simeq 1$ rad m^{-2}.

I modeled the observed RM asymmetry assuming that 3CR 403.1 is located at the center of the galaxy group and is inclined with respect to the plane of the sky so that the southern

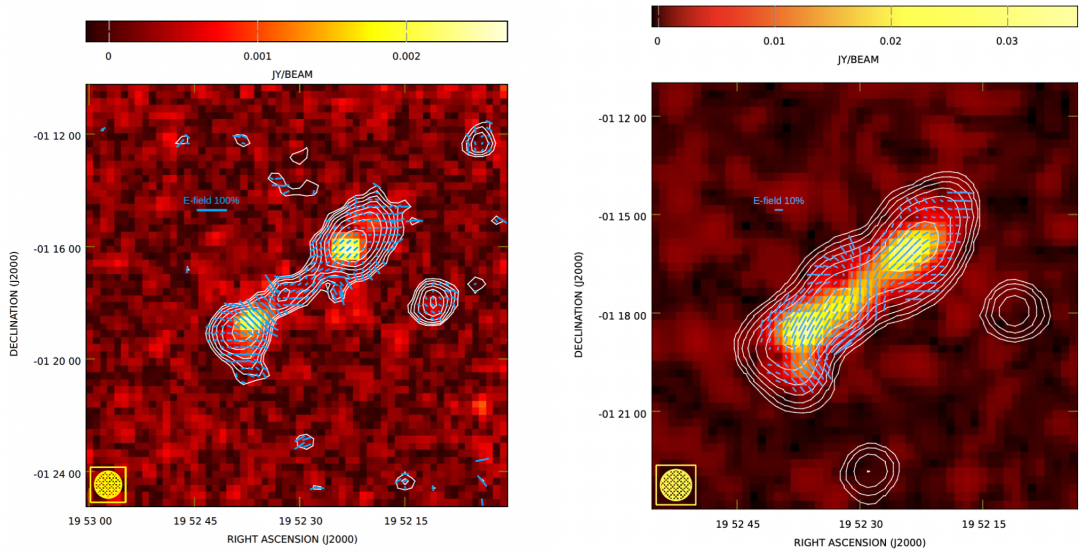

Figure 3.22 *Left Panel*: 3CR 403.1 polarization image at 18.6 GHz (SRT). The contours refer to the total intensity. The polarization vectors represent the direction of the radio wave E-field, with their length proportional to the fractional polarization, while their orientation represents the polarization angle. The average fractional polarization of 3CR 403.1 at 18.6 GHz and $57''$ resolution is FPOL=0.17. *Right Panel*: Polarized intensity image of 3CR 403.1 at 1.4 GHz (NVSS). The contours refer to the total intensity. The polarization vectors represent the direction of the radio wave E-field. Their length is proportional to the fractional polarization while their orientation represents the polarization angle.

lobe has a larger Faraday depth in comparison to the northern lobe (see e.g. Laing et al. 2008).

I considered an idealized situation in which the magnetic field is composed by uniform "cells" of size Λ_B with random direction in space and I used the software FARADAY (Murgia et al. 2004) to calculate the variance of the Faraday rotation ($\sigma^2_{\rm RM}$) from a depth L and a projected radius $r_\perp$:

$$\sigma^2_{\rm RM}(L) = 812^2 \Lambda_B \int_L^{+\infty} (nB_\parallel)^2 dl \quad ({\rm rad^2 m^{-4}}) \tag{3.9}$$

where the cluster's midplane is located at $L = 0$, the cluster far side is located at $L < 0$, and the cluster near side is at $L > 0$ (e.g. Lawler & Dennison 1982; Tribble 1991; Feretti et al. 1995; Felten 1996). In Equation 3.9, the magnetic field strength is in μG, the density in ${\rm cm^{-3}}$, while the field scale and the physical depth are in kpc.

If the electron gas density is described by the β-model (Cavaliere & Fusco-Femiano 1976):

$$n = n_0 \left(1 + \frac{r^2}{r_c^2}\right)^{-\frac{3}{2}\beta}, \tag{3.10}$$

with r_c being the core radius of the gas distribution and I assume that the magnetic field strength scales with the gas density according to:

$$B = B_0 (n/n_0)^\eta \tag{3.11}$$

then, by substituting in Equation 3.9, I find

$$\begin{aligned} \sigma^2_{\rm RM}(L, r_\perp) &= 812^2 \Lambda_c n_0^2 B_0^2 / 3 \times \\ &\times \int_L^{+\infty} (1 + r_\perp^2/r_c^2 + l^2/r_c^2)^{-3\beta(1+\eta)} dl \quad {\rm rad^2 m^{-4}} \end{aligned} \tag{3.12}$$

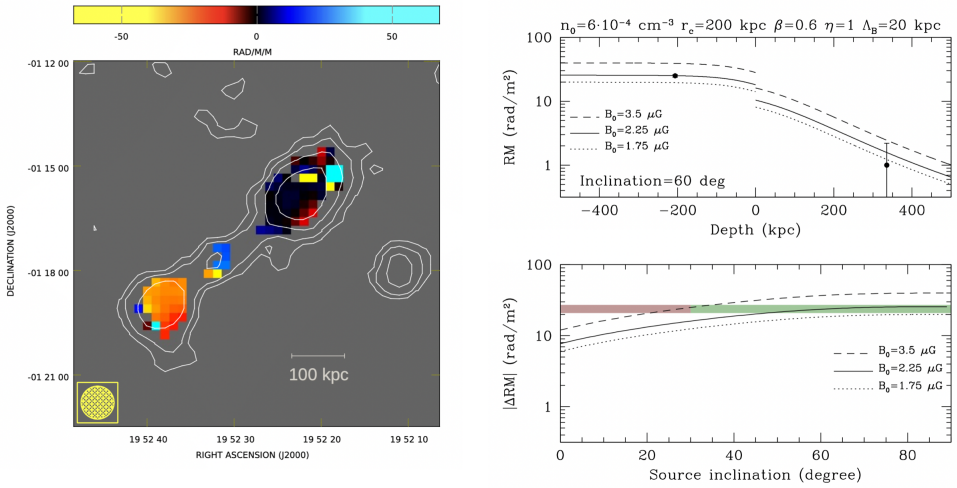

Figure 3.23 *Left Panel*: Rotation measure image calculated with the images at 1.4 and 18.6 GHz smoothed with a FWHM Gaussian of 57″. The color range is from -60 to 60 rad/m^2. Contours refer to the total intensity image at 18 GHz. Levels start at 3σ and increase by a factor of 2.*Right panel, top*: absolute value of the RM as a function of the physical depth of the radio lobes in the cluster medium. The dots represent the measured value for the south (left) and north (right) lobes, plotted at a depth corresponding to a source inclination of 60°. The three lines represent the expected RM signal for three different values of magnetic field strength at the cluster centre. *Right Panel, bottom*: absolute value of the RM difference between the two lobes versus the source inclination. The shaded region represents the measured value, while the lines are the expected RM difference for three different values of magnetic field strength at the cluster centre.

where $r_\perp$ is the impact parameter from the cluster centre, and I assume that the magnetic field is isotropic so that $B_\parallel = B/\sqrt{3}$.

For the β-model I assumed a core radius r_c = 200 kpc and β = 0.6, while for the magnetic field model I assumed a correlation length of Λ_B = 20 kpc and η = 1. These are the best fit parameter found for A 194 by Govoni et al. (2017). The central gas density in A 194 is similar to that of 3CR 403.1, and I speculate that the properties of the intracluster magnetic field derived for A 194 using high-resolution RM data can be assumed as a reference also for the case of 3CR 403.1. Indeed, I fixed Λ_B and η, and I deduce the combinations of the central magnetic field strength, B_0, and the source inclination with respect to the plane of the sky that explain the observed RM asymmetry between the two lobes.

In the upper right panel of Figure 3.23 I show the expected RM profiles as a function of the depth for three values of the magnetic field strength at the galaxy group centre. The dots represent the measured RM values for the south and north lobe if an inclination of 60° is assumed. For the southern lobe I considered a projected distance of $r_{\perp}$=119 kpc while for the northern lobe I considered $r_{\perp}$=194 kpc. In the bottom right panel of Figure 3.23 I show the RM difference between the two lobes versus the source's inclination. The shaded horizontal stripe represents the measured RM difference. I do not have any a priori hint about the source inclination. However, in the 68% of the cases (inclination > 30°) the observed RM can be used to constrain the cluster magnetic field strength, B_0, between 1.75 and 3.5 μG. This is the magnetic field at the cluster centre. Note that according to Equation 3.11 with η = 1, the field strength decreases with radius following the gas density.

In Figure 3.24 I plot 3CR 403.1 in the B_0-density plane from Govoni et al. (2017). The position of the radio source in the plane is consistent with the correlation observed for other galaxy clusters for which the magnetic field strength was determined from the RM analysis. The low central magnetic field found in this work for the poor galaxy cluster around 3CR 403.1 confirms the general trend that fainter central magnetic fields seem to be present in less dense galaxy clusters (Govoni et al. 2017).

3.3.3 3CR 403.1: SRT Background Tests

I analyzed separately the images of the two observing days 19 Nov and 19 Dec 2020, which have comparable noise levels (see Figure 3.25). Although the signal-to-noise ratio is lower than that of the combined image, there is a hint that the negative signal is present in both the individual images. This would exclude that it is an artifact due to peculiar atmospheric fluctuations not captured by the baseline subtraction.

I then repeated the baseline subtraction by: 1) using a linear fit instead of a 2nd-order polynomial fit and 2) by dropping the mask completely and using just the 10% of data from the beginning and end of each individual sub-scan to define the"cold-sky". In both the cases the negative signal around the source is still observed.

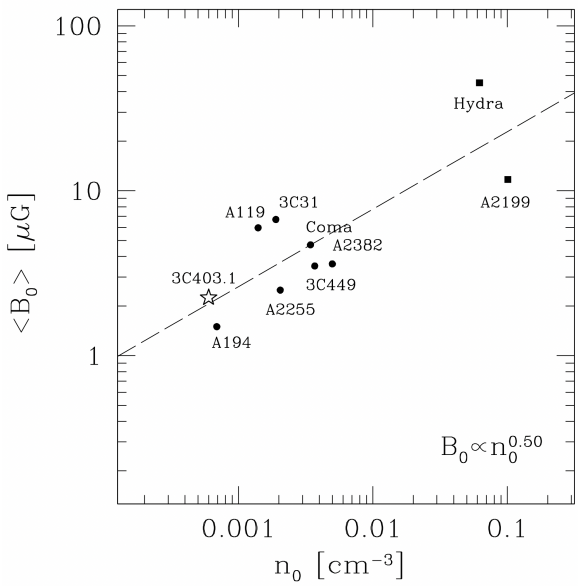

Figure 3.24 Central magnetic field strength $< B_0 >$ vs the central electron density n_0. The dashed line indicates the scaling obtained by a linear fit of the log-log relationship $< B_0 > \propto n_0^{0.50}$. 3CR 403.1 is indicated with a star. The other sources in the plot are discussed in Govoni et al. (2017).

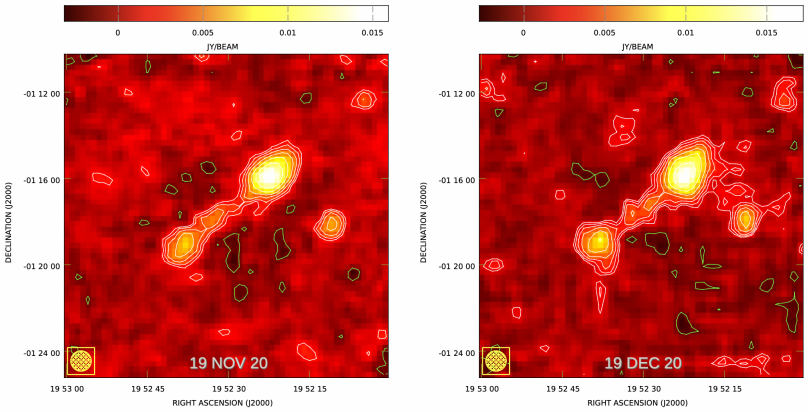

Figure 3.25 Comparison of Nov 19th (*left panel*) versus Dec 19th, 2020 (*right panel*) session. The rms noise levels are 0.60 and 0.52 mJy/beam, respectively. Contours are traced at -3σ, 3σ and scale by $\sqrt{2}$. Negative contours are represented in green.

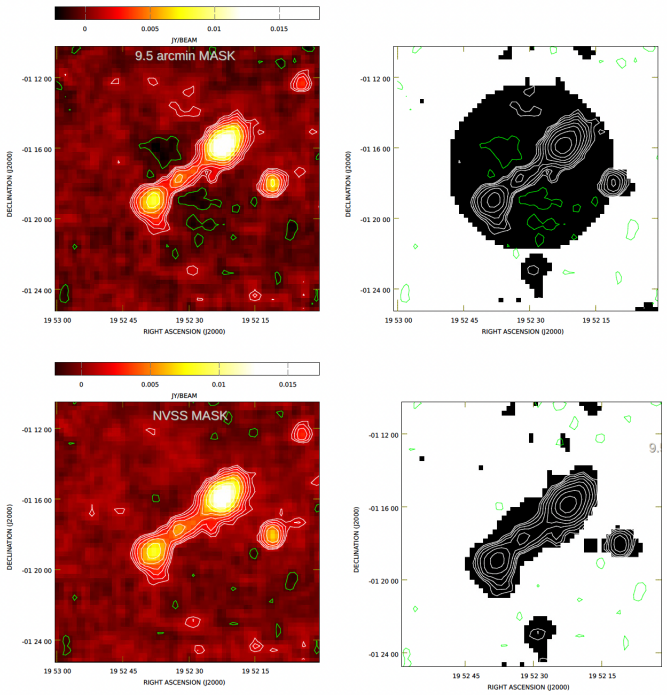

Figure 3.26 Images obtained using the circular mask with a diameter of 9.5′ (*top-left*) and the tailored NVSS mask (*bottom-left*). The rms noise level is 0.39 mJy/beam for both images. Contours are traced at -3σ, 3σ and scale by $\sqrt{2}$ (negative contours are represented in green). Top-right and bottom-right panels show the mask (black pixels) defining the cold-sky region (white pixels) used for the baseline fit.

I also repeated the baseline subtraction by using a smaller, more tailored, mask for 3CR 403.1 at 18.6 GHz based on the NVSS 3σ contour level, see Figure 3.26. In this case the negative signal disappears. However, this test is not conclusive since the negative signal could have been captured and removed along with the cold sky emission. I concluded that new observations over a larger field of view are probably necessary to firmly determine the nature of the negative radio brightness.

3.4 3C 297: Powerful yet Lonely

Note: Section adapted from Missaglia et al. (2023).

This section focuses on 3C 297, a radio-loud quasar for which Spinrad et al. (1985) computed a redshift z=1.406, and suggests the presence of a massive cluster in formation. Spinrad et al. (1985) emphasized the high redshift of 3C 297, and reported the detection of [Mg II], [Ne IV], and [C III] lines in its spectrum. Jackson & Rawlings (1997) took a near-infrared spectrum of 3C 297 between 1.05 and 1.25 μm, detecting a prominent [O III] λ5007 line redshifted to 1.2053 μm corresponding to a redshift measurement z = 1.407.

This source has a large suite of recent multi-wavelength observations. Chiaberge et al. (2015) classify 3C 297 as a merger, using Hubble Space Telescope (*HST*) observations, because of the presence of a double core. Hilbert et al. (2016) reported earlier radio, optical and infrared observations of 3C 297. A VLA map shows a strong, straight lobe of radio emission stretching from the host galaxy to more than 5″ (~ 43 kpc) to the northwest. In addition, 3C 297 has diffuse radio emission to the south of the host galaxy. The southern radio emission includes two knots of optical emission, whose relative position is uncertain given the absence of a radio core to align the radio and the optical/IR. From observations obtained with the UVIS channel of the *HST*'s Wide Field Camera 3 through the F606W filter and with the IR channel through the F140W filter, 3C 297 appears as a compact but resolved core with diffuse emission, with an arc 2″ north of the core and a highly elongated source 1″ to the south. This highly elongated source is suggestive of a recent/ongoing merger as already claimed by Chiaberge et al. (2015). Kotyla et al. (2016) analyzed *HST* data of 21 high-z sources of the 3C catalog and noticed that 3C 297 lacks an associated galaxy cluster or group.

In the *Chandra* Snapshot Survey of 3C sources (Massaro et al. 2015, 2018; Stuardi et al. 2018), 3C 297 shows a complex morphology of its X-ray halo as the likely result of an interaction with the radio jet ("feedback", see e.g. Fabian 2012; Kraft et al. 2012).

The combination of multi-object spectroscopy and *Chandra* data proved to be an efficient method to find that another 3C source belongs to a galaxy cluster. In Madrid et al. (2018) Gemini spectra and Chandra images were used to identify a previously unknown cluster of galaxies around 3C 17, at $z = 0.22$. 3C 17 has been of particular interest because its radio jet is dramatically bent (Morganti et al. 1999; Massaro et al. 2009, 2010), a sign of strong interaction with the ICM.

While the presence of hot gas and the bent radio jet of 3C 297 are typical for galaxy clusters, no galaxies at the same redshift are known in the literature around 3C 297 within ~2 Mpc. These findings prompted to do follow-up observations of 3C 297 in an effort to find potential companions.

In this section, new Gemini multi-object spectroscopy of field galaxies in the vicinity of 3C 297 (see Section 2.2.2), to search for a potential galaxy group or cluster members, and new *Chandra* observations performed to distinguish between the X-ray emission arising from the ICM and that related to the large-scale radio structure are presented. 3C 297 was observed by *Chandra* in 2016 as part of the 3C Snapshot Survey (see Stuardi et al. 2018, for a recent review) for a total exposure of ~ 12 ks (OBSID: 18103).

New *Chandra* ACIS-S data in VERY FAINT mode (P.I. Missaglia) were obtained between 2021 April and 2022 April (see Figure 3.27). The awarded observing time has been divided into 10 observations, for a total nominal exposure time of ~ 200 ks (OBSIDs: 23829; 24352, 24353, 24355, 24356, 24357, 25000, 25001, 25004, 25023).

As anticipated in Section 2.2.3 I extracted X-ray spectra from an elliptical region (see Figure 2.12) with semi-major and minor axes of $12''$ and $7''$, respectively. The axes were selected based on the surface brightness profile in the south-western direction. To investigate if this emission is non thermal, due to inverse Compton scattering (IC) of non-thermal radio-emitting electrons on cosmic microwave background (CMB) photons (IC/CMB; Felten & Rees 1969; Cooke et al. 1978; Harris & Grindlay 1979), or thermal, and therefore related to the ICM, I adopted two different models for the extended emission: (1) Galactic absorption

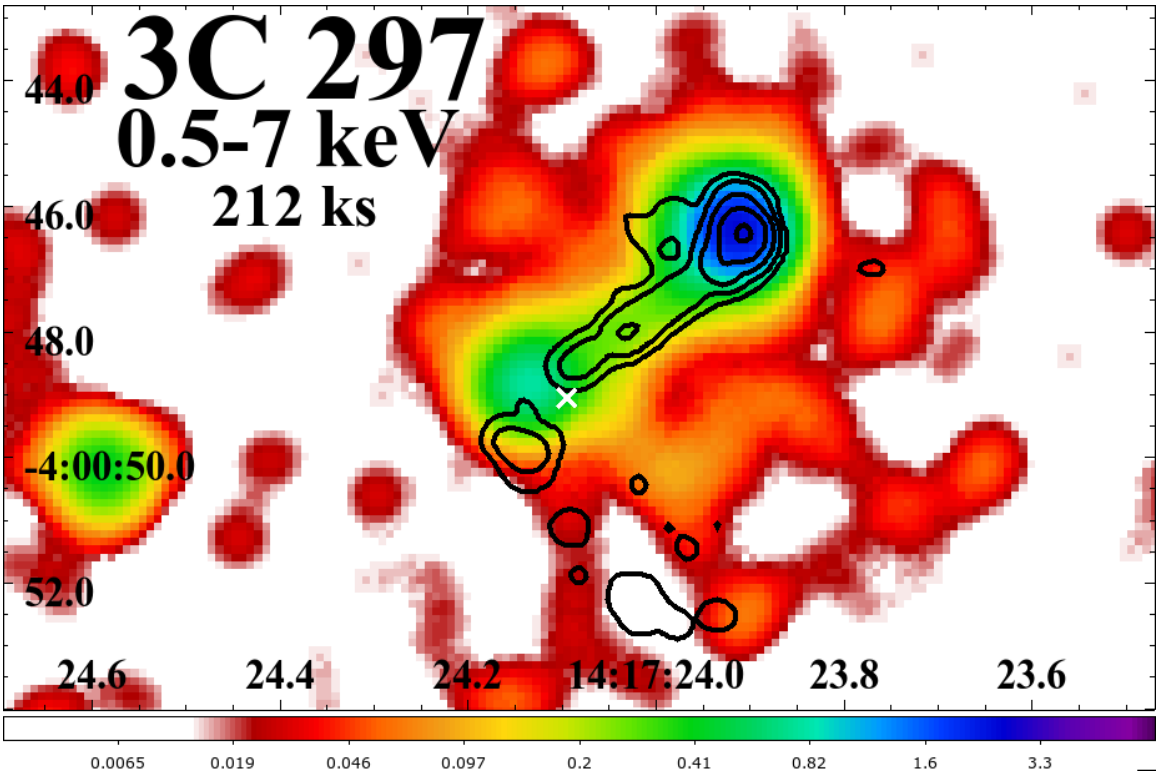

Figure 3.27 *Chandra* image of 3C 297, obtained after merging the available observations, for a total of 212 ks. The image has been filtered in the energy range 0.5-7 keV, binned with a pixel size of 0.123″/pixel and smoothed with a 3.44″ Gaussian kernel. VLA 8.4 GHz (restoring beam 0.357″ × 0.233″) black radio contours are drawn starting at 0.08 μJy beam^{-1}, increasing by factors of six. The position of the radio core, derived from the spectral index map, is marked with a white cross.

plus a power-law (xswabs.absgal*xspowerlaw.pl), and (2) Galactic absorption plus a thermal model (xswabs.absgal*xsapec.therm).

As reported in the literature (see e.g. Massaro & Ajello 2011b; Ghisellini et al. 2015, and references therein) magnetic fields in the lobes of radio galaxies are relatively low, of the order of tens of μG, therefore radiating synchrotron emission inefficiently. At high-z the CMB energy density dominates the radio lobe magnetic field energy density. Therefore, as described by Ghisellini et al. (2014a,b, and references therein; see also Volonteri et al. 2011), at high-z the high energy electron population is depleted due to scattering on the CMB photons, which serves to reduce the radio brightness of the lobes (CMB quenching). At the same time, the increased CMB energy density, enhances the IC/CMB X-ray emission from the lobes (Rees & Sciama 1968).

Yuan et al. (2003) present a *Chandra* analysis of the extended X-ray emission around the high redshift (z=4.301) quasar GB1508+5714. This emission is well described as IC/CMB, and the lack of an obvious detection of radio emission from the extended component could be a consequence of Compton losses on the electron population, or of a low magnetic field. It is also argued that extended X-ray emission produced by IC scattering may be common around high redshift radio galaxies and quasars, demonstrating that significant power is injected into their surrounding by powerful jets.

In the non-thermal scenario (X-ray diffuse emission due to IC/CMB in the lobes) I obtained a photon index equal to $\Gamma = 2.72^{+0.94}_{-0.77}$ and a luminosity of $L_X = 6.6^{+3.3}_{-2.5} \times 10^{43}$ erg s^{-1} (χ^2(dof)=0.63(6)). In the thermal scenario (X-ray emission from the ICM) I could only put an upper bound on the temperature of 6 keV. In this case I obtain an X-ray luminosity of $L_X = 4.5^{+2.0}_{-1.7} \times 10^{43}$ erg s^{-1} (see details in Table 3.7). Given that the diffuse X-rays are not associated with the radio structure, I had to consider also the thermal scenario (X-ray emission from the ICM), even if in the case of cluster emission a spherically symmetric emission should be expected. In this case, adopting a (xswabs.absgal*xsapec.therm) model, I could only put an upper bound on the temperature of 6 keV. This translates to an X-ray luminosity between 0.5 and 7 keV of $L_X = 4.5^{+2.0}_{-1.7} \times 10^{43}$ erg s^{-1} (χ^2(dof)=0.72(6)). To

Results of the X-ray spectral fitting of 3C 297 components.					
Region	Power-Law				
	$N_{H,int}$ (10^{22} cm^{-2})	Γ	norm (10^{-6} cm^{-5})	χ^2_ν(dof)	$L_{X(0.5-7keV)}$ (10^{44} erg s^{-1})
Northern Hotspot	-	1.87 ± 0.15	$4.87^{+0.65}_{-0.22}$	0.68(13)	$2.82^{+0.57}_{-0.46}$
X-ray Halo	-	$2.72^{+0.94}_{-0.77}$	$1.50^{+0.58}_{-0.54}$	0.63(6)	$0.66^{+0.33}_{-0.25}$
Nucleus	1.95×10^{-4}	$1.44^{+0.51}_{-0.31}$	$1.42^{+1.27}_{-0.37}$	0.42(2)	$1.15^{+0.53}_{-0.40}$
	>4.7	1.8*	$2.16^{+0.51}_{-0.45}$	0.48(3)	
	-	$1.44^{+0.33}_{-0.31}$	$1.42^{+0.46}_{-0.39}$	0.28(5)	
Region	Thermal				
	$N_{H,int}$ (10^{22} cm^{-2})	kT (keV)	norm (10^{-6} cm^{-5})	χ^2_ν(dof)	$L_X(0.5-7keV)$ (10^{43} erg s^{-1})
X-ray Halo	-	<6	25^{+34}_{-13}	0.72(6)	$4.5^{+2.0}_{-1.7}$

Table 3.7 Results of the spectral fitting of the X-ray components: northern hotspot, extended emission and nucleus (all highlighted in Figure 2.12). * marks fixed values in the fit.

disentangle the two scenarios, low frequency radio data that could trace the extension of the southern lobe are needed, also to estimate the IC/CMB contribution to the X-ray emission from the lobe region.

Finally, I extracted the spectrum of the nuclear region, i.e. the region that in the optical corresponds to the host galaxy of 3C 297 (the position of the central AGN identified with the radio spectral index map as reported in Stuardi et al. (2018) is marked with a white cross in Figure 3.27). I adopted a model with Galactic and intrinsic absorption, plus a power-law (xswabs.absgal*xszwabs.absint*xspowerlaw.pl). I fitted the spectrum in three different configurations: (1) with photon index, normalization and intrinsic absorption as free parameters; (2) with photon index equals to 1.8 and free intrinsic absorption and normalization, and (3) with no intrinsic absorption. Results of the spectral fitting for the three components are summarized in Table 3.7. The nucleus has an X-ray luminosity of $L_X = 1.15^{+0.53}_{-0.40} \times 10^{44}$ erg s^{-1} between 0.5-7 keV.

Pre-Image and Target Selection

For field spectroscopy, the Gemini Multi-Object Spectrograph was used (GMOS; Hook et al. 2004). The i-band pre-image for the mask design was obtained on 2020 February 18 through program GS-2019B-FT-211 (PI: Madrid) with GMOS at Gemini South (GS). The integration time was 1080 s, taken in clear and 0.75″ seeing conditions.

In the GMOS i-band pre-image (see Figure 3.28), 3C 297 has an i-band magnitude of 20.7 AB mag. Lacking photometric redshifts in the field, the initial target selection was based on the i-band photometry of galaxies in this image. If there was a galaxy cluster around 3C 297, then most members would be considerably fainter than the BCG – in case of a fossil group, by at least 2.5 mag within the virial radius (Dariush et al. 2007). Therefore the high priority target sample was selected from the $21.8 < i < 23.0$ AB mag interval, corresponding to $0.2–3.0 \times 10^{10}\,L_{\odot}$ if at $z \sim 1.4$. The bright cut-off was chosen to reduce the contamination by foreground sources. For targets below the faint cut-off it would be increasingly difficult to determine a spectroscopic redshift, in particular, if they reside in the redshift desert between $z \sim 1.8–2.5$, where redshifted emission lines are absent in the optical wavelength range. Galaxies with i= 23.0–24.0 mag comprised a low-priority sample that the mask-making algorithm could use to fill any remaining spaces in the mask design. After the Gemini mask-making software automatically resolved slit placement conflicts (spatial or spectral overlaps), 40 galaxies – or about 50% of the targets – remained in the mask design. Science targets had slitlets of 1″. While this sample of 40 targets is necessarily incomplete, it is still representative, and can be therefore used to detect a potential cluster population in the spatial vicinity of 3C 297. In addition to these galaxies, there were two alignment stars in wider slits, and one reference star and three galaxies of similar brightness as 3C 297 in narrow science slits, to guide the data processing and judge data quality. 3C 297 was also included, near the center of the mask (see Table 3.8 and Figure 3.28).

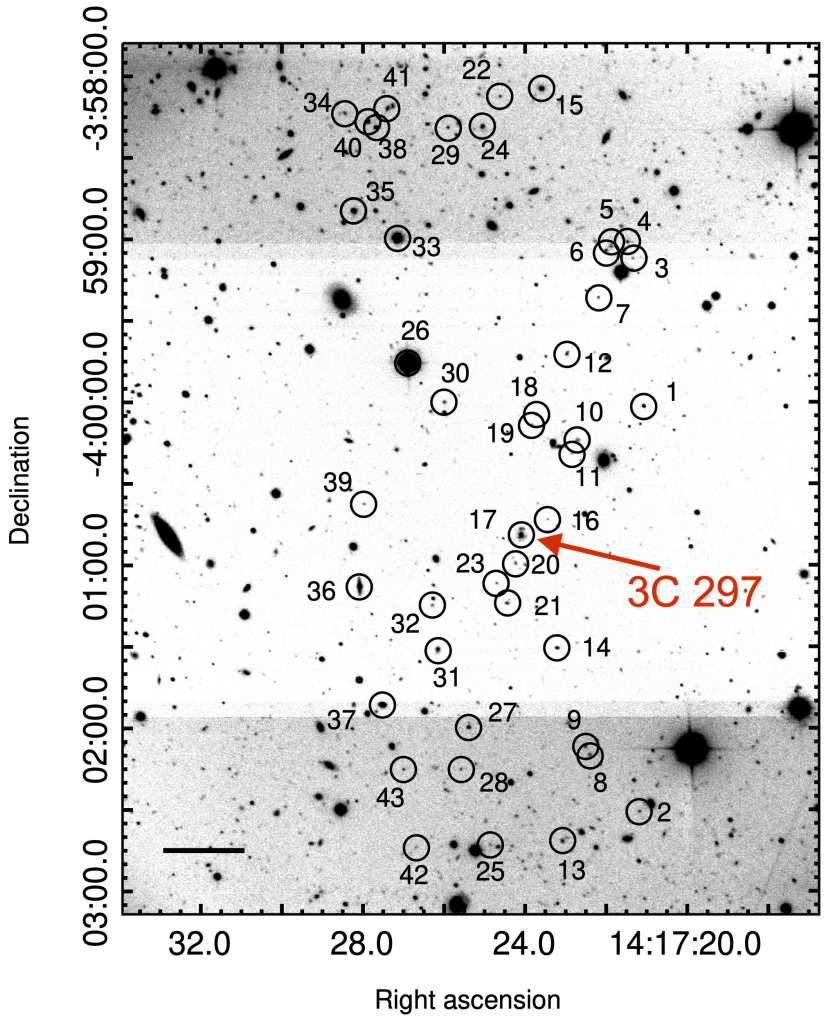

Figure 3.28 Section of the GMOS pre-image of the 3C 297 field. This i-band image has a total exposure time of 1080 s. Numbers correspond to the slit ID. The radio galaxy 3C 297 is close to the center of the image, identified with slit number 17. The bar on the lower left represents 30″. The different background levels are a due to limited processing functionality by the Gemini pipeline that automatically produces the pre-image. North is up and east is left.

Band-Shuffling Mask Design

GMOS was used in band-shuffling mode, which allows for very high slit density in a fairly compact area. Specifically, 1/3 of the detector area or $5.5' \times 1.8'$ are available for the slit placement, corresponding to a projected physical area of 2.8×0.9 Mpc at $z = 1.408$.

During the observations, science targets are observed for 60 s, after which the collected charges are moved ("shuffled") to an unilluminated detector area, and the telescope makes a small offset. During the next 60 s, at the offset position, the slits collect sky signal, only. Then the "target" charges are shuffled back under the slit, and the sky charges are moved onto a different storage area. This is repeated for a total of 600 s in a single exposure, for an effective on-source integration time of 300 s. Very accurate sky subtraction and fringe correction become possible at longer wavelengths dominated by airglow, with just a single readout, and redshifts can be secured for fainter galaxies. For details about this mode see Glazebrook & Bland-Hawthorn (2001).

Instrumental Setup

The instrumental setup is optimized to identify galaxies at a redshift of $z \sim 1.4$. Many characteristic emission lines of active and star-forming galaxies, such as [MgII]λ2799, [OII]λ3727, [NeIII]λ3869, and Hδ, would be redshifted to the 670–990 nm range. This interval then also includes the characteristic Balmer break and the Ca H+K absorption lines of older stellar populations in elliptical galaxies. The instrumental setup for GMOS, therefore, used the R400 grating with the OG515 order sorting filter, and a central wavelength of 790 nm. The associated spectral resolution for a slit width of $1''$ is $R = 960$. The main observable wavelength interval with this setup was 510–1050 nm, with – negligible – second order overlap above 1020 nm. Depending on how close a source was located to the edge of the masking area, the spectral range was truncated by the detector edges either at the blue or the red end. Typically, a 450 nm wide interval within 510–1050 nm for each source was covered.

Observations

One month after the original mask was cut and tested, Gemini suspended its science operations due to the pandemic, preventing the program to proceed with the spectral observations. By the time Gemini South reopened, the GMOS-S detector was experiencing considerable charge transfer efficiency issues that were prohibitive for these band-shuffling observations.

The mask was thus redesigned for identical band-shuffling observations with GMOS-N at Gemini North, using the GMOS-S pre-image. Spectra were obtained on 2021 April 13 and 15 under program GN-2021A-FT-203 (PI: Madrid), with an effective on-source integration time of $11 \times 300 = 3300$ s, and an image seeing of $0.5''$–$0.8''$. The detector was binned 2×2 (in the spatial and spectral dimensions), and observed two central wavelength settings of 790 nm and 800 nm to cover the detector gaps. Calibration data consisted of biases, lamp and twilight flats, and CuAr arc spectra for wavelength calibration.

The obtained GMOS spectrum of 3C 297 is displayed in Figure 3.29. This spectrum has prominent emission lines: Mg II, O III, He II, [Ne V], [O II], [Ne III]. From the position of the different lines, it was possible to measure a mean redshift of z=1.408 ±0.001.

Before undertaking a detailed spectral analysis, a redshift correction of z=1.408 to the spectrum of 3C 297 was applied, together with a Galactic extinction correction of $A_{\lambda,V}$=0.146 mag using the extinction maps of Schlafly & Finkbeiner (2011b) and the Cardelli et al. (1989) extinction law. In order to increase the signal-to-noise (S/N) of the emission lines, the spectrum was smoothed using a Gaussian filter of 3 pixels width. This smoothing preserves the spectral resolution while suppressing high-frequency noise.

The spectrum of 3C 297 is essentially free of either blue or red continuum emission. Moreover, there is no detection of stellar absorption features. The presence of Mg II 2798 Å and [Ne V] $\lambda\lambda$3345,3424 is further proof of the AGN nature of this object. The latter doublet is conspicuous, suggesting that 3C 279 has high-ionization gas.

The strongest line detected in the observed wavelength interval corresponds to [O II] $\lambda\lambda$3726,3729 (hereafter [O II] λ3728). This line profile displays a broad, prominent

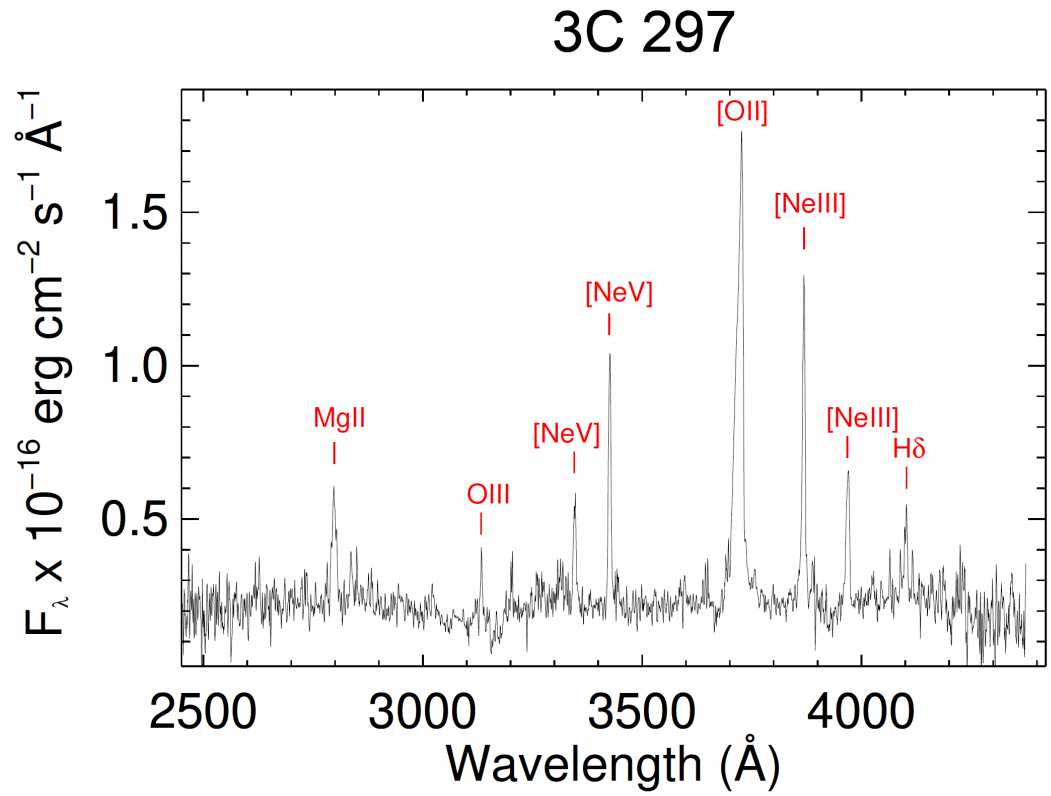

Figure 3.29 New GMOS spectrum of 3C 297. The spectrum is displayed with a redshift correction of z=1.408.

Table 3.8 Targets of the GMOS multi-slit mask.

Slit	R.A.	Dec.	m_i	z
1	14:17:21.076	-4:00:01.45	21.45	—
2	14:17:21.177	-4:02:30.65	23.37	—
3	14:17:21.344	-3:59:07.30	23.91	☆
4	14:17:21.475	-3:59:01.19	22.92	—
5	14:17:21.871	-3:59:02.67	22.96	—
6	14:17:22.008	-3:59:04.24	23.01	1.156
7	14:17:22.193	-3:59:21.65	23.26	0.633
8	14:17:22.400	-4:02:09.94	23.09	1.263
9	14:17:22.525	-4:02:06.74	22.87	1.163
10	14:17:22.737	-4:00:14.41	22.68	1.029
11	14:17:22.855	-4:00:19.08	23.81	—
12	14:17:22.977	-3:59:42.29	22.51	1.523
13	14:17:23.077	-4:02:41.65	22.63	—
14	14:17:23.204	-4:01:30.48	22.28	—
15	14:17:23.588	-3:58:04.49	21.23	0.215
16	14:17:23.455	-4:00:43.17	24.25	—
17	**14:17:24.102**	**-4:00:48.93**	**20.95**	**1.408**
18	14:17:23.719	-4:00:04.45	22.74	—
19	14:17:23.839	-4:00:08.48	23.22	1.137
20	14:17:24.232	-4:00:59.38	23.21	—
21	14:17:24.447	-4:01:14.20	22.89	—
22	14:17:24.621	-3:58:07.42	23.44	1.343
23	14:17:24.702	-4:01:06.75	23.57	1.577
24	14:17:25.052	-3:58:18.53	21.91	—
25	14:17:24.861	-4:02:43.03	23.80	—
26	14:17:26.898	-3:59:45.86	15.12	☆
27	14:17:25.387	-4:01:59.64	21.88	—
28	14:17:25.583	-4:02:15.24	23.56	0.732
29	14:17:25.901	-3:58:18.92	23.10	2.577
30	14:17:25.989	-4:00:00.01	22.87	—
31	14:17:26.160	-4:01:30.80	21.69	0.211
32	14:17:26.292	-4:01:14.94	23.35	1.181
33	14:17:27.150	-3:58:59.79	17.44	☆
34	14:17:28.444	-3:58:13.55	23.12	—
35	14:17:28.238	-3:58:49.56	20.34	—
36	14:17:28.087	-4:01:07.61	20.20	—
37	14:17:27.513	-4:01:51.40	20.38	0.244
38	14:17:27.675	-3:58:18.69	21.72	0.295
39	14:17:27.965	-4:00:37.53	23.32	—
40	14:17:27.882	-3:58:16.70	21.41	0.605
41	14:17:27.389	-3:58:12.06	22.42	—
42	14:17:26.692	-4:02:43.83	23.98	1.199
43	14:17:27.001	-4:02:15.24	23.37	—

Column 1: Slit number; Column 2: Right Ascension (J2000); Column 3: Declination (J2000); Column 4: apparent i-band magnitude; Column 5: redshift. Slits 3, 26, and 33 are stars denoted with the ☆ symbol. 3C 297 is highlighted in bold.

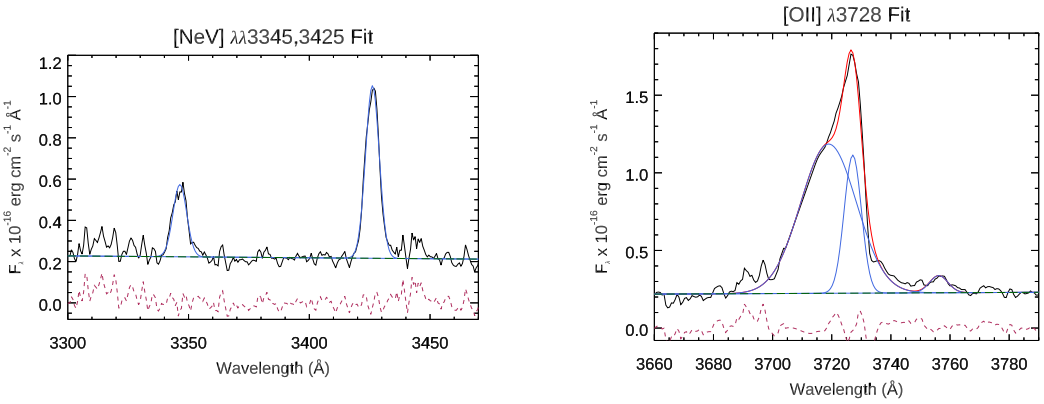

Figure 3.30 Example of the Gaussian decomposition applied to the observed emission line profiles. *Left Panel*: Fit to the coronal lines [Ne V] $\lambda\lambda$ 3345, 3425. *Right Panel*: [O II] $\lambda\lambda$ 37286, 3729. For this latter line, a second blueshifted, broad component of FWHM=1790 km s^{-1} was necessary to reproduce the observed profile. In both panels, the observed profile is in black, individual Gaussians are in blue, the total fit in red. The green line is the continuum level and the dashed maroon line is the residual after subtraction of the fit.

blue asymmetry (see below), indicating the presence of powerful outflows in the center of the radio-galaxy. In blue-asymmetric oxygen lines a component is usually shifted to the blue by a few hundred km/s or more, relative to the systemic velocity and is significantly broader than the narrower component. In some quasars, this blueshifted line can display FWHM values of a few thousand km/s and the centroid of the line shifted by several hundred km/s relative to the systemic velocity (see Zakamska & Greene (2014) and discussion below).

3.4.1 The AGN Activity in 3C 297

The continuum emission in 3C 297 has no hints of either a blue continuum, typical of Type I AGN, or stellar absorption features, usually observed in Type II AGN. However, the detection of coronal lines of [Ne V], usually associated with AGN, confirms the presence of an active nucleus in this object (see Figure 3.29).

Presence of broad lines features indicative of broad line region (BLR) was searched. The only permitted lines, detected at a 3σ level, are those of Mg II λ2798, O III λ3133 and Hδ at 4101 Å(see Figure 3.29). The former is significantly broader (FWHM of 1059 km s^{-1})

Table 3.9 Identifications, integrated fluxes, and FWHM of the lines detected in the spectrum of 3C 297.

Line	Wavelength (Å)	Flux $\times 10^{-16}$ (erg cm^{-2} s^{-1})	FWHM (km s^{-1})
Mg II	2797.70	4.23±0.49	1059
O III	3133.70	1.28±0.13	651
[Ne V]	3346.41	2.48±0.30	609
[Ne V]	3426.13	5.92±0.30	595
[O II] broad	3718.94	22.73±0.93	1704
[O II]	3727.11	6.46±0.28	547
[Ne III]	3868.46	8.45±0.39	600
[Ne III]	3968.95	3.97±0.39	585
Hδ	4101.34	2.38±0.38	610

All lines but Mg II and [O II] broad (see Fig. 3.30 right panel) are spectroscopically unresolved (the instrumental FWHM is 6.8 Å.)

than most forbidden lines (FWHM $\sim$ 500 – 600 km s^{-1}) (Osterbrock & Ferland 2006). However, Mg II λ2798 is actually a doublet, (λ2791 and λ2798), and at spectral resolution the individual components cannot be resolved. With an intrinsic FWHM of 600 km s^{-1}, the Mg II doublet is observed as a broad blended profile.

From the lack of continuum features typical of Type I AGN, and the absence of broad components in the permitted lines, 3C 297 can be classified as a Type II radio-source.

3.4.2 Outflowing Ionized Gas

The broadest feature measured in the spectrum of 3C 297 corresponds to a blueshifted component found in the forbidden [O II] λ3728 line. This feature is centered at 3719 Å, with a FWHM of 1790 km s^{-1}. In addition, a narrow component associated to the same transition has been detected, with a FWHM of 547 km s^{-1}, very similar to the width of the remaining narrow forbidden lines, see Figure 3.30. Because the broad feature is associated with a forbidden line, its origin is outside a putative Broad Line Region (BLR). The gas density in a BLR region is orders of magnitude larger than the critical density of the transition leading to the [O II] λ3728 doublet. If the broad component is indeed associated with [O II] λ3728, it is displaced by 657 km s^{-1} to the blue of the rest-frame wavelength.

[O III] λ5007 falls outside the spectral range of the data. The only published spectrum covering that line is the one of Jackson & Rawlings (1997), that has low spectral resolution (R = 380). Although the doublet [O III] $\lambda\lambda$4959,5007 is clearly detected, it is not possible to confirm from the Jackson & Rawlings (1997) data the presence of an obvious blueshifted asymmetric line. However, several detections of broad blue-shifted features associated to [O II] have been reported in the literature. For instance, Balmaverde et al. (2016) studied a sample of 224 quasars selected from the Sloan Digital Sky Survey (SDSS) at z < 1. They focused on ionized gas outflows traced by the optical [O III] and [O II] lines. Most of the quasar spectra show asymmetries and broad wings in both lines, although the former has larger wings than the latter. These line asymmetries in quasars are generally interpreted as signs of outflows instead of inflows from the farside of the emitting region. Indeed, Perna et al. (2015) detected outflows extending to ~10 kpc from the central black hole using [O II]. Zakamska & Greene (2014) found that [O II]$\lambda\lambda$3726,3729 also shows outflow signatures, in some cases consistent with extremely broad features seen in [O III] (see also Davies et al. (2015)). It is possible to conclude that the strong asymmetry observed in [O II] points to an extreme gas outflow in 3C 297. Given the evidence for strong outflows from the spectra, a disturbed X-ray atmosphere might be expected. Even if the number of counts is very low and therefore any statement should be tentative, in the two areas marked with a dashed red circle and ellipse I highlighted an excess of X-ray counts. In the south-western region ($4''$ circle) this excess has a Gaussian significance of 5.8σ, while the excess in the north-eastern direction (ellipse $4''\times 2''$) has a significance of ~3.2σ.

3.4.3 Optical Sources in the Field

As expected, the spectra of the 39 science targets in the field of 3C 297 have different signal-to-noise ratios (S/N). The spectra for those field sources for which redshifts have been derived can be found in the published article.

Some objects have bright emission lines that are easy to identify (e.g. [O III] for slits 28 & 40, Hα for slits 15 and 31). With only four exceptions discussed below, all of the spectra allow the identification of at least two spectral lines, even in those spectra with low S/N.

The redshifts of slits 6, 12, 19, and 42 are derived using the [O II] line only. [O II] is the most probable line observed in these spectra for the following reasons. If it were [O III] (λ5007 Å) the [O III] (λ4960 Å) line would be detected as well. If the single line of these four spectra were [NeIII] (λ3869 Å) the [OII] and [O III] lines would be present too.

The main conclusion of this field spectroscopy is that no galaxies have been identified at the same redshift of 3C 297.

3.4.4 Is 3C 297 a High-z Fossil Group?

The main findings for 3C 297, namely the presence of an X-ray luminous hot gas halo and a lack of companion galaxies, would make it a candidate for a so-called fossil group (see e.g. Ponman et al. 1994; Mendes de Oliveira & Carrasco 2007; Schirmer et al. 2010 and Aguerri & Zarattini 2021 for a recent review).

Fossil groups, or fossil clusters, are systems where the closest M^* galaxies have dynamically collapsed onto the BCG due to dynamic friction (Chandrasekhar 1943), while the group's common X-ray halo would remain visible due to its long cooling time and AGN feedback (Jones et al. 2003). Fossil groups are defined by the presence of an X-ray halo (with $L_X \geq 10^{42}$ erg s^{-1}, that is compatible with our estimate, see beginning of the Section) and a characteristic magnitude gap of ~ 2 mag between their BCG and the second-brightest group member (Kundert et al. 2017; Aguerri & Zarattini 2021).

Observationally, catalogs of fossil groups are usually limited to $z < 0.5$. For instance, the highest redshift for the fossil groups reported by a recent survey is $z = 0.442$ (Johnson et al. 2018). In the Hess et al. (2012) sample, the highest redshift fossil group is 0.489. Voevodkin et al. (2010) presented an X-ray selected sample of X-ray luminous fossil groups at $z < 0.2$. Pratt et al. (2016) studied four very X-ray luminous fossil groups detected in

the Planck Sunyaev-Zel'dovich Survey whose temperatures are 5-6 keV with total masses exceeding 10^{14}M$\odot$.

Simulations show that a fossil system may assemble half of its mass in dark matter by redshift $z > 1$, and that the assembled mass at any redshift is generally higher in a fossil than in regular groups (Dariush et al. 2007). The existence of a fossil group at the redshift of 3C 297 is therefore compatible with theoretical expectations.

High redshift examples of fossil groups are very limited with current record holders standing at z=0.47 (Yoo et al. 2021) and z=0.7 (Grillo et al. 2013). The fact that no physical companion galaxies were found, making 3C 297 one of the highest redshift fossil groups known to date.

Hess et al. (2012) sing both SDSS and VLA data, demonstrated that fossil groups host radio-loud AGN detected at 1.4 GHz. 3C 297, being a stronger source than the AGN in the sample studied by Hess et al. (2012), shows that fossil groups can also host powerful radio sources. As reported in Lotz et al. (2008), time-scales of galaxy mergers are of the order of 1 Gyr. Even if poorly constrained, 3C 297 has a cooling time longer than 1 Gyr.

3.5 Conclusions

In this last section I summarize the results obtained for the sources presented in this chapter.

3.5.1 3C Unidentified

In the case of the 3C unidentified sources I can summarize the results as follows:

- six of the seven sources (all but 3CR 409), show a clear detection of the radio core at 1.5 GHz, 6 GHz and 10 GHz. These radio images, retrieved from the historical VLA archive, were all manually reduced and for five sources I also gave a tentative FR II radio classification;
- I found IR counterparts to all the radio cores, thanks to the WISE archival images. This allowed me to estimate the photometric redshift of the counterparts using the

magnitudes at 3.4 and 4.6 μm as described in Glowacki et al. (2017). This method allowed me also to give tentative classifications (LERG/HERG/QSO) of the sources in the sample. Most of the sources are classified as QSOs with a probability $\gtrsim 60\%$, while 3CR 131 and 3CR 454.2 are classified as LERGs, with the same probability;

- only three sources (namely 3CR 91, 3CR 158 and 3CR 390) of the seven with an infrared counterpart are also detected in the optical band using Pan-STARRS images. For the other sources I have obtained an $N_{H,int}$ value of the order of $\sim 10^{23}$ cm^{-2}, and corresponding levels of dust obscuration are likely the reason for the non-detection of the optical counterpart;

- I found *Chandra* X-ray counterparts for all the radio cores. Then, for 3CR 91, 3CR 390, 3CR 490 and 3CR 428, I also estimated the X-ray spectral indexes (α_X=0.48-0.80) and the intrinsic absorption $N_{H,int}$, via spectral analysis. The spectral indexes are compatible with results reported in the literature for the nuclei of QSOs and LERGs;

- I detected X-ray emission arising from the X-ray counterpart of the northern radio jet in 3CR 158 as well as that associated with the radio bridge in 3CR 390;

- our *Chandra* observations revealed also the presence of extended X-ray emission, the hallmark of galaxy clusters, around 3CR 409 and 3CR 454.2. I performed a spectral analysis, but temperature or spectral parameters are unconstrained. This demands deeper *Chandra* observations to make more conclusive measures of the temperature, mass, and luminosity of the clusters.

Regarding the tentative classification of the sources in the sample, my results are:

- 3CR 91 has an 8 GHz radio structure similar to an FR II radio galaxy. From the WISE magnitudes of the counterpart it can be classified as a QSO at $z \sim 0.2$. The Pan-STARRS core counterpart is detected, and the intrinsic absorption value estimated from X-ray spectral fitting is of the same order of magnitude as the Galactic one. I therefore classify this source as a QSO at $z \sim 0.2$.

- 3CR 131 has an 8 GHz radio structure similar to an FR II radio galaxy. From the WISE magnitudes of the counterpart, it can be classified as a LERG at $z \sim 0.4$. There is no Pan-STARRS detected counterpart, but there are not enough nuclear counts in the *Chandra* image to perform a spectral analysis. I classify this source as an FR II-LERG at $z \sim 0.4$.

- 3CR 158, at 8 GHz, is similar to an FR II, and I detected X-ray extended emission aligned with the radio jet structure. The photometric redshift estimate from WISE magnitudes is $z \sim 4$, and the source is classified as a QSO. The poor statistics do not allow me to perform a spectral analysis of the source nucleus. The Pan-STARRS core counterpart is detected with $m_R = 20.6$, the highest of the sample. From these results, I classify this source as a high redshift ($\gtrsim 4$) QSO.

- 3CR 390 does not have a clear radio morphology, showing two sided lobes. From the WISE magnitudes of the counterpart, this source can be classified as a QSO at $z \sim 0.4$. This source has a detected Pan-STARRS nuclear counterpart, and from the X-ray spectral fitting, I estimate a nuclear intrinsic absorption comparable to the Galactic one. I classify this source as a QSO at $z \sim 0.4$.

- 3CR 409 shows an FR II radio morphology, and from the WISE magnitudes this source is classified as a QSO at $z \sim 0.9$. This source appears to lie in a cluster of galaxies, and does not have a detected Pan-STARRS nuclear counterpart. From the X-ray spectral fitting, I estimate an intrinsic absorption $\sim 10^{23}$ cm^{-2}. I therefore classify this source as a highly-absorbed QSO at $z \sim 0.9$.

- 3CR 428 features an FR II-like radio morphology. The WISE magnitudes of this source classify it as a QSO at $z \sim 2.3$. No Pan-STARRS nuclear counterpart is detected, and from the X-ray spectral fit I estimate an intrinsic absorption $\sim 10^{23}$ cm^{-2}. I classify this source as a highly-absorbed QSO at $z \sim 2.3$.

- 3CR 454.2 features an FR II-like radio morphology. From the WISE magnitudes I classify this source as a LERG at $z \sim 0.3$. I do not detect a nuclear Pan-STARRS counterpart. This source appears to lie in a galaxy cluster with disturbed ICM morphology, however the available *Chandra* data do not allow nuclear spectral analysis and so no estimate of the intrinsic absorption, or the ICM temperature. Deeper X-ray observations are needed to draw firm conclusions on this source.

In conclusion, I have four sources with a predicted low-z host ($z \sim 0.2 - 0.4$) namely 3CR 91, 3CR 131, 3CR 390, 3CR 454.2. Three sources are classified as high-z (> 0.9), highly-absorbed QSO, namely 3CR 158, 3CR 409 and 3CR 428. In the case of 3CR 158, since the estimated photometric redshift is that of a very high-z source, deeper *Chandra* observations are required to verify this estimate.

3.5.2 3CR 403.1

For 3CR 403.1, I performed a spectral-polarimetric study of this FR II radio galaxy, hosted in a small galaxy group of dwarf galaxies, as shown in the observations performed by VLT/MUSE as part of the MURALES survey (see Figure 3.19). This study was carried out using new high frequency radio data from the SRT and archival data from VLA and MWA. Radio data were complemented with X-ray data from *Chandra*, obtained as part of the 3CR Snapshot Survey (see also recent observations in Massaro et al. 2018; Stuardi et al. 2018; Jimenez-Gallardo et al. 2020) and optical observations available from the MURALES survey. Results can be summarized as follows:

- Assuming that this group is virialized, I used the velocity dispersion of the five companion galaxies detected with MUSE to estimate the total mass of the system as $M_{env} = 7.5 \times 10^{11} M_{\odot}$.

- I measured the flux density of 3CR 403.1 for the entire source and its components, radio core region and lobes, separately, using new SRT observations, complemented

with archival NVSS, GLEAM and VLSSr radio data (lower frequencies). Results of the spectral analysis are shown in Figure 3.20.

- Given the values of the parameters obtained from the fit of the radio spectrum for the entire radio source (injection spectral index and break frequency), I measured the equipartition magnetic field, finding a value of B_{eq} = 2.37 μG. This value was used to compute the spectral age of the source, being 93 Myr.

- From the new high-frequency SRT data at 18.6 GHz I unexpectedly observed a flux depression in two regions perpendicular to the radio axis (see green contours in Figure 3.18) with a level of significance higher than 3σ. This negative radio signal is cospatial with the extended X-ray emission detected in the *Chandra* observation, that I interpreted as thermal radiation from the hot ICM surrounding 3CR 403.1.

- Thus, I re-analysed the *Chandra* observation, focusing on the region of the radio flux depression (see Figure 3.18). I performed a spectral analysis of the X-ray emission to estimate the temperature and density of the ICM in that region. I found $kT = 0.85^{+0.07}_{-0.08}$ keV and $n_e = (4.6 \pm 0.3) \times 10^{-4} \mathrm{cm}^{-3}$ that corresponds to a gas mass equal to $M_{gas} \simeq (2.2 \pm 0.1) \times 10^{11} M_{\odot}$.

- The radio Comptonization parameter would require a much larger ICM pressure than that estimated from the X-rays and therefore I investigated the possibility that the negative signal in the SRT image is an artifact, but the results were not conclusive. I obtained an estimate of the Comptonisation parameter both in the radio ($y_R = (2.0 \pm 0.4) \times 10^{-5}$ Mpc^2) and in the X-ray ($y_X = 3.82^{+0.40}_{-0.43} \times 10^{-8}$ Mpc^2) from an elliptical region encompassing the nucleus of 3CR 403.1 where I detected the highest value of the negative signal. From these calculations I find that the Comptonization parameter values obtained with the radio (y_R) and X-ray (y_X) are not consistent. I investigated the possibility that the negative signal in the SRT image is an artifact, but the results were not conclusive. If the negative signal is considered as real, than this implies that (i) the X-ray observations are not deep enough to make a more

accurate estimate or (ii) it is possible to speculate that part of the discrepancy of the two values is due to the presence of a pool of non-thermal, mildly relativistic old electrons, ejected from the radio source's core in a past episode of activity (as suggested by a VLA P-band observation).

- Finally, I used SRT data combined with NVSS to derive the rotation measure (RM) images of 3CR 403.1 (see Figure 3.23). From this estimate I concluded that the ICM surrounding 3CR 403.1 is permeated by a magnetic field with strength between 1.75 and 3.5 μG. Thus, I compared this value of the magnetic field with the density found from the X-ray analysis. The position of the radio source in the plane is consistent with the correlation observed for the other galaxy clusters for which the magnetic field strength was determined from the RM analysis.

Due to the low statistics of the available X-ray data, no firm estimate of the Comptonization parameter can be drawn. I plan to collect more radio data to investigate the emission detected by the VLA in P band, possibly related to past AGN activity and thus the presence of cold electrons responsible of the flux decrease observed in SRT data.

I want to stress that the SRT observations of 3CR 403.1 gave intriguing results, but this should be a starting point for an exploratory program of powerful radio sources looking for similar effects, opening a new window on the scientific results achievable with the SRT.

3.5.3 3C 297

I have presented an optical/X–ray study of the high redshift (z=1.408) quasar 3C 297. In the 3C *Chandra* Snapshot observation, I observed a complex morphology of the X-ray halo and the detection of the X-ray counterpart of the radio hotspot visible in the VLA image at 8.4 GHz. With new deeper *Chandra* observations, I performed the spectral analysis of the bright X-ray hotspot and of the nuclear region. The nucleus is not detected in the radio image, therefore I used a tentative position obtained from an available spectral index map. I obtained an X-ray luminosity of $L_X = 2.82^{+0.57}_{-0.46} \times 10^{44}$ erg s^{-1} for the hotspot and

$L_X = 1.15^{+0.53}_{-0.40} \times 10^{44}$ erg s^{-1} for the nucleus, in the energy range 0.5-7 keV. I investigated if the extended X-ray emission had a thermal or non-thermal origin, i.e. if it was due to the hot gas or to IC/CMB. It was only possible to put an upper bound on the temperature being 6 keV. Given the distribution of the surrounding X-ray gas, that 3C 297 could be the BCG of a galaxy cluster and thus I searched for fainter companions/galaxy members. With new GMOS observations, optical spectra of the neighbouring sources of our target have been obtained, and for 19 of them their redshifts were measured. The main conclusion of this field spectroscopy is that no galaxies at the same redshift as 3C 297 has been identified. Therefore it is possible to postulate that 3C 297 is a fossil group, being the first at such high redshift. From the optical spectral analysis, the line profile displays a broad, prominent blue asymmetry, indicating the presence of powerful ionized gas outflows in the center of the radio-galaxy.

References

Aguerri, J. A. L. & Zarattini, S. 2021, Universe, 7

Baldi, R. D., Chiaberge, M., Capetti, A., Sparks, W., Macchetto, F. D., O'Dea, C. P., Axon, D. J., Baum, S. A., & Quillen, A. C. 2010, ApJ, 725, 2426

Balmaverde, B., Capetti, A., Marconi, A., Venturi, G., Chiaberge, M., Baldi, R. D., Baum, S., Gilli, R., Grandi, P., Meyer, E., Miley, G., O'Dea, C., Sparks, W., Torresi, E., & Tremblay, G. 2019, A&A, 632, A124

Balmaverde, B., Capetti, A., Marconi, A., Venturi, G., Chiaberge, M., Baldi, R. D., Baum, S., Gilli, R., Grandi, P., Meyer, E. T., Miley, G., O'Dea, C., Sparks, W., Torresi, E., & Tremblay, G. 2021, A&A, 645, A12

Balmaverde, B., Marconi, A., Brusa, M., Carniani, S., Cresci, G., Lusso, E., Maiolino, R., Mannucci, F., & Nagao, T. 2016, A&A, 585, A148

Basu, K., Vazza, F., Erler, J., & Sommer, M. 2016, A&A, 591, A142

Baum, S. A., Zirbel, E. L., & O'Dea, C. P. 1995, ApJ, 451, 88

Bennett, A. S. 1962, MmRAS, 68, 163

Bennett, C. L., Larson, D., Weiland, J. L., & Hinshaw, G. 2014, ApJ, 794, 135

Best, P. N. & Heckman, T. M. 2012, MNRAS, 421, 1569

Birkinshaw, M. 1999, Phys. Rep., 310, 97

Bolli, P., Orlati, A., Stringhetti, L., Orfei, A., Righini, S., Ambrosini, R., Bartolini, M., Bortolotti, C., Buffa, F., Buttu, M., Cattani, A., D'Amico, N., Deiana, G., Fara, A., Fiocchi, F., Gaudiomonte, F., Maccaferri, A., Mariotti, S., Marongiu, P., Melis, A., Migoni, C., Morsiani, M., Nanni, M., Nasyr, F., Pellizzoni, A., Pisanu, T., Poloni, M., Poppi, S., Porceddu, I., Prandoni, I., Roda, J., Roma, M., Scalambra, A., Serra, G., Trois, A., Valente, G., Vargiu, G. P., & Zacchiroli, G. 2015, Journal of Astronomical Instrumentation, 4, 1550008

Bolton, J. G. & Ekers, J. 1966, Australian Journal of Physics, 19, 559

Bridle, A. H. 1984, AJ, 89, 979

Buttiglione, S., Capetti, A., Celotti, A., Axon, D. J., Chiaberge, M., Macchetto, F. D., & Sparks, W. B. 2011, A&A, 525, A28

Cardelli, J. A., Clayton, G. C., & Mathis, J. S. 1989, ApJ, 345, 245

Cavaliere, A. & Fusco-Femiano, R. 1976, A&A, 49, 137

Chambers, K. C., Magnier, E. A., Metcalfe, N., Flewelling, H. A., Huber, M. E., Waters, C. Z., Denneau, L., Draper, P. W., Farrow, D., Finkbeiner, D. P., Holmberg, C., Koppenhoefer, J., Price, P. A., Rest, A., Saglia, R. P., Schlafly, E. F., Smartt, S. J., Sweeney, W., Wainscoat, R. J., Burgett, W. S., Chastel, S., Grav, T., Heasley, J. N., Hodapp, K. W., Jedicke, R., Kaiser, N., Kudritzki, R. P., Luppino, G. A., Lupton, R. H., Monet, D. G., Morgan, J. S., Onaka, P. M., Shiao, B., Stubbs, C. W., Tonry, J. L., White, R., Bañados, E., Bell, E. F., Bender, R., Bernard, E. J., Boegner, M., Boffi, F., Botticella, M. T., Calamida, A., Casertano, S., Chen, W. P., Chen, X., Cole, S., Deacon, N., Frenk, C., Fitzsimmons, A., Gezari, S., Gibbs, V., Goessl, C., Goggia, T., Gourgue, R., Goldman, B., Grant, P., Grebel, E. K., Hambly, N. C., Hasinger, G., Heavens, A. F., Heckman, T. M., Henderson, R., Henning, T., Holman, M., Hopp, U., Ip, W. H., Isani, S., Jackson, M., Keyes, C. D., Koekemoer, A. M., Kotak, R., Le, D., Liska, D., Long, K. S., Lucey, J. R., Liu, M., Martin, N. F., Masci, G., McLean, B.,

Mindel, E., Misra, P., Morganson, E., Murphy, D. N. A., Obaika, A., Narayan, G., Nieto-Santisteban, M. A., Norberg, P., Peacock, J. A., Pier, E. A., Postman, M., Primak, N., Rae, C., Rai, A., Riess, A., Riffeser, A., Rix, H. W., Röser, S., Russel, R., Rutz, L., Schilbach, E., Schultz, A. S. B., Scolnic, D., Strolger, L., Szalay, A., Seitz, S., Small, E., Smith, K. W., Soderblom, D. R., Taylor, P., Thomson, R., Taylor, A. N., Thakar, A. R., Thiel, J., Thilker, D., Unger, D., Urata, Y., Valenti, J., Wagner, J., Walder, T., Walter, F., Watters, S. P., Werner, S., Wood-Vasey, W. M., & Wyse, R. 2016, arXiv e-prints, arXiv:1612.05560

Chandrasekhar, S. 1943, ApJ, 97, 255

Chiaberge, M., Capetti, A., & Celotti, A. 2000, A&A, 355, 873

—. 2002, A&A, 394, 791

Chiaberge, M., Gilli, R., Lotz, J. M., & Norman, C. 2015, ApJ, 806, 147

Cleary, K., Lawrence, C. R., Marshall, J. A., Hao, L., & Meier, D. 2007, ApJ, 660, 117

Condon, J. J., Cotton, W. D., Greisen, E. W., Yin, Q. F., Perley, R. A., Taylor, G. B., & Broderick, J. J. 1998, AJ, 115, 1693

Cooke, B. A., Lawrence, A., & Perola, G. C. 1978, MNRAS, 182, 661

D'Abrusco, R., Álvarez Crespo, N., Massaro, F., Campana, R., Chavushyan, V., Landoni, M., La Franca, F., Masetti, N., Milisavljevic, D., Paggi, A., Ricci, F., & Smith, H. A. 2019, ApJS, 242, 4

D'Abrusco, R., Massaro, F., Paggi, A., Smith, H. A., Masetti, N., Landoni, M., & Tosti, G. 2014, ApJS, 215, 14

Dariush, A., Khosroshahi, H. G., Ponman, T. J., Pearce, F., Raychaudhury, S., & Hartley, W. 2007, MNRAS, 382, 433

Dasadia, S., Sun, M., Morandi, A., Sarazin, C., Clarke, T., Nulsen, P., Massaro, F., Roediger, E., Harris, D., & Forman, B. 2016, MNRAS, 458, 681

Davies, R. L., Schirmer, M., & Turner, J. E. H. 2015, MNRAS, 449, 1731

de Koff, S., Baum, S. A., Sparks, W. B., Biretta, J., Golombek, D., Macchetto, F., McCarthy, P., & Miley, G. K. 1996, ApJS, 107, 621

Dennison, B. 1979, AJ, 84, 725

Edge, D. O., Shakeshaft, J. R., McAdam, W. B., Baldwin, J. E., & Archer, S. 1959, MmRAS, 68, 37

Fabian, A. C. 2012, ARA&A, 50, 455

Fanaroff, B. L. & Riley, J. M. 1974, MNRAS, 167, 31P

Felten, J. E. 1996, in Astronomical Society of the Pacific Conference Series, Vol. 88, Clusters, Lensing, and the Future of the Universe, ed. V. Trimble & A. Reisenegger, 271

Felten, J. E. & Rees, M. J. 1969, Nature, 221, 924

Feretti, L., Dallacasa, D., Giovannini, G., & Tagliani, A. 1995, A&A, 302, 680

Fitzpatrick, E. L. & Massa, D. 2007, ApJ, 663, 320

Ghisellini, G., Celotti, A., Tavecchio, F., Haardt, F., & Sbarrato, T. 2014a, MNRAS, 438, 2694

Ghisellini, G., Haardt, F., Ciardi, B., Sbarrato, T., Gallo, E., Tavecchio, F., & Celotti, A. 2015, MNRAS, 452, 3457

Ghisellini, G., Tavecchio, F., Maraschi, L., Celotti, A., & Sbarrato, T. 2014b, Nature, 515, 376

Glazebrook, K. & Bland-Hawthorn, J. 2001, PASP, 113, 197

Glowacki, M., Allison, J. R., Sadler, E. M., Moss, V. A., & Jarrett, T. H. 2017, arXiv e-prints, arXiv:1709.08634

Govoni, F. & Feretti, L. 2004, International Journal of Modern Physics D, 13, 1549

Govoni, F., Murgia, M., Vacca, V., Loi, F., Girardi, M., Gastaldello, F., Giovannini, G., Feretti, L., Paladino, R., Carretti, E., Concu, R., Melis, A., Poppi, S., Valente, G., Bernardi, G., Bonafede, A., Boschin, W., Brienza, M., Clarke, T. E., Colafrancesco, S., de Gasperin, F., Eckert, D., Enßlin, T. A., Ferrari, C., Gregorini, L., Johnston-Hollitt, M., Junklewitz, H., Orrù, E., Parma, P., Perley, R., Rossetti, M., B Taylor, G., & Vazza, F. 2017, A&A, 603, A122

Grillo, C., Christensen, L., Gallazzi, A., & Rasmussen, J. 2013, MNRAS, 433, 2604

Hardcastle, M. J., Evans, D. A., & Croston, J. H. 2009, MNRAS, 396, 1929

Harris, D. E. & Grindlay, J. E. 1979, MNRAS, 188, 25

Harris, D. E. & Krawczynski, H. 2002, ApJ, 565, 244

Harvanek, M. & Hardcastle, M. J. 1998, ApJS, 119, 25

Heckman, T. M. & Best, P. N. 2014, ARA&A, 52, 589

Hess, K. M., Wilcots, E. M., & Hartwick, V. L. 2012, AJ, 144, 48

HI4PI Collaboration, Ben Bekhti, N., Flöer, L., Keller, R., Kerp, J., Lenz, D., Winkel, B., Bailin, J., Calabretta, M. R., Dedes, L., Ford, H. A., Gibson, B. K., Haud, U., Janowiecki, S., Kalberla, P. M. W., Lockman, F. J., McClure-Griffiths, N. M., Murphy, T., Nakanishi, H., Pisano, D. J., & Staveley-Smith, L. 2016, A&A, 594, A116

Hilbert, B., Chiaberge, M., Kotyla, J. P., Tremblay, G. R., Stanghellini, C., Sparks, W. B., Baum, S., Capetti, A., Macchetto, F. D., Miley, G. K., O'Dea, C. P., Perlman, E. S., & Quillen, A. 2016, ApJS, 225, 12

Hine, R. G. & Longair, M. S. 1979, MNRAS, 188, 111

Hook, I. M., Jørgensen, I., Allington-Smith, J. R., Davies, R. L., Metcalfe, N., Murowinski, R. G., & Crampton, D. 2004, PASP, 116, 425

Jackson, N. & Rawlings, S. 1997, MNRAS, 286, 241

Jaffe, W. & Perola, G. C. 1974, A&A, 31, 223

Jimenez-Gallardo, A., Massaro, F., Balmaverde, B., Paggi, A., Capetti, A., Forman, W. R., Kraft, R. P., Baldi, R. D., Mahatma, V. H., Mazzucchelli, C., Missaglia, V., Ricci, F., Venturi, G., Baum, S. A., Liuzzo, E., O'Dea, C. P., Prieto, M. A., Röttgering, H. J. A., Sani, E., Sparks, W. B., Tremblay, G. R., van Weeren, R. J., Wilkes, B. J., Harwood, J. J., Mazzotta, P., & Kuraszkiewicz, J. 2021a, ApJ, 912, L25

Jimenez-Gallardo, A., Massaro, F., Paggi, A., D'Abrusco, R., Prieto, M. A., Peña-Herazo, H. A., Berta, V., Ricci, F., Stuardi, C., Wilkes, B. J., O'Dea, C. P., Baum, S. A., Kraft, R. P., Forman, W. R., Jones, C., Mingo, B., Liuzzo, E., Balmaverde, B., Capetti, A., Missaglia, V., Hardcastle, M. J., Baldi, R. D., & Morabito, L. K. 2021b, ApJS, 252, 31

Jimenez-Gallardo, A., Massaro, F., Prieto, M. A., Missaglia, V., Stuardi, C., Paggi, A., Ricci, F., Kraft, R. P., Liuzzo, E., Tremblay, G. R., Baum, S. A., O'Dea, C. P., Wilkes, B. J., Kuraszkiewicz, J., Forman, W. R., & Harris, D. E. 2020, ApJS, 250, 7

Johnson, L. E., Irwin, J. A., White, Raymond E., I., Wong, K.-W., & Dupke, R. A. 2018, ApJ, 869, 170

Jones, L. R., Maughan, B. J., Ebeling, H., Scharf, C., Perlman, E., Lumb, D., Gondoin, P., Mason, K. O., Cordova, F., & Priedhorsky, W. C. 2004, in Clusters of Galaxies: Probes of Cosmological Structure and Galaxy Evolution, ed. J. S. Mulchaey, A. Dressler, & A. Oemler, 25

Jones, L. R., Ponman, T. J., Horton, A., Babul, A., Ebeling, H., & Burke, D. J. 2003, MNRAS, 343, 627

Kalberla, P. M. W., Burton, W. B., Hartmann, D., Arnal, E. M., Bajaja, E., Morras, R., & Pöppel, W. G. L. 2005, A&A, 440, 775

Kotyla, J. P., Chiaberge, M., Baum, S., Capetti, A., Hilbert, B., Macchetto, F. D., Miley, G. K., O'Dea, C. P., Perlman, E. S., Sparks, W. B., & Tremblay, G. R. 2016, ApJ, 826, 46

Kraft, R. P., Birkinshaw, M., Nulsen, P. E. J., Worrall, D. M., Croston, J. H., Forman, W. R., Hardcastle, M. J., Jones, C., & Murray, S. S. 2012, ApJ, 749, 19

Kraft, R. P., Forman, W. R., Churazov, E. C., Eilek, J., Hardcastle, M. J., Heinz, S., Jones, C., Markevitch, M., Murray, S. S., Nulsen, P. E. J., Owen, F., Vikhlinin, V., & Worrall, D. M. 2005, in X-Ray and Radio Connections, ed. L. O. Sjouwerman & K. K. Dyer, 7.09

Kundert, A., D'Onghia, E., & Aguerri, J. A. L. 2017, ApJ, 845, 45

Lacy, M., Baum, S. A., Chandler, C. J., Chatterjee, S., Clarke, T. E., Deustua, S., English, J., Farnes, J., Gaensler, B. M., Gugliucci, N., Hallinan, G., Kent, B. R., Kimball, A., Law, C. J., Lazio, T. J. W., Marvil, J., Mao, S. A., Medlin, D., Mooley, K., Murphy, E. J., Myers, S., Osten, R., Richards, G. T., Rosolowsky, E., Rudnick, L., Schinzel, F., Sivakoff, G. R., Sjouwerman, L. O., Taylor, R., White, R. L., Wrobel, J., Andernach, H., Beasley, A. J., Berger, E., Bhatnager, S., Birkinshaw, M., Bower, G. C., Brandt, W. N., Brown, S., Burke-Spolaor, S., Butler, B. J., Comerford, J., Demorest, P. B., Fu, H., Giacintucci, S., Golap, K., Güth, T., Hales, C. A., Hiriart, R., Hodge, J., Horesh, A., Ivezić, Ž., Jarvis, M. J., Kamble, A., Kassim, N., Liu, X., Loinard, L., Lyons, D. K., Masters, J., Mezcua, M., Moellenbrock, G. A., Mroczkowski, T., Nyland, K., O'Dea, C. P., O'Sullivan, S. P., Peters, W. M., Radford, K., Rao, U., Robnett, J., Salcido, J., Shen, Y., Sobotka, A., Witz, S., Vaccari, M., van Weeren, R. J., Vargas, A., Williams, P. K. G., & Yoon, I. 2020, PASP, 132, 035001

Laing, R. A., Bridle, A. H., Parma, P., & Murgia, M. 2008, MNRAS, 391, 521

Laing, R. A., Jenkins, C. R., Wall, J. V., & Unger, S. W. 1994, in Astronomical Society of the Pacific Conference Series, Vol. 54, The Physics of Active Galaxies, ed. G. V. Bicknell, M. A. Dopita, & P. J. Quinn, 201

Laing, R. A., Riley, J. M., & Longair, M. S. 1983, MNRAS, 204, 151

Lane, W. M., Cotton, W. D., van Velzen, S., Clarke, T. E., Kassim, N. E., Helmboldt, J. F., Lazio, T. J. W., & Cohen, A. S. 2014, MNRAS, 440, 327

Law-Green, J. D. B., Leahy, J. P., Alexander, P., Allington-Smith, J. R., van Breugel, W. J. M., Eales, S. A., Rawlings, S. G., & Spinrad, H. 1995, MNRAS, 274, 939

Lawler, J. M. & Dennison, B. 1982, ApJ, 252, 81

Lotz, J. M., Jonsson, P., Cox, T. J., & Primack, J. R. 2008, MNRAS, 391, 1137

Lynds, C. R., Stockton, A. N., & Livingston, W. C. 1965, ApJ, 142, 1667

Madrid, J. P., Chiaberge, M., Floyd, D., Sparks, W. B., Macchetto, D., Miley, G. K., Axon, D., Capetti, A., O'Dea, C. P., Baum, S., Perlman, E., & Quillen, A. 2006, ApJS, 164, 307

Madrid, J. P., Donzelli, C. J., Rodríguez-Ardila, A., Paggi, A., Massaro, F., & Schirmer, M. 2018, ApJS, 238, 31

Makarov, D. I. & Uklein, R. I. 2012, Astrophysical Bulletin, 67, 135

Maselli, A., Massaro, F., Cusumano, G., La Parola, V., Harris, D. E., Paggi, A., Liuzzo, E., Tremblay, G. R., Baum, S. A., & O'Dea, C. P. 2016, MNRAS, 460, 3829

Massaro, F. & Ajello, M. 2011a, ApJ, 729, L12

—. 2011b, ApJ, 729, L12

Massaro, F., Capetti, A., Paggi, A., Baldi, R. D., Tramacere, A., Pillitteri, I., Campana, R., Jimenez-Gallardo, A., & Missaglia, V. 2020, ApJS, 247, 71

Massaro, F., Harris, D. E., & Cheung, C. C. 2011, ApJS, 197, 24

Massaro, F., Harris, D. E., Chiaberge, M., Grandi, P., Macchetto, F. D., Baum, S. A., O'Dea, C. P., & Capetti, A. 2009, ApJ, 696, 980

Massaro, F., Harris, D. E., Liuzzo, E., Orienti, M., Paladino, R., Paggi, A., Tremblay, G. R., Wilkes, B. J., Kuraszkiewicz, J., Baum, S. A., & O'Dea, C. P. 2015, ApJS, 220, 5

Massaro, F., Harris, D. E., Tremblay, G. R., Axon, D., Baum, S. A., Capetti, A., Chiaberge, M., Gilli, R., Giovannini, G., Grandi, P., Macchetto, F. D., O'Dea, C. P., Risaliti, G., & Sparks, W. 2010, ApJ, 714, 589

Massaro, F., Harris, D. E., Tremblay, G. R., Liuzzo, E., Bonafede, A., & Paggi, A. 2013, ApJS, 206, 7

Massaro, F., Missaglia, V., Stuardi, C., Harris, D. E., Kraft, R. P., Paggi, A., Liuzzo, E., Tremblay, G. R., Baum, S. A., O'Dea, C. P., Wilkes, B. J., Kuraszkiewicz, J., & Forman, W. R. 2018, ApJS, 234, 7

Massaro, F., Tremblay, G. R., Harris, D. E., Kharb, P., Axon, D., Balmaverde, B., Baum, S. A., Capetti, A., Chiaberge, M., Gilli, R., Giovannini, G., Grandi, P., Macchetto, F. D., O'Dea, C. P., Risaliti, G., Sparks, W., & Torresi, E. 2012, ApJS, 203, 31

McCarthy, P. J., Miley, G. K., de Koff, S., Baum, S. A., Sparks, W. B., Golombek, D., Biretta, J., & Macchetto, F. 1997, ApJS, 112, 415

Melis, A., Concu, R., Trois, A., Possenti, A., Bocchinu, A., Bolli, P., Burgay, M., Carretti, E., Castangia, P., Casu, S., Pestellini, C. C., Corongiu, A., D'Amico, N., Egron, E., Govoni, F., Iacolina, M. N., Murgia, M., Pellizzoni, A., Perrodin, D., Pilia, M., Pisanu, T., Poddighe, A., Poppi, S., Porceddu, I., Tarchi, A., Vacca, V., Aresu, G., Bachetti, M., Barbaro, M., Casula, A., Ladu, A., Leurini, S., Loi, F., Loru, S., Marongiu, P., Maxia, P., Mazzarella, G., Migoni, C., Montisci, G., Valente, G., & Vargiu, G. 2018, Journal of Astronomical Instrumentation, 7, 1850004

Mendes de Oliveira, C. L. & Carrasco, E. R. 2007, ApJ, 670, L93

Messias, H. G., Hatziminaoglou, E., Hibon, P., Mroczkowski, T., Matute, I., Lacy, M., Mason, B., Martín, S., Afonso, J. M., Fomalont, E., Amarantidis, S., Antón, S., Cortés, P. C., Demarco, R., Gendron-Marsolais, M.-L., Hopkins, A. M., Kneissl, R., Lopez, C., Rebolledo, D., & Yang, C. 2021, MNRAS, 508, 5259

Mingo, B., Croston, J. H., Hardcastle, M. J., Best, P. N., Duncan, K. J., Morganti, R., Rottgering, H. J. A., Sabater, J., Shimwell, T. W., Williams, W. L., Brienza, M., Gurkan, G., Mahatma, V. H., Morabito, L. K., Prandoni, I., Bondi, M., Ineson, J., & Mooney, S. 2019, MNRAS, 488, 2701

Minkowski, R. 1960, ApJ, 132, 908

Missaglia, V., Madrid, J. P., Schirmer, M., Massaro, F., Rodríguez-Ardila, A., Donzelli, C. J., Valencia, M., Paggi, A., Kraft, R. P., Stuardi, C., & Wilkes, B. J. 2023, ApJS, 264, 6

Missaglia, V., Massaro, F., Liuzzo, E., Paggi, A., Kraft, R. P., Forman, W. R., Jimenez-Gallardo, A., Madrid, J. P., Ricci, F., Stuardi, C., Wilkes, B. J., Baum, S. A., O'Dea, C. P., Kuraszkiewicz, J., Tremblay, G. R., Maselli, A., Capetti, A., Sani, E., Balmaverde, B., & Harris, D. E. 2021, ApJS, 255, 18

Missaglia, V., Murgia, M., Massaro, F., Paggi, A., Jimenez-Gallardo, A., Forman, W. R., Kraft, R. P., & Balmaverde, B. 2022, ApJ, 936, 10

Morganti, R., Oosterloo, T., Tadhunter, C. N., Aiudi, R., Jones, P., & Villar-Martin, M. 1999, A&AS, 140, 355

Murgia, M., Fanti, C., Fanti, R., Gregorini, L., Klein, U., Mack, K. H., & Vigotti, M. 1999, A&A, 345, 769

Murgia, M., Govoni, F., Feretti, L., Giovannini, G., Dallacasa, D., Fanti, R., Taylor, G. B., & Dolag, K. 2004, A&A, 424, 429

Murgia, M., Markevitch, M., Govoni, F., Parma, P., Fanti, R., de Ruiter, H. R., & Mack, K. H. 2012, A&A, 548, A75

Murgia, M., Parma, P., Mack, K. H., de Ruiter, H. R., Fanti, R., Govoni, F., Tarchi, A., Giacintucci, S., & Markevitch, M. 2011, A&A, 526, A148

Oke, J. B. & Gunn, J. E. 1983, ApJ, 266, 713

Osterbrock, D. E. & Ferland, G. J. 2006, Astrophysics of gaseous nebulae and active galactic nuclei

Pacholczyk, A. G. 1970, Radio astrophysics. Nonthermal processes in galactic and extragalactic sources

Paggi, A., Massaro, F., Peña-Herazo, H. A., Missaglia, V., Ricci, F., Stuardi, C., Kraft, R. P., Tremblay, G. R., Baum, S. A., & Wilkes, B. J. 2021, A&A, 647, A79

Parma, P., Murgia, M., Morganti, R., Capetti, A., de Ruiter, H. R., & Fanti, R. 1999, A&A, 344, 7

Perna, M., Brusa, M., Cresci, G., Comastri, A., Lanzuisi, G., Lusso, E., Marconi, A., Salvato, M., Zamorani, G., Bongiorno, A., Mainieri, V., Maiolino, R., & Mignoli, M. 2015, A&A, 574, A82

Podigachoski, P., Barthel, P. D., Haas, M., Leipski, C., Wilkes, B., Kuraszkiewicz, J., Westhues, C., Willner, S. P., Ashby, M. L. N., Chini, R., Clements, D. L., Fazio, G. G., Labiano, A., Lawrence, C., Meisenheimer, K., Peletier, R. F., Siebenmorgen, R., & Verdoes Kleijn, G. 2015, A&A, 575, A80

Ponman, T. J., Allan, D. J., Jones, L. R., Merrifield, M., McHardy, I. M., Lehto, H. J., & Luppino, G. A. 1994, Nature, 369, 462

Pracy, M. B., Ching, J. H. Y., Sadler, E. M., Croom, S. M., Baldry, I. K., Bland-Hawthorn, J., Brough, S., Brown, M. J. I., Couch, W. J., Davis, T. M., Drinkwater, M. J., Hopkins,

A. M., Jarvis, M. J., Jelliffe, B., Jurek, R. J., Loveday, J., Pimbblet, K. A., Prescott, M., Wisnioski, E., & Woods, D. 2016, MNRAS, 460, 2

Prandoni, I., Murgia, M., Tarchi, A., Burgay, M., Castangia, P., Egron, E., Govoni, F., Pellizzoni, A., Ricci, R., Righini, S., Bartolini, M., Casu, S., Corongiu, A., Iacolina, M. N., Melis, A., Nasir, F. T., Orlati, A., Perrodin, D., Poppi, S., Trois, A., Vacca, V., Zanichelli, A., Bachetti, M., Buttu, M., Comoretto, G., Concu, R., Fara, A., Gaudiomonte, F., Loi, F., Migoni, C., Orfei, A., Pilia, M., Bolli, P., Carretti, E., D'Amico, N., Guidetti, D., Loru, S., Massi, F., Pisanu, T., Porceddu, I., Ridolfi, A., Serra, G., Stanghellini, C., Tiburzi, C., Tingay, S., & Valente, G. 2017, A&A, 608, A40

Pratt, G. W., Pointecouteau, E., Arnaud, M., & van der Burg, R. F. J. 2016, A&A, 590, L1

Rees, M. J. & Sciama, D. W. 1968, Nature, 217, 511

Ricci, F., Lovisari, L., Kraft, R. P., Massaro, F., Paggi, A., Liuzzo, E., Tremblay, G., Forman, W. R., Baum, S., O'Dea, C., & Wilkes, B. 2018, ApJ, 867, 35

Sandage, A. 1966, ApJ, 145, 1

—. 1967, ApJ, 150, L145

Schirmer, M., Suyu, S., Schrabback, T., Hildebrandt, H., Erben, T., & Halkola, A. 2010, A&A, 514, A60

Schlafly, E. F. & Finkbeiner, D. P. 2011a, ApJ, 737, 103

—. 2011b, ApJ, 737, 103

Smith, H. E. & Spinrad, H. 1980, PASP, 92, 553

Smith, H. E., Spinrad, H., & Smith, E. O. 1976, PASP, 88, 621

Spinrad, H., Djorgovski, S., Marr, J., & Aguilar, L. 1985, PASP, 97, 932

Staveley-Smith, L., Davies, R. D., & Kinman, T. D. 1992, MNRAS, 258, 334

Stuardi, C., Missaglia, V., Massaro, F., Ricci, F., Liuzzo, E., Paggi, A., Kraft, R. P., Tremblay, G. R., Baum, S. A., O'Dea, C. P., Wilkes, B. J., Kuraszkiewicz, J., Forman, W. R., & Harris, D. E. 2018, ApJS, 235, 32

Sunyaev, R. A. & Zeldovich, Y. B. 1972, Comments on Astrophysics and Space Physics, 4, 173

Tremblay, G. R., Chiaberge, M., Sparks, W. B., Baum, S. A., Allen, M. G., Axon, D. J., Capetti, A., Floyd, D. J. E., Macchetto, F. D., Miley, G. K., Noel-Storr, J., O'Dea, C. P., Perlman, E. S., & Quillen, A. C. 2009, ApJS, 183, 278

Tribble, P. C. 1991, MNRAS, 250, 726

Voevodkin, A., Borozdin, K., Heitmann, K., Habib, S., Vikhlinin, A., Mescheryakov, A., Hornstrup, A., & Burenin, R. 2010, ApJ, 708, 1376

Volonteri, M., Haardt, F., Ghisellini, G., & Della Ceca, R. 2011, MNRAS, 416, 216

Wayth, R. B., Lenc, E., Bell, M. E., Callingham, J. R., Dwarakanath, K. S., Franzen, T. M. O., For, B. Q., Gaensler, B., Hancock, P., Hindson, L., Hurley-Walker, N., Jackson, C. A., Johnston-Hollitt, M., Kapińska, A. D., McKinley, B., Morgan, J., Offringa, A. R., Procopio, P., Staveley-Smith, L., Wu, C., Zheng, Q., Trott, C. M., Bernardi, G., Bowman, J. D., Briggs, F., Cappallo, R. J., Corey, B. E., Deshpande, A. A., Emrich, D., Goeke, R., Greenhill, L. J., Hazelton, B. J., Kaplan, D. L., Kasper, J. C., Kratzenberg, E., Lonsdale, C. J., Lynch, M. J., McWhirter, S. R., Mitchell, D. A., Morales, M. F., Morgan, E., Oberoi, D., Ord, S. M., Prabu, T., Rogers, A. E. E., Roshi, A., Shankar, N. U., Srivani, K. S., Subrahmanyan, R., Tingay, S. J., Waterson, M., Webster, R. L., Whitney, A. R., Williams, A., & Williams, C. L. 2015, PASA, 32, e025

Wright, E. L., Eisenhardt, P. R. M., Mainzer, A. K., Ressler, M. E., Cutri, R. M., Jarrett, T., Kirkpatrick, J. D., Padgett, D., McMillan, R. S., Skrutskie, M., Stanford, S. A.,

Cohen, M., Walker, R. G., Mather, J. C., Leisawitz, D., Gautier, Thomas N., I., McLean, I., Benford, D., Lonsdale, C. J., Blain, A., Mendez, B., Irace, W. R., Duval, V., Liu, F., Royer, D., Heinrichsen, I., Howard, J., Shannon, M., Kendall, M., Walsh, A. L., Larsen, M., Cardon, J. G., Schick, S., Schwalm, M., Abid, M., Fabinsky, B., Naes, L., & Tsai, C.-W. 2010, AJ, 140, 1868

Yoo, J., Ko, J., Kim, J.-W., & Kim, H. 2021, MNRAS, 508, 2634

Yuan, W., Fabian, A. C., Celotti, A., & Jonker, P. G. 2003, MNRAS, 346, L7

Zakamska, N. L. & Greene, J. E. 2014, MNRAS, 442, 784

Chapter 4

Beyond the Third Cambridge Catalog

Part of my Ph.D. work has been devoted to a peculiar class of radio sources: the wide angle tailed radio galaxies (WATs). Observed for the first time with the National Radio Astronomy Observatory (NRAO) interferometer at 2.7 GHz during a survey of sources in the Abell clusters (Owen & Rudnick 1976), WATs were given this name because their radio morphology presents the so-called "jet-hotspot-lobe transition": there are bright hotspots (called "warmspots") closer to their radio core with respect to FR IIs and with extended radio plumes beyond them (O'Donoghue et al. 1990). Leahy (1993) defines WATs as a class of sources that initially have well-collimated jets on a kiloparsec scale and that suddenly flare into diffuse plumes, which may be significantly bent.

Owen & Rudnick (1976), noting that this source class has higher radio luminosity than the radio sources with narrower tails (also known as head-tailed radio galaxies), proposed that their curved radio structure could be due to the motion of the host galaxy through the ICM, moving more slowly than the head-tailed sources. This scenario is supported by the fact that WATs are generally associated with more dominant cluster galaxies (Bird 1994; Pinkney 1995).

Sakelliou & Merrifield (2000) investigated WATs radio structure using a sample selected from those lying in Abell galaxy clusters. These authors suggested that because the Universe evolves hierarchically with galaxy clusters forming through mergers of groups, WATs bent or curved tails are due to the ram pressure that originated in the merging processes.

4.1 WATs Large Scale Environment at $z \lesssim 0.15$

In this section I present a statistical analysis of the large-scale (up to 2 Mpc) environment of an homogeneous and complete sample, both in radio and optical selection, of WATs in the local Universe (i.e., with redshifts $z \lesssim 0.15$). The analysis is carried out using the parameters obtainable from the cosmological neighbors, that is optical sources within a distance of maximum 2 Mpc from the target source. I have compared the results on WATs large-scale environments with that of FR Is and FR IIs radio galaxies, listed in two others homogeneous and complete catalogs, and selected with the same criterion adopted for the WATs catalog.

WATs are normally found in galaxy cluster and are in general associated with the brightest cluster galaxy (BCG; see e.g. Burns 1981). This implies that WATs can be found in merging systems, as shown in Gómez et al. (1997) via *ROSAT* X-ray data, or relaxed systems showing "sloshing" of the central ICM due to cluster minor mergers (Ascasibar & Markevitch 2006). WATs have proven to be reliable tracers of high-density environments up to high redshifts and may be therefore used as probes of the presence of the ICM. One of the first examples is that presented by Burns (1981). The author presented VLA 20-cm observations of the WAT 1919+479 (4C 47.51), discussing the morphology, the polarization, the environment and the nature of the galaxy cluster hosting the radio source. Using X-ray observations, it is possible to support the contention that the cluster around the WAT is gas rich.

Many different methods have been already used to investigate the large-scale environment of radio sources. Thanks to multifrequency observations and redshift estimates, it has been possible to remove unrelated galaxies and so improving the reliability of the analysis (Best 2004). In the optical range, the Sloan Digital Sky Survey (SDSS, York et al. 2000) has expanded our knowledge of galaxy properties, such as luminosities, morphologies, star-formation rates and nuclear activity, and how this properties depend upon the environment that a galaxy inhabits. This can place important constraints on

models of galaxy formation and evolution, and allows the intrinsic properties of the galaxies to be separated from those that have been externally induced.

Studying the environment of FR Is and FR IIs on the megaparsec scale, it was found that FR Is generally inhabit galaxy-rich environments, being members of groups or galaxy clusters, while FR IIs tend to be more isolated as shown, for example, in Zirbel (1997). There are however some well known exceptions, such as Cygnus A (Carilli & Barthel 1996).

The environments of powerful radio sources have been widely studied (see e.g., Prestage & Peacock 1988; Hill & Lilly 1991) up to a $z \sim 0.5$. From the estimate of the galaxy density around these sources, it has been concluded that there is no strong statistical evidence for the difference in the environments hosting FR Is and FR IIs, but at low-redshift ($z < 0.5$) the environments appear less galaxy-rich than that of the counterparts of same radio power at high-redshift.

In the literature WATs environment has been studied both at moderate ($z \sim 0.2$) and high redshift ($z > 0.2$). Blanton et al. (2001) presented observations of a complete, magnitude-limited sample of 40 radio galaxies from the VLA FIRST survey (Becker et al. 1995), part of a larger sample of bent-double radio sources at moderate redshift. The most interesting result is that ~46% of the sources in the sample are associated with groups, some of them being poor groups. The high-redshift Clusters Occupied by Bent Radio AGN (COBRA) Survey (Blanton et al. 2015) uses bent radio sources as tracers of distant galaxy clusters, on the assumption that, as shown at low-redshift, WATs are good tracers of high-density environments.

Smolčić et al. (2007), having identified a complex galaxy cluster system in the COSMOS field via a WAT, used optical and X-ray data to investigate its host environment. The cluster shows evidence for subclustering, both in diffuse X-ray emission and in the spatial distribution of galaxies found from the optical analysis applying the Voronoi tessellation-based approach.

In this work, extending the previous analysis of the large-scale environment to a complete and homogeneous (both in luminosity and redshift) sample of WATs restricted to the local

Universe (i.e., source redshifts z_{src} ≤0.15) it is possible to prove if WATs environment differs from that of FR Is and FR IIs from the catalogs FRI*CAT* and FRII*CAT*. WATs used in this work are listed in the WAT*CAT* (Missaglia et al. 2019, details of the catalogs are described in Section 4.1.1). A similar analysis is reported in Massaro et al. (2019) in which the authors presented the results of the analysis of the large-scale environment of FR I and FR II radio galaxies from the same catalogs I use in this work. From their analysis, Massaro et al. (2019) concluded that radio galaxies, independently of their radio (FR I vs. FR II) classification, tend to inhabit galaxy-rich large-scale environments with similar richness.

Hereinafter, cgs units are adopted for numerical results and a flat cosmology with H_0=69.6 km s^{-1} Mpc^{-1}, $\Omega_{\rm M}$=0.286 and Ω_Λ=0.714 (Bennett et al. 2014) is assumed, unless otherwise stated. Thus, according to these cosmological parameters, in the z range of the WAT*CAT* , 1″ corresponds to 0.408 kpc at $z_{\rm src}$=0.02 and to 2.634 kpc at $z_{\rm src}$=0.15.

4.1.1 Sample Selection

To carry out this analysis I have used three catalogs, all obtained from the radio-loud sample of Best & Heckman (2012). All sources are selected on the basis of their morphology, as it is shown in the Faint Images of the Radio Sky at Twenty cm (FIRST) radio survey (Becker et al. 1995).

The first catalog is the WAT*CAT* (Missaglia et al. 2019), listing 47 radio sources at low redshift ($z_{\rm src}$ ≤ 0.15) showing two-sided jets with two clear warmspots (i.e., jet knots as bright as 20% of the nucleus) lying on the opposite side of the radio core and having classical extended emission resembling a plume beyond the warmspots.

The second catalog is the combination of FRI*CAT* and sFRI*CAT* both described in Capetti et al. (2017a). FRI*CAT* sources, chosen on the basis of their FR I radio morphology, are selected to have a radio structure extending beyond a distance of 30 kpc from the optical position of the host galaxy. The 14 sFRI*CAT* sources have FR I radio morphology, whose radio emission extended between 10 and 30 kpc, and are limited to z_{src} =0.05 (see Capetti

et al. 2017a, for details). The combination of these two samples includes FR Is at redshift $z_{src} \leq 0.15$.

The third catalog is the FRII*CAT* (Capetti et al. 2017b), composed of 105 edge-brightened radio sources (FR II type) within the same redshift range of the previous catalog.

All three catalogs include only sources lying in the footprint of the SDSS, that is also covered by the main catalog of groups and clusters of galaxies adopted in our analysis: the one created by Tempel et al. (2012), based on a modified version of the Friends-of-Friends algorithm (Huchra & Geller 1982; Tago et al. 2010). The Tempel catalog has the largest number of galaxy cluster/group detections, with spectroscopic redshifts $0.009 \leq z_{\rm cl} \leq 0.20$, with a peak around 0.08.

It is important to stress that, thanks to the adopted selection criteria, all three radio galaxy catalogs are not contaminated by compact radio objects, as compact steep spectrum sources, and FR 0s (Baldi et al. 2015, 2018), which show a different cosmological evolution and lie in different environments.

4.1.2 Cosmological Neighbors

To investigate the large-scale environment of WATs, first a type of optical sources has been defined: the *cosmological neighbors*.

Cosmological neighbors are all optical sources lying within a maximum distance of 2 Mpc radius computed at $z_{\rm src}$ of the central radio galaxy, with all the SDSS magnitude flags indicating a galaxy-type object (i.e., $uc{=}rc{=}gc{=}ic{=}zc{=}3$), and having a spectroscopic redshift z with $\Delta z = |z_{\rm src} - z| \leq 0.005$. This value corresponds to $\sim$ 1500 km s^{-1}, that is the maximum velocity dispersion in groups and clusters of galaxies (see e.g., Berlind et al. 2006). However, in the galaxy-richest clusters, the large velocity dispersions may lead this method to underestimate the local galaxy density, due to some companion galaxies falling outside of this range.

N_{cn}^{500} and N_{cn}^{2000} are the number of cosmological neighbors lying within 500 kpc and 2 Mpc distance from the central radio galaxy, respectively, that provide an estimate of the environmental richness.

As shown in Figure 4.1, it is quite evident that the N_{gal} parameter (cluster richness from Tempel et al. 2012) underestimates the group/cluster richness, and there are only a few cases in which N_{cn}^{2000} provides a lower estimate of the group/cluster richness.

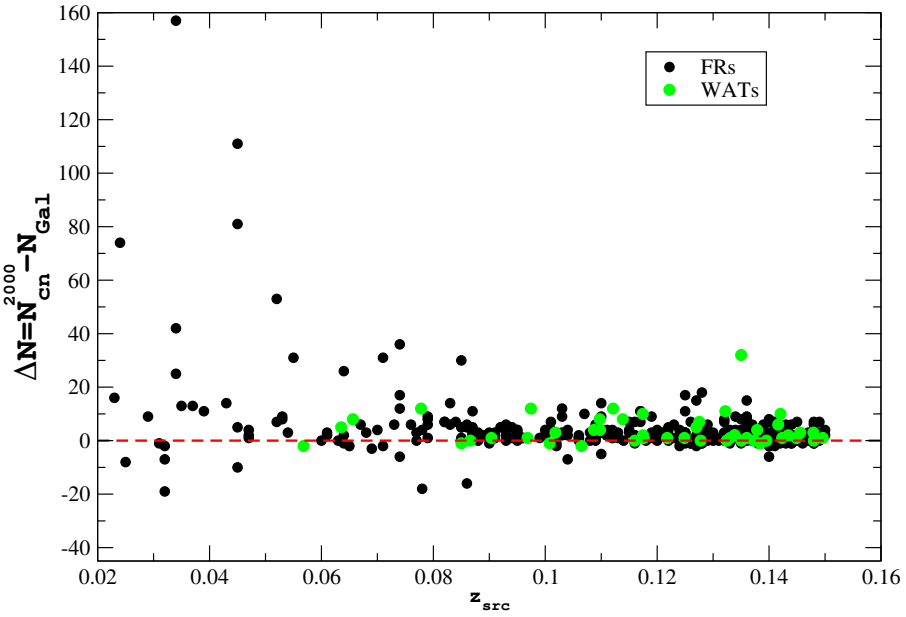

Figure 4.1 The difference ΔN between the number of cosmological neighbors lying within 2 Mpc distance from the central radio source (N_{cn}^{2000}), and the richness estimated in the T12 cluster catalog (N_{gal}) as function of z_{src}. Grey circles mark radio sources in the FRI*CAT* , sFRI*CAT* and FRII*CAT* , and green diamonds correspond to WAT*CAT* sources.

Parameters Definitions

Using the distribution of the cosmological neighbors it is possible to define several parameters that can be used to investigate the properties of the large-scale environments

of WATs and FR Is and FR IIs (hereinafter FRs). Therefore, the following quantities can be defined:

- The *average projected distance* d_{cn}^{m} that is average distance of the distribution of cosmological neighbors within 2 Mpc from the central radio source.
- The *standard deviation* σ_z of the redshift distribution of the cosmological neighbors surrounding each radio source within 2 Mpc.
- The *concentration parameter* ζ_{cn}, defined as the ratio between the number of cosmological neighbors lying within 500 kpc and within 1 Mpc. Under the assumption that the cosmological neighbours are uniformly distributed around the radio galaxy of interest (given that the number of sources around a random position in the sky scales as $N \propto \vartheta^2$, where ϑ is the angular separation from the selected position) the value of ζ_{cn} should be equal to 0.25. This parameter is used to test if the radio galaxy analyzed tends to lie close to the center or in the outskirt of the group or clusters of galaxies in which it resides, if present.

All values of the environmental parameters for the WAT sample described above are reported in Table 4.1.

4.1.3 Statistical Analysis

In this section I present the results obtained from the statistical analysis of WATs large scale environment by means of the environmental parameters previously defined, also searching for possible differences between WATs and FRs properties.

In Figure 4.2, medians of the number of cosmological neighbors within 500 kpc and 2 Mpc from the central WAT are plotted.

Median values for the WAT sample are systematically higher than that of radio galaxies (FR Is and FR IIs). Expecting that medians for the WAT sample are distributed randomly, and therefore there is the same probability of finding medians values for WATs higher or lower than FRs one, according to the binomial distribution the probability that WATs'

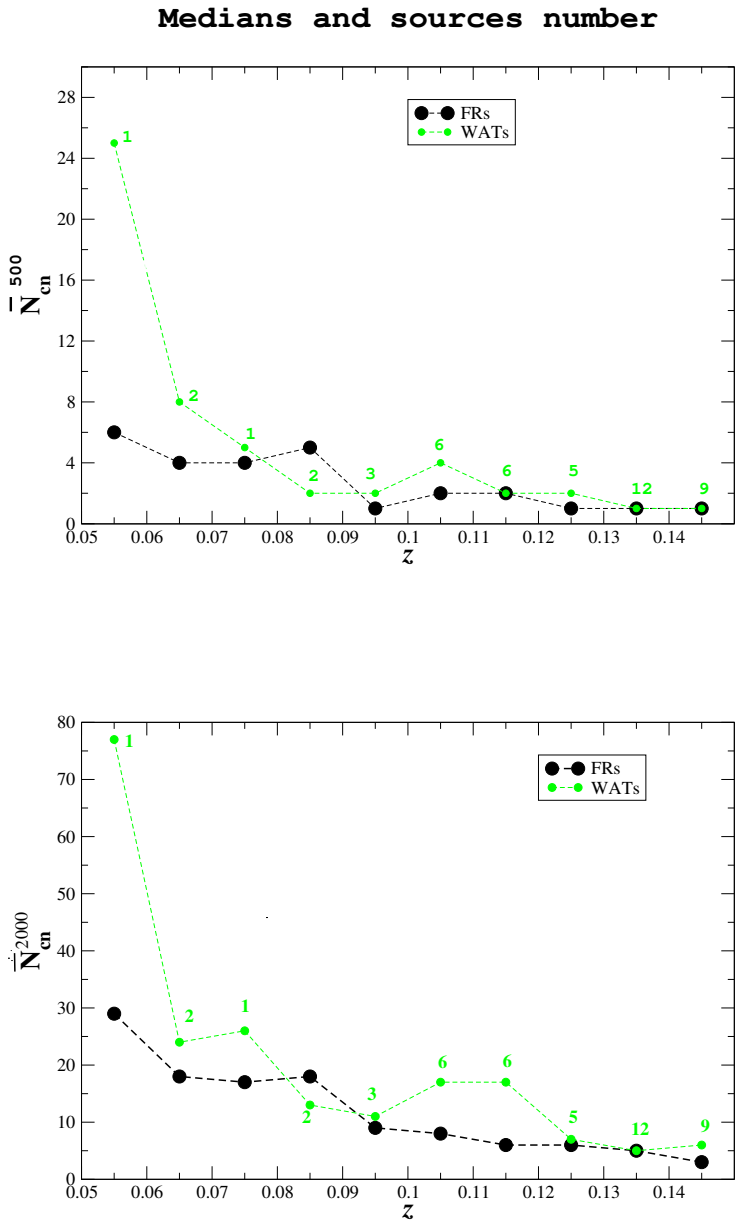

Figure 4.2 Median values of the number of cosmological neighbors for the WATs (green) and the FRs (black) within 500 kpc (*upper panel*) and 2 Mpc (*lower panel*) per bin of redshift z. Above each median value the number of sources in each bin of z starting from 0.05 is also reported.

N_{cn}^{500} are less than FRs' N_{cn}^{500} is ~ 0.4% and that WATs' N_{cn}^{2000} are less than FRs' N_{cn}^{2000} is ~ 2%. Therefore there are some indications that WATs live in richer environments with respect to FRs, but given the small sample of WATs the significance is too low to draw firm conclusions, even if richer environments would be expected, given that WATs morphology is due to merger effects.

Then I explored the distribution of the average projected distance d_{cn}^{m} of cosmological neighbors, which provides an estimate of the galaxy group/cluster physical size, as a function of the standard deviation σ_z of their redshifts (see Figure 4.3 upper panel) and as a function of the redshift of the central source z_{src} (see Figure 4.3 lower panel). In the upper panel Figure 4.3, the standard deviation σ_z of cosmological neighbors' redshifts do not exceed a value of 0.003, that is consistent with the threshold of $\Delta z = |z_{\rm src} - z| \leq 0.005$ used to select the cosmological neighbors, while in the lower panel all the sources in the WAT*CAT* are clustered around a value of d_{cn}^{m} ~ 1 Mpc, implying that the size of the galaxy cluster/group in which the WAT is hosted is constant at low-z, and there are no values of d_{cn}^{m} larger than 1.2 Mpc. The observed scatter at high-z is due to the low number of cosmological neighbors detected. The same results are reported as normalized distributions in Figure 4.4.

In Figure 4.5, the distribution of the concentration parameter ζ_{cn} for WAT*CAT* and FRs sources is shown. Assuming that the cosmological neighbors are uniformly distributed around the radio galaxy analyzed, ζ_{cn}= 0.25. Instead, the majority of the WAT*CAT* sources (41 out of 47) have a value of ζ_{cn} higher than 0.25. This means that WATs tend to occupy the central region of the galaxy group/cluster in which they reside, in agreement with WATs being the BCGs. However, the lack of X-ray observation prevented me to compare the ICM morphology with the spatial distribution of the cosmological neighbors.

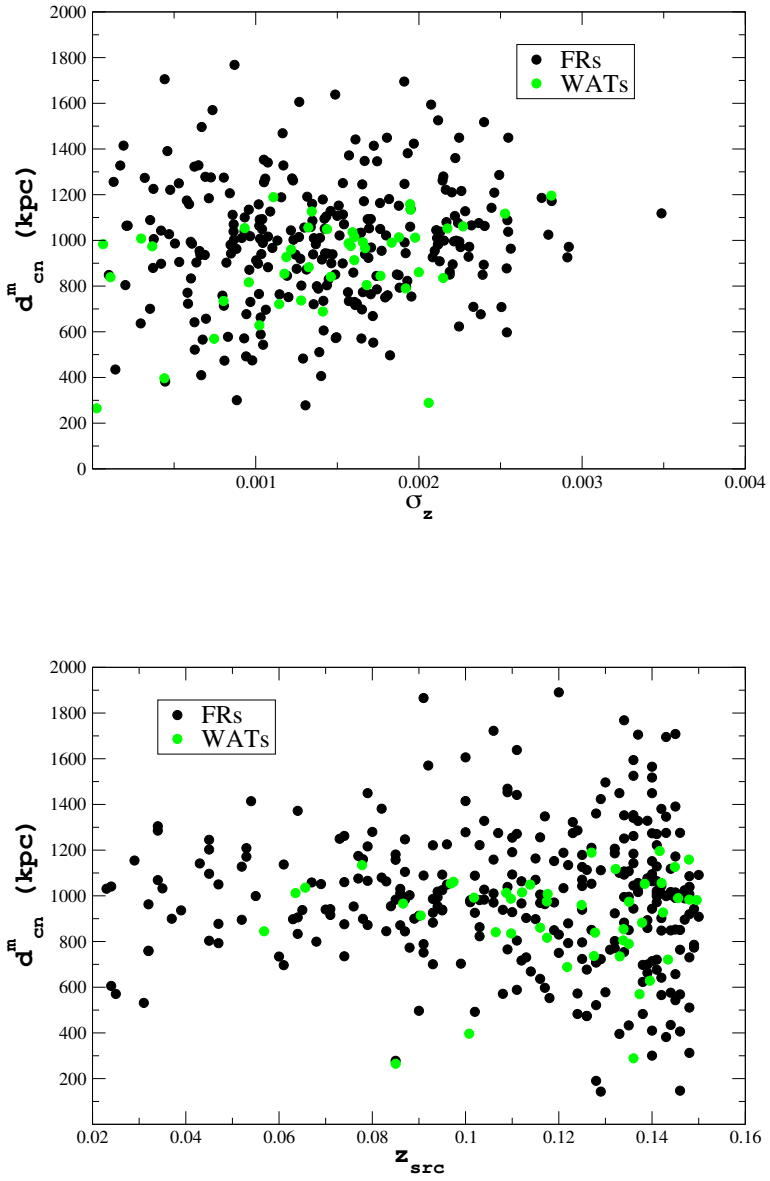

Figure 4.3 Average projected distance d^m_{cn} of the distribution of cosmological neighbors as function of the standard deviation σ_z of their redshift distribution (*upper panel*) and of the redshift z_{src} of the central RG (*lower panel*) for the three RG classes: FR Is and FR IIs (black squares) and WATs (green squares). WAT*CAT* sources are clustered around a certain value of d^m_{cn} ($\sim$ 1 Mpc).

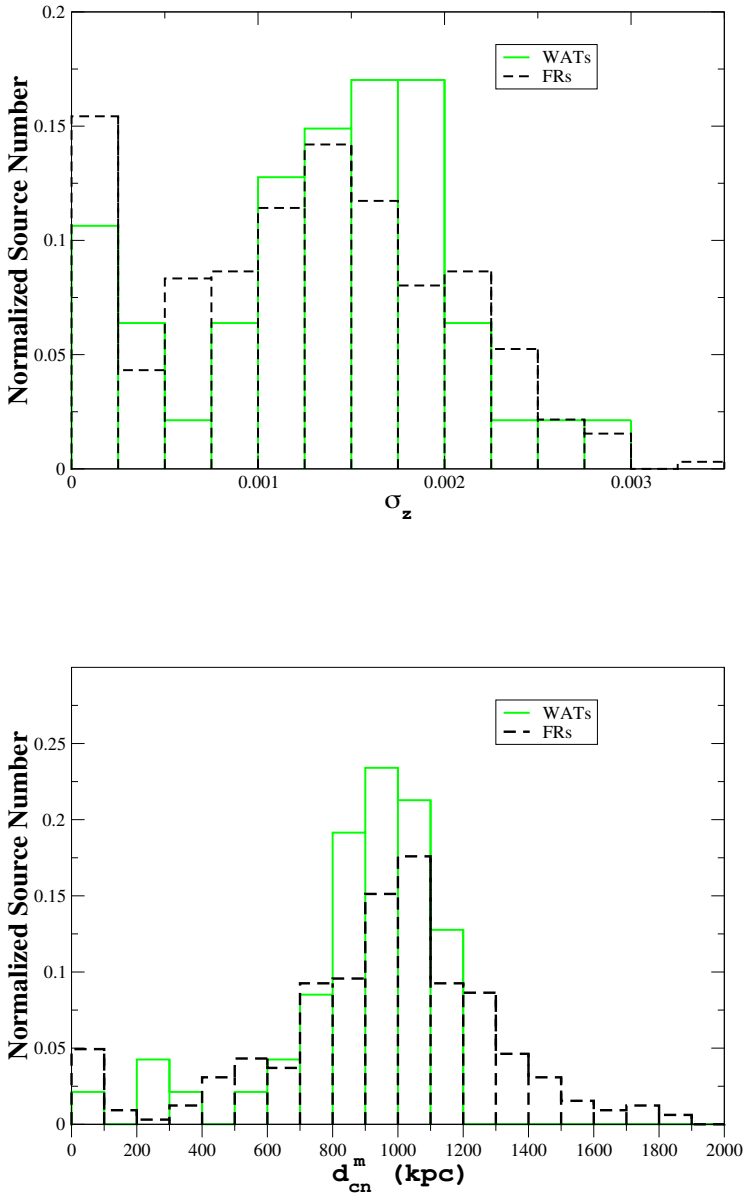

Figure 4.4 Distribution of the standard deviation σ_z of their redshift distribution (*upper panel*) and of the average projected distance d_{cn}^{m} of the distribution of cosmological neighbors (*lower panel*).

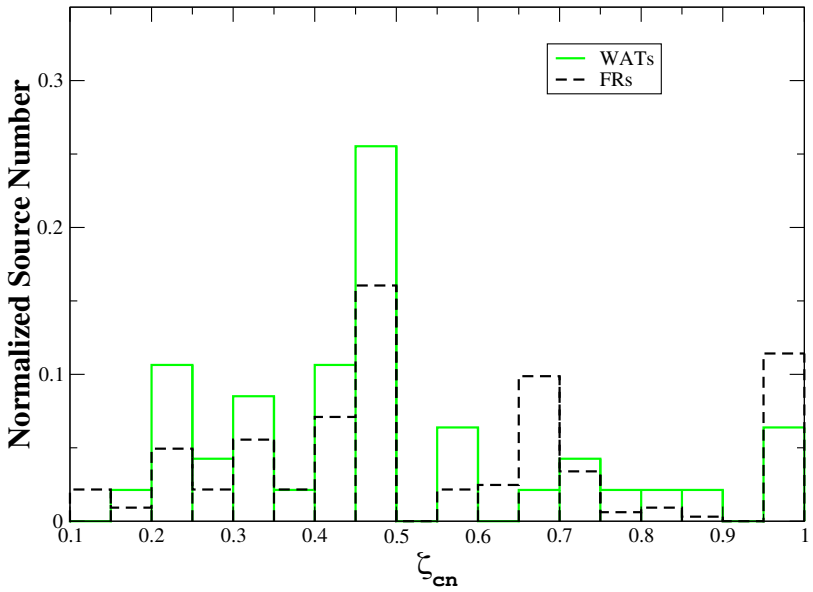

Figure 4.5 The distribution of the concentration parameter ζ_{cn} estimated using the distribution of the cosmological neighbors. Black histogram refers to the FR I and FR II populations, and green one to WATs. The largest fraction of their values lie above the value of 0.25 expected assuming a uniform distribution of cosmological neighbors.

4.1.4 Conclusions

In this Section I presented an extensive investigation of WATs large-scale environment in the local Universe (i.e., at $z_{src} \leq 0.15$). This analysis made use of cosmological neighbors, defined as optical sources lying within 2 Mpc from the radio galaxy of interest, and with a redshift difference $\Delta z \leq 0.005$ with respect to the radio galaxy lying at the center of the field examined. In this study I also compared the large-scale environments of those radio galaxies classified as WATs with that of FR Is and FR IIs, all selected from extremely homogeneous catalogs, with uniform radio, infrared and optical data available for all sources. For FR Is and FR IIs it has been found that, independently of their radio morphological classification, they all have environments that are indistinguishable.

It is important to emphasize of *comparing radio sources in the same redshift bins* to obtain a complete overview of their large-scale environments, because this method takes into account cosmological biases (like spectroscopic redshift survey completeness).

The main results are summarized as follows:

1. Median values of the number of cosmological neighbors within 500 kpc e 2 Mpc (N_{cn}^{500} and N_{cn}^{2000}) are systematically higher than those of radio galaxies within a level of confidence of 0.4% and 2%, depending on N_{cn}^{500} and N_{cn}^{2000}, respectively;

2. the average projected distance d_{cn}^{m} of the cosmological neighbors as function of the standard deviation σ_z of the redshift distribution of the cosmological neighbors and of the redshift z_{src} of the sources is clustered around a distance of ~1 Mpc, implying that in the redshift range explored, WATs environments have similar sizes, and do not exceed 1.2 Mpc, while there is no trend observed for FR Is and FR IIs;

3. typical values of the concentration parameter ζ_{cn} for WATs are well above 0.25 (it is $\geqslant 0.25$ for 41 sources out of 47), value expected considering a uniform distribution of cosmological neighbors around the central RG, implying that WATs tend to inhabit the central region of the galaxy group/cluster in which they reside, therefore possibly being associated with the BCG of the galaxy group/cluster.

I have also explored any link between d_m^{cn} and σ_z in comparison with the absolute magnitude in the R band of the radio galaxy, but no trend/link is identified. A similar situation occurs also when comparing both these environmental parameters with radio power L_R and emission line luminosity of the [OIII], i.e., $L_{[OIII]}$.

I plan to extend this sample with observations from low radio frequency telescopes, such as LOFAR and the uGMRT, augmented with the analysis of WAT*CAT* X-ray observations. I could therefore estimate properties of the ICM, such as X-ray luminosity L_X, mass and environmental mass M_{env} as well as X-ray fluxes. This information will complement the results obtained from the environmental parameters, given that both d_{cn}^{m} and ζ_{cn} traces the position of the mass, not the gas.

Table 4.1 Parameters used for the analysis of the WATs sample

SDSS name	z_{src}	N_{cn}^{500}	N_{cn}^{2000}	ζ_{cn}	σ_z	d_{cn}^m
J004312.85-103956.0	0.12754	2.0	7.0	0.40	0.001	736.99
J080101.35+134952.2	0.10872	5.0	16.0	0.55	0.002	1013.38
J080337.67+105042.4	0.14234	1.0	4.0	0.33	0.001	927.21
J081803.86+543708.4	0.11742	7.0	28.0	0.5	0.002	975.40
J082718.31+463510.8	0.12487	2.0	9.0	0.33	0.001	959.80
J085116.24+082723.1	0.06354	7.0	15.0	0.87	0.002	1011.96
J091337.21+031720.5	0.14163	1.0	10.0	0.25	0.003	1195.88
J092428.89+141409.3	0.13842	5.0	33.0	0.42	0.002	1052.34
J092539.06+362705.6	0.11212	3.0	18.0	0.37	0.002	1015.23
J092612.34+324721.2	0.13953	3.0	4.0	1.0	0.001	628.37
J093349.82+451957.8	0.13387	1.0	4.0	0.5	0.001	854.25
J095716.41+190651.2	0.09039	2.0	11.0	0.29	0.002	913.53
J101932.33+140301.8	0.14558	4.0	10.0	0.80	0.002	989.99
J103502.62+425548.3	0.13602	2.0	3.0	0.67	0.002	288.96
J103605.76+000606.8	0.09683	0.0	3.0	0.0	9.32E-4	1053.76
J103636.24+383508.1	0.14489	0.0	3.0	0.0	0.001	1126.64
J103856.37+575247.5	0.10078	1.0	2.0	0.5	4.40E-4	396.52
J104645.86+314426.8	0.11386	2.0	16.0	0.28	0.001	1049.01
J104914.08+005945.2	0.10648	9.0	22.0	0.56	0.001	840.99
J114020.23+535029.1	0.14799	0.0	2.0	0.0	6.50E-5	983.40
J114111.81+054405.0	0.09743	13.0	57.0	0.59	0.002	1061.37
J115424.56+020653.0	0.13243	0.0	0.0	0.0	0.0	0.0
J115513.65-003133.9	0.13218	2.0	14.0	0.33	0.002	1117.27
J120118.19+061859.3	0.13505	1.0	3.0	0.5	3.66E-4	974.12
J120455.02+483256.9	0.06562	10.0	32.0	0.77	0.002	1035.64
J121439.53+052803.9	0.0778	5.0	26.0	0.5	0.002	1134.36
J130904.46+102935.3	0.08661	3.0	23.0	0.19	0.002	965.99
J133038.38+381609.7	0.10978	3.0	7.0	0.75	0.002	835.37
J135315.36+550648.2	0.14342	3.0	6.0	0.75	0.001	721.07
J141456.58+001223.0	0.12702	1.0	9.0	0.25	0.001	1189.28
J141513.98-013703.7	0.14959	0.0	1.0	0.0	0.0	981.44
J141718.94+060812.3	0.10972	3.0	17.0	0.30	0.002	987.50
J141731.27+081230.1	0.0568	25.0	77.0	0.48	0.002	844.98
J141927.23+233810.2	0.13732	1.0	2.0	0.5	7.45E-4	569.33
J143304.34+033037.6	0.14792	1.0	6.0	0.5	0.002	1158.48
J143409.03+013700.9	0.13786	2.0	9.0	0.40	0.001	882.68
J144700.45+460243.5	0.12777	1.0	2.0	1.0	1.10E-4	838.92
J144904.27+025802.7	0.12179	2.0	7.0	0.40	0.001	688.48
J150229.04+524402.0	0.13307	1.0	5.0	0.25	8.03E-4	734.93
J151108.77+180153.3	0.116	6.0	19.0	0.5	0.002	860.58
J154346.14+341521.6	0.11747	2.0	7.0	0.5	9.58E-4	816.44
J154729.59+145657.0	0.08501	2.0	2.0	1.0	2.50E-5	265.28
J155343.59+234825.4	0.11761	1.0	3.0	0.5	2.98E-4	1008.10
J161828.98+295859.6	0.13382	1.0	5.0	0.25	0.002	804.95
J164527.68+272005.8	0.10182	5.0	20.0	0.45	0.002	991.86
J212546.35+005551.8	0.13501	10.0	32.0	0.42	0.002	789.58
J222455.24-002302.3	0.14204	1.0	10.0	0.25	0.001	1056.20

Col. (1): SDSS name.
Col. (2): Source redshift.
Col. (3,4): Number of cosmological neighbors within 500 and 2000 kpc, respectively, estimated at the z_{src} of the central radio galaxy.
Col. (5): The concentration parameter ζ_{cn}.
Col. (6): The standard deviation of the redshift distribution for the cosmological neighbors within 2 Mpc.
Col. (7): Average projected distance of cosmological neighbors within 2 Mpc.

References

Ascasibar, Y. & Markevitch, M. 2006, ApJ, 650, 102

Baldi, R. D., Capetti, A., & Giovannini, G. 2015, A&A, 576, A38

Baldi, R. D., Capetti, A., & Massaro, F. 2018, A&A, 609, A1

Becker, R. H., White, R. L., & Helfand, D. J. 1995, ApJ, 450, 559

Bennett, C. L., Larson, D., Weiland, J. L., & Hinshaw, G. 2014, ApJ, 794, 135

Berlind, A. A., Frieman, J., Weinberg, D. H., Blanton, M. R., Warren, M. S., Abazajian, K., Scranton, R., Hogg, D. W., Scoccimarro, R., Bahcall, N. A., Brinkmann, J., Gott, J. Richard, I., Kleinman, S. J., Krzesinski, J., Lee, B. C., Miller, C. J., Nitta, A., Schneider, D. P., Tucker, D. L., Zehavi, I., & SDSS Collaboration. 2006, ApJS, 167, 1

Best, P. N. 2004, MNRAS, 351, 70

Best, P. N. & Heckman, T. M. 2012, MNRAS, 421, 1569

Bird, C. M. 1994, AJ, 107, 1637

Blanton, E. L., Gregg, M. D., Helfand, D. J., Becker, R. H., & Leighly, K. M. 2001, AJ, 121, 2915

Blanton, E. L., Paterno-Mahler, R., Wing, J. D., Ashby, M. L. N., Golden-Marx, E., Brodwin, M., Douglass, E. M., Randall, S. W., & Clarke, T. E. 2015, in Extragalactic

Jets from Every Angle, ed. F. Massaro, C. C. Cheung, E. Lopez, & A. Siemiginowska, Vol. 313, 315–320

Burns, J. O. 1981, MNRAS, 195, 523

Capetti, A., Massaro, F., & Baldi, R. D. 2017a, A&A, 598, A49

—. 2017b, A&A, 601, A81

Carilli, C. L. & Barthel, P. D. 1996, A&A Rev., 7, 1

Gómez, P. L., Pinkney, J., Burns, J. O., Wang, Q., Owen, F. N., & Voges, W. 1997, ApJ, 474, 580

Hill, G. J. & Lilly, S. J. 1991, ApJ, 367, 1

Huchra, J. P. & Geller, M. J. 1982, ApJ, 257, 423

Leahy, J. P. 1993, in Jets in Extragalactic Radio Sources, ed. H.-J. Röser & K. Meisenheimer, Vol. 421, 1

Massaro, F., Álvarez-Crespo, N., Capetti, A., Baldi, R. D., Pillitteri, I., Campana, R., & Paggi, A. 2019, ApJS, 240, 20

Missaglia, V., Massaro, F., Capetti, A., Paolillo, M., Kraft, R. P., Baldi, R. D., & Paggi, A. 2019, A&A, 626, A8

O'Donoghue, A. A., Owen, F. N., & Eilek, J. A. 1990, ApJS, 72, 75

Owen, F. N. & Rudnick, L. 1976, ApJ, 205, L1

Pinkney, J. 1995, PhD thesis, New Mexico State University

Prestage, R. M. & Peacock, J. A. 1988, MNRAS, 230, 131

Sakelliou, I. & Merrifield, M. R. 2000, MNRAS, 311, 649

Smolčić, V., Schinnerer, E., Finoguenov, A., Sakelliou, I., Carilli, C. L., Botzler, C. S., Brusa, M., Scoville, N., Ajiki, M., Capak, P., Guzzo, L., Hasinger, G., Impey, C., Jahnke, K., Kartaltepe, J. S., McCracken, H. J., Mobasher, B., Murayama, T., Sasaki, S. S., Shioya, Y., Taniguchi, Y., & Trump, J. R. 2007, ApJS, 172, 295

Tago, E., Saar, E., Tempel, E., Einasto, J., Einasto, M., Nurmi, P., & Heinämäki, P. 2010, A&A, 514, A102

Tempel, E., Tago, E., & Liivamägi, L. J. 2012, A&A, 540, A106

York, D. G., Adelman, J., Anderson, John E., J., Anderson, S. F., Annis, J., Bahcall, N. A., Bakken, J. A., Barkhouser, R., Bastian, S., Berman, E., Boroski, W. N., Bracker, S., Briegel, C., Briggs, J. W., Brinkmann, J., Brunner, R., Burles, S., Carey, L., Carr, M. A., Castander, F. J., Chen, B., Colestock, P. L., Connolly, A. J., Crocker, J. H., Csabai, I., Czarapata, P. C., Davis, J. E., Doi, M., Dombeck, T., Eisenstein, D., Ellman, N., Elms, B. R., Evans, M. L., Fan, X., Federwitz, G. R., Fiscelli, L., Friedman, S., Frieman, J. A., Fukugita, M., Gillespie, B., Gunn, J. E., Gurbani, V. K., de Haas, E., Haldeman, M., Harris, F. H., Hayes, J., Heckman, T. M., Hennessy, G. S., Hindsley, R. B., Holm, S., Holmgren, D. J., Huang, C.-h., Hull, C., Husby, D., Ichikawa, S.-I., Ichikawa, T., Ivezić, Ž., Kent, S., Kim, R. S. J., Kinney, E., Klaene, M., Kleinman, A. N., Kleinman, S., Knapp, G. R., Korienek, J., Kron, R. G., Kunszt, P. Z., Lamb, D. Q., Lee, B., Leger, R. F., Limmongkol, S., Lindenmeyer, C., Long, D. C., Loomis, C., Loveday, J., Lucinio, R., Lupton, R. H., MacKinnon, B., Mannery, E. J., Mantsch, P. M., Margon, B., McGehee, P., McKay, T. A., Meiksin, A., Merelli, A., Monet, D. G., Munn, J. A., Narayanan, V. K., Nash, T., Neilsen, E., Neswold, R., Newberg, H. J., Nichol, R. C., Nicinski, T., Nonino, M., Okada, N., Okamura, S., Ostriker, J. P., Owen, R., Pauls, A. G., Peoples, J., Peterson, R. L., Petravick, D., Pier, J. R., Pope, A., Pordes, R., Prosapio, A., Rechenmacher, R., Quinn, T. R., Richards, G. T., Richmond, M. W., Rivetta, C. H., Rockosi, C. M., Ruthmansdorfer, K., Sandford, D., Schlegel, D. J., Schneider, D. P., Sekiguchi, M., Sergey, G., Shimasaku, K., Siegmund, W. A.,

Smee, S., Smith, J. A., Snedden, S., Stone, R., Stoughton, C., Strauss, M. A., Stubbs, C., SubbaRao, M., Szalay, A. S., Szapudi, I., Szokoly, G. P., Thakar, A. R., Tremonti, C., Tucker, D. L., Uomoto, A., Vanden Berk, D., Vogeley, M. S., Waddell, P., Wang, S.-i., Watanabe, M., Weinberg, D. H., Yanny, B., Yasuda, N., & SDSS Collaboration. 2000, AJ, 120, 1579

Zirbel, E. L. 1997, ApJ, 476, 489

Chapter 5

Summary, Conclusions & Future Perspectives

5.1 Summary & Conclusions

My Ph.D. project has been devoted to the study of radio-loud AGN (i.e. radio galaxies and quasars), the environments in which they reside, and the interconnection between the radio and the X-ray emission, the former due to synchrotron emission in the radio lobes, the latter arising from both radio galaxies lobes/jets and the hot plasma that constitutes the intracluster medium (ICM). The key to understand how galaxies form and evolve with time is in understanding how feedback occurs in active galaxies hosted in galaxy groups/clusters. It has been indeed shown, combining radio observations with X-rays, that AGN feedback acts on the ICM cooling and can also ignite/quench the star formation.

In Chapter 3 I have presented the results obtained from radio and X-ray observations of the most powerful radio sources in the northern hemisphere: radio sources from the Third Cambridge Catalog. In particular, in Section 3.2, I have analysed sources that were previously classified as "unidentified" (because they lacked the detection of an optical counterpart) with available *Chandra* snapshot observations in the X-rays. To point at unidentified radio galaxies, X-ray observations based on old radio images with low angular resolution have been used. Given the low radio-loud AGN spatial density, I expect to find the X-ray counterpart of the radio core near the radio core observed in the radio image. For the seven sources considered here, I have reduced unpublished Very Large Array (VLA)

radio observations, to obtain a more accurate position of the radio core and compare it with that observed in the X-ray, a radio classification, and a measure of the total flux of the source. Counterpart were also searched in the optical and infrared (IR) bands, via Panoramic Survey Telescope & Rapid Response System (Pan-STARRS) and Wide-field Infrared Survey Explorer (WISE) data. The results of this analysis can be summarized as follows: six out of seven sources show a clear detection of the radio core, and all six have IR and X-ray counterparts of the radio core detected, while only three sources have the optical counterpart detected. For four sources I performed X-ray spectral analysis of the nuclear region, and I used IR magnitudes to estimate their tentative redshift. X-ray emission has been detected in correspondence with the radio jet of 3CR 158, while two sources showed diffuse X-ray emission. One of these two sources, 3CR 454.2, shows a clear Fanaroff-Riley type 2 (FR II) radio morphology: FR II radio sources in the 3C, however, tend to live in poorer systems with respect to galaxy clusters, but in this case I detected not only what is an hallmark of galaxy clusters but also two tentative X-ray cavities, sign of the radio lobe/ICM interaction, as predicted by the radio-mode feedback. All results are published in Missaglia et al. (2021). In Section 3.3 I reported new, high radio frequency, spectro-polarimetric observations of the giant radio galaxy (GRG) 3CR 403.1 obtained with the Sardinia Radio Telescope (SRT), used to estimate the surface brightness, the rotation measure (RM) and the ICM magnetic field. This source shows a radio spectrum with oldest electrons close to the core, and younger ones at the tip of the lobes. From the RM analysis, I estimated the magnetic field in the ICM and the age of the source. This new data have been complemented with the *Chandra* snapshot observation of this source, that revealed the presence of X-ray diffuse emission, suggesting therefore the presence of a group/cluster hosting 3CR 403.1, confirmed by optical MUSE data, used to estimate the redshifts of the group members, their velocity dispersion and therefore the mass of the environment. The most intriguing result of this analysis is the detection in the SRT image of two regions, in proximity of the large scale radio structure of 3CR 403.1, with negative intensity at 18.6 GHz. This negative signal can be either due to the Sunyaev-Zel'dovich effect (see Section 1.4.1), or to

cold, "ghost" electrons from a previous AGN activity. GRG are reported to grow in low density environment, but the presence of diffuse X-ray emission and possibly electrons from past AGN activity represent a starting point to better study environment and evolution of these sources. Results of this analysis are published in Missaglia et al. (2022). In Section 3.4, I presented new optical and X-ray observation of the high redshift (z=1.408) quasar 3C 297. *Chandra* X-ray observations indicate the presence of an X-ray luminous hot gas halo, suggesting the presence of a galaxy cluster hosting 3C 297, but optical observations show no galaxies at the same redshift of 3C 297, and also point to the presence of an extreme gas outflow. This source could be the first case of fossil group at high-redshift, and therefore a chance to study AGN cooling-flows at such high redshift, because fossil groups catalogs are usually limited to z <0.5.

It is still debated what is the general dependence of radio galaxy structures on the physical properties of the ICM and of the large-scale environment in general, as can be obtained, for example, from optical observations of the group/cluster richness. This theme has been studied, as shown in Chapter 4, for a peculiar class of radio sources: the wide angle tail radio galaxies (WATs, see Figure 5.1 left panel). I studied the environment of WATs from a complete sample in the local Universe ($z \lesssim$0.15) using parameters obtained from the so-called cosmological neighbors, that is optical sources lying within 2 Mpc from the central WAT and with a spectroscopic redshift z such that $\Delta z = |z_{\rm WAT} - z| \leq 0.005$ (see Figure 5.1, right panel). I found that WATs tend to inhabit large-scale environments with a larger galaxy richness than that of FR Is and FR IIs, and this is in agreement with WATs morphology (transition jet-warmspot-plume) being induced by clusters mergers. Also, the average project distance of the cosmological neighbors shows that WATs are clustered around a distance of ~ 1 Mpc, and therefore feature similar sizes in the redshift range explored. In addition, WATs tend to inhabit the central region of the galaxy group/cluster in which they reside, as shown from the values of the concentration parameter.

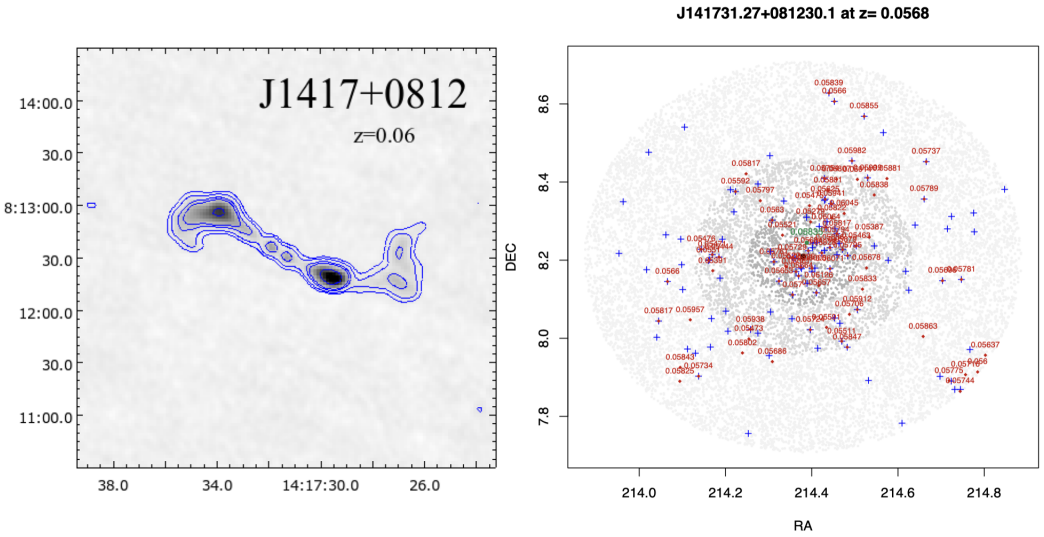

Figure 5.1 *Left Panel*: FIRST radio contours of the WAT source J1417+0812 from the WATCAT sample (Missaglia et al. 2019). *Right Panel*: SDSS J141731.27+081230.1 is the central black point, while different intensities of gray indicate SDSS sources lying within 500 kpc, 1 Mpc, and 2 Mpc from z_{src}=0.0568, respectively. Red circles indicate the cosmological neighbors, while blue crosses mark candidate elliptical galaxies, i.e., SDSS sources in the field with optical colors similar to quiescent elliptical galaxies at z_{src}=0.0568 and within $\Delta\, z$ of 0.005. In green the location of the closest group or cluster of galaxies, within $\Delta\, z$ of 0.005, listed in the Tempel et al. (2012) catalog of galaxy clusters/groups.

5.2 Future perspectives

Another interesting aspect of the interaction radio morphology/ICM is given by the possibility that merging induced shocks interact with the radio lobes of radio galaxies rejuvenating and accelerating old, cool electrons therein. This could be the case of the radio galaxy J2210+0846 in the merging cluster Abell 2395 (see Figure 5.2). Thanks to *Chandra* X-ray observations, it was possible to have the first hint of the dynamical state of the cluster: there is the clear detection of two interacting BCGs. In addition, two discontinuities from the surface brightness profile of the diffuse X-ray emission indicate the presence of shock induced luminosity/temperature variations.

Then, as a PI, I have obtained Giant Metrewave Radio Telescope (GMRT) observations (proposal number 38_051) in both band 3 (250-500 MHz) and 4 (550-900 MHz). These data

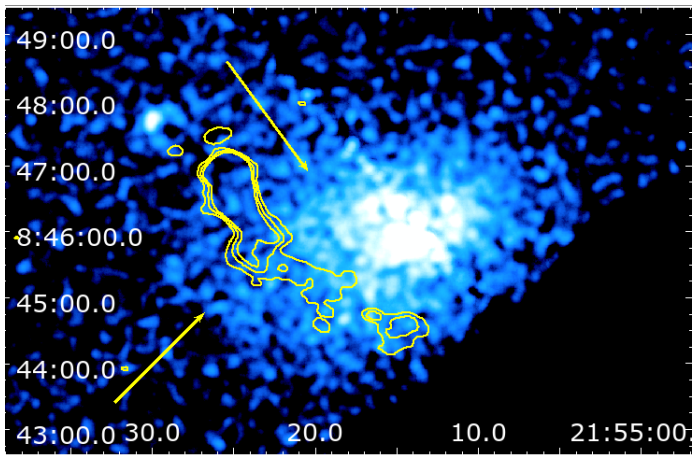

Figure 5.2 LOw Frequency ARray (LOFAR) radio contours of J2155+0846 at 145 MHz (yellow) overlaid on the *Chandra* exposure-corrected, background-subtracted image (0.5-3 keV) of the cluster Abell 2395. Yellow arrows point at the two discontinuities in the surface brightness. The tail of the radio source lies roughly between these two discontinuities. Preliminary image from Missaglia et al, in preparation.

are essential to trace the low frequency emission of the plumes of the radio galaxy, that shows a wide-angle tail morphology, probably due to the ram pressure originated from the merger. With these new data it will be possible to test if, as described by van Weeren et al. (2017), cluster shocks can efficiently re-accelerate electrons.

Low radio frequency observations from the LOFAR Two-metre Sky Survey have been used to study the properties of a sample of GRG up to redshift z=2.3 (Dabhade et al. 2020). Given the interesting results obtained for the source 3CR 403.1, a request for an SRT observational campaign of GRG is currently in preparation, to compare SRT high frequencies data with that obtained by LOFAR. finally, I plan to extend the WAT sample at higher redshifts and to obtain and analyze X-ray observations of sources in the WATCAT, to estimate the ICM properties and complement the information obtained from the environmental parameters.

References

Dabhade, P., Röttgering, H. J. A., Bagchi, J., Shimwell, T. W., Hardcastle, M. J., Sankhyayan, S., Morganti, R., Jamrozy, M., Shulevski, A., & Duncan, K. J. 2020, A&A, 635, A5

Missaglia, V., Massaro, F., Capetti, A., Paolillo, M., Kraft, R. P., Baldi, R. D., & Paggi, A. 2019, A&A, 626, A8

Missaglia, V., Massaro, F., Liuzzo, E., Paggi, A., Kraft, R. P., Forman, W. R., Jimenez-Gallardo, A., Madrid, J. P., Ricci, F., Stuardi, C., Wilkes, B. J., Baum, S. A., O'Dea, C. P., Kuraszkiewicz, J., Tremblay, G. R., Maselli, A., Capetti, A., Sani, E., Balmaverde, B., & Harris, D. E. 2021, ApJS, 255, 18

Missaglia, V., Murgia, M., Massaro, F., Paggi, A., Jimenez-Gallardo, A., Forman, W. R., Kraft, R. P., & Balmaverde, B. 2022, ApJ, 936, 10

Tempel, E., Tago, E., & Liivamägi, L. J. 2012, A&A, 540, A106

van Weeren, R. J., Andrade-Santos, F., Dawson, W. A., Golovich, N., Lal, D. V., Kang, H., Ryu, D., Brìggen, M., Ogrean, G. A., Forman, W. R., Jones, C., Placco, V. M., Santucci, R. M., Wittman, D., Jee, M. J., Kraft, R. P., Sobral, D., Stroe, A., & Fogarty, K. 2017, Nature Astronomy, 1, 0005

Appendix A

Radiative Processes

RL AGN are generally characterized by the ejection of a pair of plasma blobs in opposite directions, which eventually expand to form radio lobes that surround the radio jets. The jet propagates until the collimation is supported by the jet speed. It will eventually slow down due to sheer friction with the surrounding medium and disrupt into lobes or plumes.

Particles accelerated in relativistic jets emit mainly via non-thermal process: synchrotron radiation (in the radio and optical energy range) and inverse Compton scattering (in the X-rays). X-ray photons are also produced via thermal processes, i.e. bremsstrahlung. In the following I will report on the basic details of the synchrotron radiation, inverse Compton scattering and bremsstrahlung radiation.

A.1 Synchrotron Radiation

The radio emission from the extended radio sources is primarily optically thin synchrotron emission (see Fig. A.1).

The motion of a charged particle in a constant, uniform magnetic field B, comprises a constant velocity component along the field, and a circular motion in a plane perpendicular to the field. As a consequence of the centripetal acceleration of the charge due to Lorentz

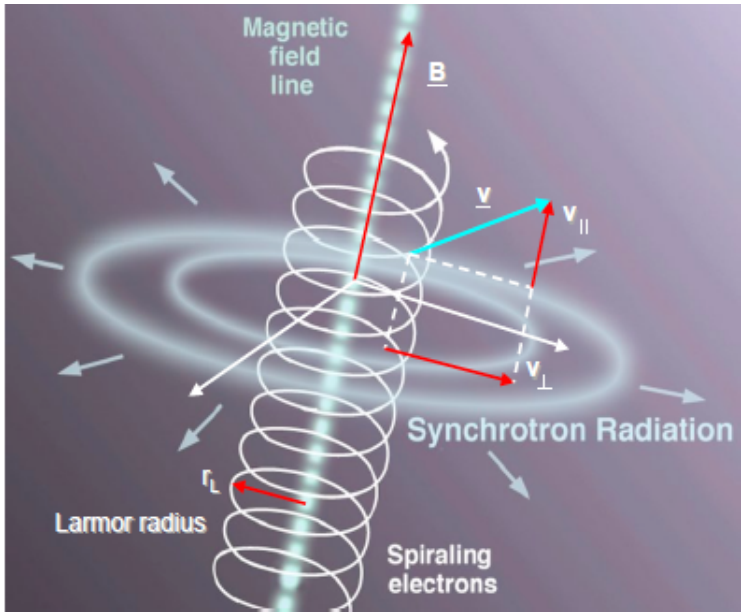

Figure A.1 Helical motion of an electron in a uniform magnetic field.

force, energy is radiated, and for relativistic particles this emission is called synchrotron radiation.

The power radiated by a single electron of Lorentz factor γ is:

$$P = \frac{2}{3}\frac{e^2}{4\pi\epsilon_0}c^{-3}\gamma^4(a_\perp^2 + \gamma^2 a_\parallel^2) \tag{A.1}$$

in terms of the components of acceleration perpendicular ($a_\perp$) and parallel ($a_\parallel$) to the instantaneous electron velocity (see e.g., Rybicki & Lightman 1979 for a complete review). For an electron gyrating in a magnetic field, $a_\parallel = 0$, whilst $a_\perp = v_\perp eB/\gamma m_e$, therefore:

$$P_s = \frac{8\pi}{3}\frac{1}{\mu_0}r_0^2 c \sin^2\psi\gamma^2 B^2 = 2\sigma_T c \sin^2\psi\gamma^2 u_B \tag{A.2}$$

where r_0 is the classical electron radius ($r_0 = \frac{e^2}{4\pi\epsilon_0 m_e c^2}$), σ_T is the Thomson cross section, ψ is the *pitch-angle* (defined by $\psi = \cos^{-1}\mu = \cos^{-1}(v_\parallel/v)$), and $u_B = \frac{B^2}{4\pi}$ the energy density of the magnetic field. The power may be averaged over pitch-angle, in which case the factor $\sin^2\psi$ becomes 2/3 if the pitch-angle distribution is isotropic.

Equation A.2 gives the energy radiated over all frequencies and solid angles, but an important consequence of the relativistic particle velocity is that this radiation is beamed into a cone of semi-angle $1/\gamma$ (in radians) about the instantaneous particle direction. If $1/\gamma \ll 1$, an observer sees radiation from an electron only as this cone sweeps across the line-of-sight; thus for the radiation to be "visible", the angle of the magnetic field to the line-of-sight must be approximately the particle pitch-angle. To receive radiation from particles in a magnetic field that is close to the line-of-sight, the particle pitch-angle must be small, and thus the radiated power will be small ($\sin^2\psi \sim 0$ in equation A.2).

Radio source magnetic fields are often turbulent, not unidirectional, and a "mean" angle to the line-of-sight may be used.

The characteristic frequency of emitted radiation is the inverse of the pulse width, which is determined by the gyrofrequency of the particle (taking the appropriate pitch-angle, and using the relativistic mass, γm_e) modified by one power of γ to account for the small opening angle of the 'cone' (see above), and two powers of γ (from a $1 - \frac{v}{c}$ term) to account for the difference between 'emission' and 'arrival' times of the pulse.

Thus most radiation is emitted at frequency:

$$\nu \approx \gamma^3 \frac{eB\sin\psi}{\gamma m_e} \approx \gamma^2 \Omega_e \sin\psi. \tag{A.3}$$

where $\Omega_e = \frac{eB}{m_e}$.

A detailed calculation of the field of a moving charge shows that the spectrum peaks at a frequency:

$$\nu_{max} = 0.29\nu_c \tag{A.4}$$

$$\nu_c = \frac{3}{2}\gamma^2 \Omega_e \sin\psi \tag{A.5}$$

where ν_c is the characteristic synchrotron frequency. It can be shown that the spectral power has low and high frequency behavior:

$$P_s \propto \begin{cases} (\nu/\nu_c)^{\frac{1}{3}} & \nu \ll \nu_c \\ (\nu/\nu_c)^{\frac{1}{2}} e^{-\omega/\omega_c} & \nu \gg \nu_c \end{cases} \tag{A.6}$$

where ω_c is the median frequency - half the power being radiated above, and half below this value. This spectrum is shown in the inset of Figure A.2. In some applications it proves adequate to assume that all the power is radiated at a frequency ν_c.

Assuming that the electron energy has a power-law distribution N(E), the emissivity is:

$$J(\nu)d\nu = -\frac{dE}{dt}N(E)dE \tag{A.7}$$

with

$$\frac{dE}{dt} = \frac{4}{3}\sigma_T\left(\frac{E}{c^2 m_e}\right)^2 c\frac{B^2}{2\mu_0} = \frac{4}{3}\sigma_T c U_B\left(\frac{v}{c}\right)^2\gamma^2 \tag{A.8}$$

With the appropriate substitutions, the emissivity can be expressed as:

$$J(\nu) = KB^{\frac{p+1}{2}}\nu^{\frac{-(p-1)}{2}} \tag{A.9}$$

with K being a constant factor.

Therefore, the synchrotron photon spectrum emitted by a power-law electron energy distribution is still approximately a power-law, and it can be also expressed in the form:

$$F_\nu \propto F_0\left(\frac{\nu}{\nu_0}\right)^{-\alpha} \tag{A.10}$$

where F_ν is the flux density expressed as:

$$F_\nu = \frac{dE}{dAdtd\nu} \tag{A.11}$$

It can be shown that the relation between the spectral index of the electron distribution (p) and that of the synchrotron emitted spectrum (α) is:

$$\alpha = \frac{p+1}{2} \tag{A.12}$$

while the normalization F_0 is proportional to the electron normalization n_0 and to B^2.

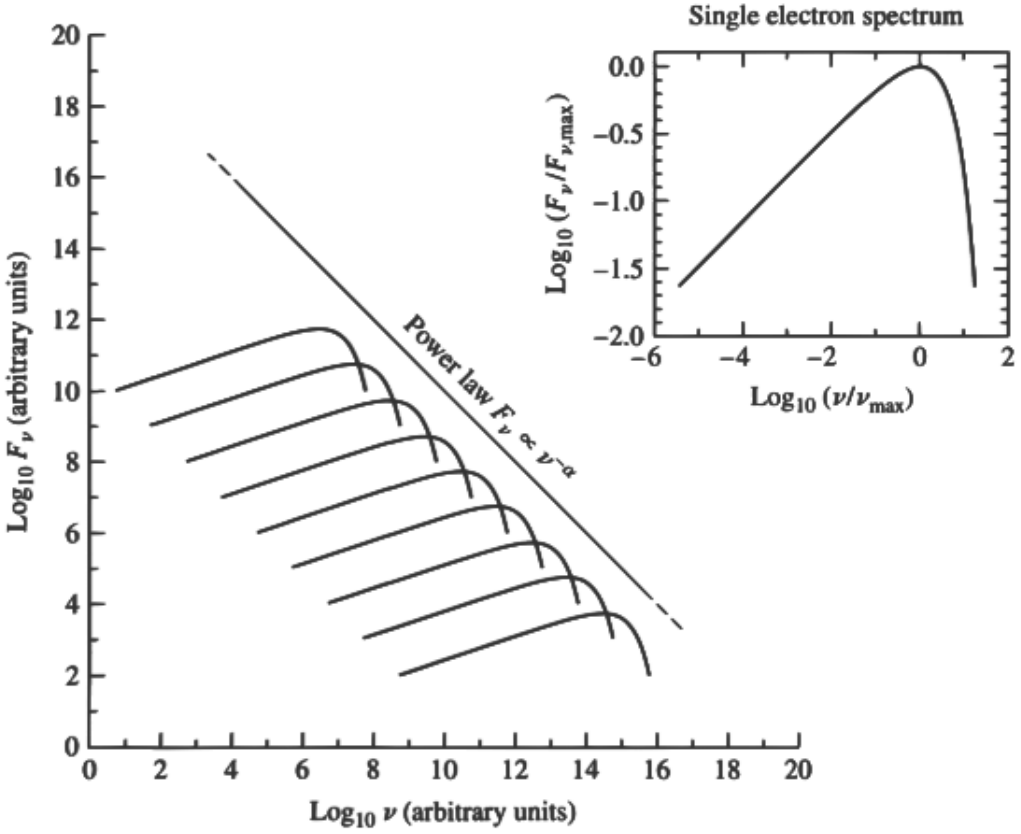

Figure A.2 Overlapping of single electron synchrotron spectra: the electrons have a power-law distribution (see inset), therefore the total spectrum is still a power-law.

A.2 Inverse Compton Scattering

In the Inverse Compton (IC) Scattering, electrons transfer energy to the photons (the inverse of the Compton Scattering). This collision increases the energy of the photons by a

factor γ^2, therefore high frequency radio photons interacting with relativistic electrons can be boosted to UV and X-ray bands. This is what typically happens in the lobes of radio galaxies: synchrotron radiation in the lobes implies the presence of magnetic fields(with a strength of the order of the μG) and relativistic electrons (with $\gamma \sim 10^3$-10^5). These electrons may interact with either Cosmic Microwave Background (CMB) photons, or with the very synchrotron photons emitted by the electrons themselves. The former case is the so-called IC/CMB, while the latter is the Synchrotron Self Compton (SSC). Assuming an uniform distribution of photons (isotropic radiation), the energy loss rate is:

$$\frac{dE}{dt} = \frac{4}{3}\sigma_T U_{rad} c \gamma^2 \beta^2 \tag{A.13}$$

where U_{rad} is is the energy density of the radiation field, σ_T is the Thomson cross-section, and $\beta = \frac{v}{c}$.

This result can be easily compared to the synchrotron loss of Equation A.8, obtaining:

$$\frac{P_{sync}}{P_{IC}} = \frac{U_B}{U_{rad}} \tag{A.14}$$

implying that the losses due to synchrotron and Compton emission are in the ratio of the magnetic field density to the photon field density and independent of γ.

A.3 Bremsstrahlung (or Free-Free Radiation)

When a free charged particle, as an electron, is accelerated by the presence of an electrostatic field due an ionized nucleus, it emits the so-called bremsstrahlung radiation (see Figure A.3). This condition happens, for example, in the ICM, the hot plasma that permeates the potential well of a galaxy group/cluster, with a density $n \sim 10^{-2} - 10^{-4} cm^{-3}$ and a temperature of T~ 10^8 K. Since the plasma is in equilibrium, the process is termed "thermal

bremsstrahlung". The total energy loss rate of the plasma is given by the formula:

$$-\frac{dE}{dt} \propto Z^2 T^{\frac{1}{2}} N N_e \overline{g} \tag{A.15}$$

with N_e and N being the number density of the electrons and of the nuclei, respectively, and $\overline{g}$ is a frequency (ν) averaged Gaunt factor, that for X-rays is:

$$g(\nu, T) = \frac{\sqrt{3}}{\pi} \ln\left(\frac{kT}{h\nu}\right) \tag{A.16}$$

Through the bremsstrahlung emissivity of the gas and its temperature, it is possible to obtain an estimate of the mass M of the ICM within a certain radius r. If a gas of pressure p and density ρ is in hydrostatic equilibrium (as in the case of the ICM), it holds:

$$\frac{dp}{d\rho} = -\frac{GM(\leq r)\rho}{r} \tag{A.17}$$

and for the perfect gas law:

$$p = \frac{\rho kT}{\mu m_H} \tag{A.18}$$

Density and temperature of the ICM can be obtained from X-ray spectral fit with the APEC model [1]. The normalization of the model is related to the density by:

$$norm = \frac{10^{-14}}{4\pi[D_A(1+z)]^2} \int n_e n_H dV \tag{A.19}$$

where D_A is the angular size distance, z is the redshift of the source, n_e and n_H are the electron and H densities, respectively.

Therefore:

$$\frac{\rho kT}{\mu m_H}\left(\frac{1}{\rho}\frac{d\rho}{dr} + \frac{1}{T}\frac{dT}{dr}\right) = -\frac{GM(\leq r)\rho}{r} \tag{A.20}$$

$$M(\leq r) = -\frac{kTr^2}{G\mu m_H}\left[\frac{d(\log\rho)}{dr} + \frac{d(\log T)}{dr}\right] \tag{A.21}$$

[1] https://heasarc.gsfc.nasa.gov/xanadu/xspec/manual/XSmodelApec.html

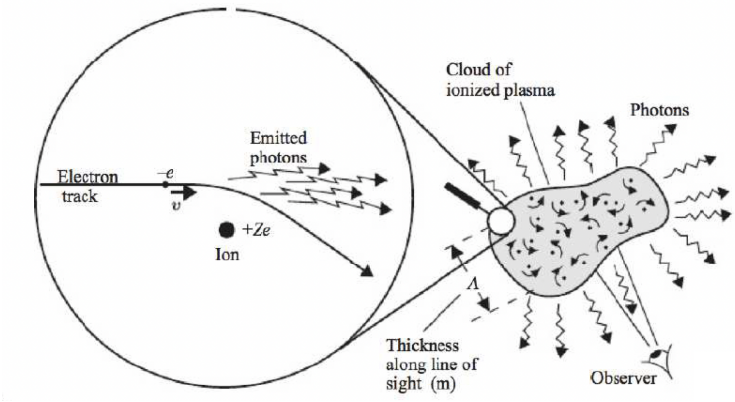

Figure A.3 Cartoon illustrating the bremsstrahlung emission of a cloud of ionized plasma due to the interaction of a free electron with the ions in the cloud.

X-ray spectra of the ICM show also discrete line emission, due to atomic process such as collisional excitation and radiative recombination in a turbulent plasma. The best example is given by the spectrum of the Perseus cluster core obtained by the Hitomi Observatory (Takahashi et al. 2014). The full array spectrum is shown in Figure A.4.

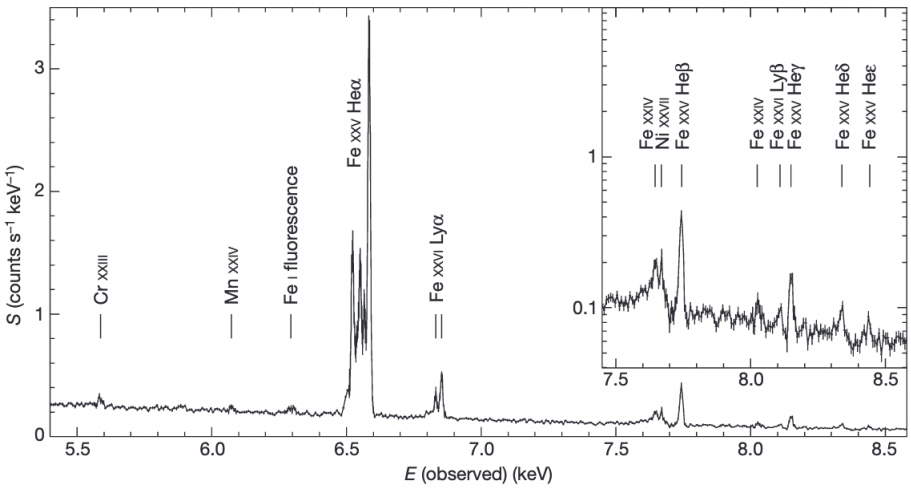

Figure A.4 Full array spectrum of the core of the Perseus cluster obtained by the Hitomi observatory. The redshift of the Perseus cluster is z=0.01756. The inset has a logarithmic scale, which allows the weaker lines to be better seen. The flux S is plotted against photon energy E.

References

Rybicki, G. B. & Lightman, A. P. 1979, Radiative processes in astrophysics

Takahashi, T., Mitsuda, K., Kelley, R., Aharonian, F., Akamatsu, H., Akimoto, F., Allen, S., Anabuki, N., Angelini, L., Arnaud, K., Asai, M., Audard, M., Awaki, H., Azzarello, P., Baluta, C., Bamba, A., Bando, N., Bautz, M., Bialas, T., Blandford, R. D., Boyce, K., Brenneman, L., Brown, G., Cackett, E., Canavan, E., Chernyakova, M., Chiao, M., Coppi, P., Costantini, E., de Plaa, J., den Herder, J.-W., DiPirro, M., Done, C., Dotani, T., Doty, J., Ebisawa, K., Enoto, T., Ezoe, Y., Fabian, A., Ferrigno, C., Foster, A., Fujimoto, R., Fukazawa, Y., Funk, S., Furuzawa, A., Galeazzi, M., Gallo, L., Gandhi, P., Gilmore, K., Guainazzi, M., Haas, D., Haba, Y., Hamaguchi, K., Harayama, A., Hatsukade, I., Hayashi, K., Hayashi, T., Hayashida, K., Hiraga, J., Hirose, K., Hornschemeier, A., Hoshino, A., Hughes, J., Hwang, U., Iizuka, R., Inoue, Y., Ishibashi, K., Ishida, M., Ishikawa, K., Ishimura, K., Ishisaki, Y., Itoh, M., Iwata, N., Iyomoto, N., Jewell, C., Kaastra, J., Kallman, T., Kamae, T., Kataoka, J., Katsuda, S., Katsuta, J., Kawaharada, M., Kawai, N., Kawano, T., Kawasaki, S., Khangaluyan, D., Kilbourne, C., Kimball, M., Kimura, M., Kitamoto, S., Kitayama, T., Kohmura, T., Kokubun, M., Konami, S., Kosaka, T., Koujelev, A., Koyama, K., Krimm, H., Kubota, A., Kunieda, H., LaMassa, S., Laurent, P., Lebrun, F., Leutenegger, M., Limousin, O., Loewenstein, M., Long, K., Lumb, D., Madejski, G., Maeda, Y., Makishima, K., Markevitch, M., Masters, C., Matsumoto, H., Matsushita, K., McCammon, D., McGuinness, D., McNamara, B., Miko, J., Miller, J., Miller, E., Mineshige, S., Minesugi, K., Mitsuishi, I., Miyazawa, T., Mizuno,

T., Mori, K., Mori, H., Moroso, F., Muench, T., Mukai, K., Murakami, H., Murakami, T., Mushotzky, R., Nagano, H., Nagino, R., Nakagawa, T., Nakajima, H., Nakamori, T., Nakashima, S., Nakazawa, K., Namba, Y., Natsukari, C., Nishioka, Y., Nobukawa, M., Noda, H., Nomachi, M., O'Dell, S., Odaka, H., Ogawa, H., Ogawa, M., Ogi, K., Ohashi, T., Ohno, M., Ohta, M., Okajima, T., Okazaki, T., Ota, N., Ozaki, M., Paerels, F., Paltani, S., Parmar, A., Petre, R., Pinto, C., Pohl, M., Pontius, J., Porter, F. S., Pottschmidt, K., Ramsey, B., Reis, R., Reynolds, C., Ricci, C., Russell, H., Safi-Harb, S., Saito, S., Sakai, S.-i., Sameshima, H., Sato, K., Sato, R., Sato, G., Sawada, M., Serlemitsos, P., Seta, H., Shibano, Y., Shida, M., Shimada, T., Shirron, P., Simionescu, A., Simmons, C., Smith, R., Sneiderman, G., Soong, Y., Stawarz, L., Sugawara, Y., Sugita, S., Szymkowiak, A., Tajima, H., Takahashi, H., Takahashi, H., Takeda, S.-i., Takei, Y., Tamagawa, T., Tamura, K., Tamura, T., Tanaka, T., Tanaka, Y., Tanaka, Y., Tashiro, M., Tawara, Y., Terada, Y., Terashima, Y., Tombesi, F., Tomida, H., Tsuboi, Y., Tsujimoto, M., Tsunemi, H., Tsuru, T., Uchida, H., Uchiyama, H., Uchiyama, Y., Ueda, Y., Ueda, S., Ueno, S., Uno, S., Urry, M., Ursino, E., de Vries, C., Wada, A., Watanabe, S., Watanabe, T., Werner, N., White, N., Wilkins, D., Yamada, S., Yamada, T., Yamaguchi, H., Yamaoka, K., Yamasaki, N., Yamauchi, M., Yamauchi, S., Yaqoob, T., Yatsu, Y., Yonetoku, D., Yoshida, A., Yuasa, T., Zhuravleva, I., Zoghbi, A., & ZuHone, J. 2014, in Society of Photo-Optical Instrumentation Engineers (SPIE) Conference Series, Vol. 9144, Space Telescopes and Instrumentation 2014: Ultraviolet to Gamma Ray, ed. T. Takahashi, J.-W. A. den Herder, & M. Bautz, 914425

Acknowledgements

The SARS-CoV-2 pandemic struck at the very beginning of my Ph.D. journey, but thanks to the love and support of my family and friends I achieved this goal, that I deeply cared about.

I want to thank my supervisor, Prof. Francesco Massaro, for always proving ideas on new projects and for introducing me to collaborators that helped me to grow scientifically.

I can't forget to thank Dr. E. T. Liuzzo and Dr. M. Brienza, for teaching me everything I know about radio astronomy, and for their thoughtfulness and patience.

A big help came for Dr. R. Kraft and Dr. A. Paggi, that introduced me to X-ray data analysis.

Raffaella, Maria Grazia, Anna and Paola, thank you for always being willing to reassure me. You made me feel loved.

Mom and dad, thank you for always putting up with my tantrums!!!

A., O. and E., thank you for your warm love.